Title
Investigating Source Processes of Isotropic Events

Author
Chiang, Andrea

Publication Date
2015

Peer reviewed|Thesis/dissertation

Investigating Source Processes of Isotropic Events

by

Andrea Chiang

A dissertation submitted in partial satisfaction of the

requirements for the degree of

Doctor of Philosophy

in

Earth and Planetary Science

in the

Graduate Division

of the

University of California, Berkeley

Committee in charge:

Professor Douglas S. Dreger, Chair
Professor Roland Bürgmann
Professor Nicholas Sitar

Fall 2015

Investigating Source Processes of Isotropic Events

Abstract

Investigating Source Processes of Isotropic Events

by

Andrea Chiang

Doctor of Philosophy in Earth and Planetary Science

University of California, Berkeley

Professor Douglas S. Dreger, Chair

This dissertation demonstrates the utility of the complete waveform regional moment tensor inversion (Dreger and Woods, 2002; Dreger, 2003; Minson and Dreger, 2008) for nuclear event discrimination. I explore the source processes and associated uncertainties for explosions and earthquakes under the effects of limited station coverage, compound seismic sources, assumptions in velocity models and the corresponding Green's functions, and the effects of shallow source depth and free-surface conditions. The motivation to develop better techniques to obtain reliable source mechanism and assess uncertainties is not limited to nuclear monitoring, but they also provide quantitative information about the characteristics of seismic hazards (e.g. Petersen et al., 2014), local and regional tectonics and in-situ stress fields of the region (Hardebeck and Hauksson, 2001; Hardebeck and Michael, 2006).

This dissertation begins with the analysis of three sparsely recorded events: the 14 September 1988 US-Soviet Joint Verification Experiment (JVE) nuclear test at the Semipalatinsk test site in Eastern Kazakhstan, and two nuclear explosions at the Chinese Lop Nor test site. We utilize a regional distance seismic waveform method fitting long-period, complete, three-component waveforms jointly with first-motion observations from regional stations and teleseismic arrays. The combination of long period waveforms and first motion observations provides unique discrimination of these sparsely recorded events in the context of the Hudson et al. (1989) source-type diagram. We demonstrate through a series of Jackknife tests and sensitivity analyses that the source-type of the explosions is well constrained. One event, a 1996 Lop Nor shaft explosion, displays large Love waves and possibly reversed Rayleigh waves at one station, indicative of a large tectonic release. We demonstrate the behavior of Network Sensitivity Solutions [NSS] (Ford et al., 2010) for models of tectonic release (Toksöz et al., 1965) and spall-based tensile damage (Patton and Taylor, 2008) over a range of F-factors and K-factors.

A potential issue for moment tensor inversion of explosions is that Green's functions have vanishing amplitudes at the free surface. Because explosions are detonated at very shallow

depths, this can result in bias in the moment tensor solution (Stevens and Murphy, 2001). It is important to understand these free surface effects on discriminating shallow explosive sources for nuclear monitoring purposes. It may also be important in natural systems that have shallow seismicity such as volcanoes and geothermal systems. To tackle this problem, we examine the effects of the free surface on the moment tensor via synthetic testing, and apply the moment tensor based discrimination method to well-recorded chemical explosions. These shallow chemical explosions represent rather severe source-station geometry in terms of the vanishing traction issues. We show that the combined waveform and first motion method enables the unique discrimination of these events, even though the data include unmodeled single force components resulting from the collapse and blowout of the quarry face immediately following the initial explosion. In contrast, recovering the announced explosive yield using seismic moment estimates from moment tensor inversion remains challenging but we can begin to put error bounds on our moment estimates using the NSS technique.

The estimation of seismic source parameters is dependent upon having a well-calibrated velocity model to compute the Green's functions for the inverse problem. Ideally, seismic velocity models are calibrated through broadband waveform modeling (e.g. Dreger and Helmberger, 1990; Bhattacharyya et al., 1999), however in regions of low seismicity velocity models derived from body or surface wave tomography may be employed (e.g. Tape et al., 2010; Shen et al., 2013; Porritt et al., 2014). Whether a velocity model is 1D or 3D, or based on broadband seismic waveform modeling or the various tomographic techniques, the uncertainty in the velocity model can be the greatest source of error in moment tensor inversion. These errors have not been fully investigated for the nuclear discrimination problem. To study the effects of unmodeled structures on the moment tensor inversion, we set up a synthetic experiment where we produce synthetic seismograms for a 3D model (Moschetti et al., 2010) and invert these data using Green's functions computed with a 1D velocity mode (Song et al., 1996) to evaluate the recoverability of input solutions, paying particular attention to biases in the isotropic component. We then evaluate source inversions for real data using Green's functions for 1D and 3D velocity models in which the Green's functions were computed by utilizing the principle of source-receiver reciprocity (Aki and Richards, 2002; Dahlen and Tromp, 1998), and the finite-difference method (Appelo and Petersson, 2009; Eisner and Clayton, 2001; Graves and Wald, 2001). Using the full waveform moment tensor inversion method we analyze earthquakes and explosions at NTS using 1D and 3D Earth models and compare the solutions and associated uncertainties at different frequency bands.

The synthetic experiment results indicate that the 1D model assumption is valid for moment tensor inversions at periods as short as 10 seconds for the 1D western U.S. model (Song et al., 1996). The correct earthquake mechanisms and source depth are recovered with statistically insignificant isotropic components as determined by the F-test. Shallow explosions are biased by the theoretical ISO-CLVD tradeoff but the tectonic release component remains low, and the tradeoff can be eliminated with constraints from P wave first motion.

Path-calibration to the 1D model can reduce non-double-couple components in earthquakes, non-isotropic components in explosions and composite sources and improve the fit to the data. When we apply the 3D model to real data, at long periods (20-50 seconds), we see good agreement in the solutions between the 1D and 3D models and slight improvement in waveform fits when using the 3D velocity model Green's functions. At high frequencies the advantage of the 3D model is limited except for paths from NTS to the San Francisco Bay, where we see a marked improvement in waveform fit. However, we do not see a clear reduction in source uncertainties when using a 3D model. A larger sample size is required to make useful interpretations about the use of 3D models in estimating source uncertainties. Our results indicate that the 3D model for the western U.S. (Moschetti et al., 2010) still needs further refinement to adequately model wave propagation at high frequencies and that path-averaged 1D models derived from the 3D model may be a more attractive approach than the more costly 3D simulation for short period inversions.

To my family.

Contents

Contents **ii**

List of Figures **iv**

List of Tables **vi**

1 Introduction **1**

2 Source characterization of underground explosions in Eastern Kazakhstan and Northwestern China **6**
2.1 Abstract . . . 6
2.2 Introduction . . . 7
2.3 Data Processing and Methods . . . 7
2.4 Results: Source Characterization . . . 11
2.4.1 14 September 1988 Soviet Joint Verification Experiment (JVE) . . . 11
2.4.2 15 May 1995 Lop Nor Shaft Explosion . . . 15
2.4.3 8 June 1996 Lop Nor Shaft Explosion . . . 17
2.5 Discussion . . . 23
2.5.1 Sensitivity to Station Geometry and Source Depth . . . 23
2.5.2 Effects of Tectonic Release and Damage Source Medium . . . 23
2.6 Conclusions . . . 26

3 Moment Tensor Analysis of Shallow Sources **30**
3.1 Abstract . . . 30
3.2 Introduction . . . 30
3.3 Methods . . . 32
3.4 Free-Surface Vanishing Traction . . . 34
3.5 HUMMING ALBATROSS . . . 37
3.6 Yield Estimates . . . 46
3.7 Discussion . . . 48
3.8 Conclusion . . . 50

4 Sensitivity of Seismic Moment Tensors to 3D Velocity Structure: A Synthetic Study **52**
4.1 Abstract . . . 52
4.2 Introduction . . . 52
4.3 Velocity Model and Computation Set Up . . . 55
4.4 Sensitivity to 3D Velocity Structure . . . 58
4.4.1 Double-Couple Sources . . . 58
4.4.2 Isotropic Sources . . . 60
4.4.3 Composite Sources . . . 61
4.4.4 Path Calibrations . . . 64
4.4.5 Random Velocity Perturbations . . . 66
4.5 Conclusion . . . 68

5 Comparing 1D and 3D Source Inversions: Application to the Western United States **73**
5.1 Abstract . . . 73
5.2 Introduction . . . 74
5.3 Method . . . 76
5.3.1 Inversion Procedure . . . 76
5.3.2 Reciprocal Green's Functions . . . 77
5.4 Moment Tensor Inversion Results . . . 79
5.4.1 Low Signal-to-Noise Events . . . 80
5.4.2 2002 Little Skull Mountain Earthquake . . . 81
5.4.3 Larger NTS Explosions . . . 82
5.4.4 Comparison in Source-Type Space . . . 88
5.5 Discussion . . . 91
5.6 Conclusion . . . 95

6 Conclusion **99**

Bibliography **103**

List of Figures

2.1 Map . . . 9
2.2 1988 Soviet JVE Source Model and Waveform Comparisons . . . 14
2.3 1988 Soviet JVE Network sensitivity solution (NSS) . . . 16
2.4 P-wave first motions . . . 18
2.5 1995 Lop Nor . . . 19
2.6 1996 Lop Nor . . . 21
2.7 1999 Lop Nor earthquake . . . 22
2.8 Source depth sensitivity . . . 24
2.9 ISO+DC composite source case . . . 28
2.10 ISO+CLVD composite source case . . . 29

3.1 Green's Functions . . . 35
3.2 Velocity Models . . . 37
3.3 Isotropic Moment and Total Seismic Moment . . . 38
3.4 Fixed Source Depth Sensitivity Analysis . . . 39
3.5 Map . . . 40
3.6 HUMMING ALBATROSS Moment Tensor Solutions . . . 42
3.7 Production Shot . . . 43
3.8 Network Sensitivity Solutions (NSS) . . . 44
3.9 Production Shot Depth Sensivity . . . 45
3.10 Multiple Frequency Bands . . . 46
3.11 M_{ISO} vs. Yield . . . 49

4.1 Velocity Model and Computation Set Up . . . 56
4.2 Comparisons with FK . . . 57
4.3 Double-Couple Moment Tensor Solutions and Waveforms . . . 59
4.4 Double-Couple Network Sensitivity Solutions . . . 60
4.5 Explosion Synthetic Waveforms . . . 62
4.6 Explosion Moment Tensor and Network Sensitivity Solution . . . 63
4.7 Composite Sources . . . 65
4.8 Path-Specific Calibrations . . . 66
4.9 Random Field . . . 68

4.10 Perturbed Velocity Model 69
4.11 1D and 3D Synthetic Waveforms 70
4.12 Normal Earthquake Moment Tensor and Network Sensitivity Solution 71
4.13 Explosion Moment Tensor and Network Sensitivity Solution 72

5.1 Map of Study Area 77
5.2 Forward and Reciprocal Waveform Comparison 80
5.3 COSO and Amargosa Full Moment Tensor Solution 82
5.4 Amargosa Network Sensitivity Solutions 83
5.5 2002 Little Skull Earthquake Full Moment Tensor Solution 84
5.6 2002 Little Skull Mountain Three-Station Inversion 85
5.7 2002 Little Skull Mountain Network Sensitivity Solutions 86
5.8 METROPOLIS Full Moment Tensor Solution 87
5.9 HOYA Full Moment Tensor Solution 89
5.10 JUNCTION Full Moment Tensor Solution 90
5.11 Comparing Uncertainites 92
5.12 Comparing Source-Type Parameters 93
5.13 Velocity Model 94
5.14 2002 Little Skull Mountain Full Moment Tensor Solution with Averaged 1D Models 97
5.15 HOYA Full Moment Tensor Solution with Averaged 1D Models 98

List of Tables

2.1 Event Information 8
2.2 Station Information 12
2.3 Velocity Models 13

3.1 Moment Tensor Solution and Yield 41

5.1 Table 1. Event Information 75

Acknowledgments

Being a part of the Berkeley Seismological Laboratory and the Department of Earth and Planetary Science at UC Berkeley has been a truly wonderful experience. I cannot imagine a better place to spend the last 5+ years.

First and foremost I want to thank my advisor Doug Dreger who is not only knowledgeable about all things seismology but is always encouraging, patient, supportive and genuinely a great person to be around with. His enthusiasm about science has always inspired me, and he is always able to encourage me when the results are not promising. His ability in having a good work-life balance has encouraged me to not only enjoy research but also never be afraid to pursue other hobbies. I would like to thank my second project advisor Roland Bürgmann who is incredibly patient and approachable. He always keeps his door open to students and colleagues who need help on tackling any bumps they encountered in their research, and make sure we do not go hungry at group meetings with lots of cookies and treats.

I particularly want to thank my fantastic D-squared cohorts: Aurelie Guilhem, Sierra Boyd, Voon Hui Lai, Avinash Nayak, Shan Dou, Seung-Hoon Yoo, Mong-Han Huang, Katie Wooddell, Ahyi Kim. I enjoy all the times we spent hanging out at the computer lab and all of the adventures we took outside the lab. I can always count on my fellow group mates for any obstacles along the way and having someone to chat with about all the good and bad things in life. My fellow classmates: Carolina, Jesse, Shou, Ana, and Jennifer, especially Carolina, Jesse and Shou whom in our second year of graduate school turned our weekly qualifying exam study group into a group therapy session. All my friends at the Seismo lab and EPS department: Eloisa, Jane, Sanne, Pam, Rob, Chris, William, Qingkai, Cheng, Laura, Scott, Allen.

I would also like to thank my mentors and collaborators from LLNL and AFRL, Sean Ford, Bill Walter, Arben Pitarka, and Eli Baker; my outside committee Nicholas Sitar and Chair of my qualifying exam committee Paul Renne; the graduate advisors Michael Manga, Bruce Buffett, Inez Fung. During these 5+ years at Berkeley I have met and get to know so many great people: the faculty, postdocs, researchers and staff at the Seismo lab, Richard, Barbara, Estelle, Manoo, Kim, Peggy, Clay, Jennifer, Taka'aki, Ingrid, Bob, Charley, Stephen, and Dawn; and the EPS staff Margie, Cryshtel, and Judith.

Lastly, words cannot express my gratitude towards my family: Mom, Dad, my brother Chris and my wonderful cat Flanagan who are always there for me through the multiple ups and downs of my Ph.D. career. My friends Jenny, Li-Yin, Jennifer, and Christie who kept my mental health in check, and always find the time in their busy schedules to be there for me. A big shout out to my friends and family in Taiwan, whom although I do not get to see very often, never seem to run out of things to say.

Chapter 1

Introduction

The use of regional distance long-period, complete waveform data to determine the seismic moment tensor is now a routine and reliable approach in determining the source mechanism of natural and manmade seismicity, and may be used to identify or discriminate different types of seismic sources. Such source-type identification is important for better understanding the physics of earthquakes (e.g. Romanowicz et al., 1993; Kao et al., 1998), geothermal and volcanic seismicity (Guilhem et al., 2014; Boyd et al., 2015; Templeton and Dreger, 2006; Minson et al., 2007; Tkalčić et al., 2009; Shuler et al., 2013b; Shuler et al., 2013a), seismicity in ice (Walter et al., 2009; Walter et al., 2010), as well as seismicity induced by anthropogenic activities such as mining (Dreger et al., 2008; Ford et al., 2008), oil and gas operations (McNamara et al., 2015), and explosions (e.g. Ekström and Richards, 1994; Dreger and Woods, 2002). The successful applications of the regional moment tensor method at the Nevada Test Site (NTS) and the 2006 and 2009 North Korea nuclear tests (Ford et al., 2009a; Ford et al., 2009b; Ford et al., 2010) show that the method is robust and capable for source-type discrimination of nuclear explosions at regional distances. Studies of underground cavity collapse and volcanic seismicity also show significant departures from assumed double-couple models of earthquakes (Minson et al., 2007; Ford et al., 2008).

The benefits of developing better techniques to study and understand seismic source processes are not limited to explosion monitoring. The recent and dramatic rise in unexpected seismicity in the central and eastern United States has generated much interest from the public and the scientific community because of the potential link to hydrocarbon production, and the possibility of industrial activities triggering damaging earthquakes in areas that are considered relatively stable and of low seismic risk. Monitoring microseismicity related to wastewater injections, mining activities and other industrial operations is sorely needed to improve our understanding of the relationship between seismicity and anthropogenic activities (Baig and Urbancic, 2010) and the imposed risks of induced seismicity (e.g. Ellsworth, 2013; McGarr, 2014; Keranen et al., 2014).

The goals of this dissertation are to study the uncertainty in regional distance seismic

moment tensor estimation due to the effects of limited station coverage, assumptions in velocity models for Green's function estimation, the effects of shallow source depth and free-surface conditions, compound seismic sources, as well as to expand the seismic moment tensor database to include more non-double-couple events.

To explore these issues and address these goals this dissertation is divided into three main sections: (1) The determination of source properties and associated uncertainties for explosions with large tectonic release and in sparse-monitoring situations in Eastern Kazakhstan and Lop Nor using long period seismic waveforms and regional and teleseismic P-wave first motion polarities; (2) The study of the effects of free-surface vanishing traction (FSVT) on shallow source inversions and magnitude-yield relations of low-magnitude, industrial chemical explosions; (3) The analysis of the effects of 3D wave propagation on source inversions and development of procedures for routine 3D moment tensor inversions of earthquakes and explosions.

In Chapter 2 the combined use of regional broadband waveforms and regional and teleseismic P-waves was applied to investigate the 14 September 1988 US-Soviet Joint Verification Experiment (JVE) nuclear test at the Semipalatinsk test site in Eastern Kazakhstan, and two nuclear explosions conducted less than ten years later at the Chinese Lop Nor test site. These events were very sparsely recorded by stations located within 1600 km, and for each event only 3 or 4 stations were available in the regional distance range for source analysis. Bowers (1997) and Bowers and Walter (2002) have qualitatively used teleseismic P waves to constrain moment tensors derived from regional broadband waveforms of mining events in South Africa, Germany and Wyoming. Ford et al. (2012) applied a more quantitative approach in which the combined use of regional and teleseismic data was implemented to constrain the source-type for the 2009 Democratic Peoples Republic of Korea nuclear test. Following the results of Ford et al. (2012) we incorporated first motion data from teleseismic stations, as well as regional stations to constrain the moment tensor derived source-type (Hudson et al., 1989; Julian et al., 1998) for the Soviet JVE and Lop Nor nuclear tests. The results show that unique discrimination of these events with large non-isotropic radiation is possible under extremely sparse monitoring conditions when long-period regional waveforms and P-wave first motion polarities are combined.

For the nuclear explosion discrimination problem the uncertainty in a given solution is as important as the best fitting parameters and therefore necessary to fully understand and model possible biases that can result in the recovered source mechanisms. A potential issue for shallow seismic sources that are effectively at the free surface is that as the traction vanishes the associated vertical dip-slip (DS) Green's functions have vanishing amplitudes (Julian et al., 1998), which in turn can result in the indeterminacy of the M_{xz} and M_{yz} components of the moment tensor and therefore bias in the moment tensor solution. The free-surface effect was noted in a study on fundamental Love and Rayleigh waves for nuclear explosions and associated tectonic release (Given and Mellman, 1986). It is important to

understand its effects for discriminating shallow explosive sources for nuclear monitoring, but could also be important in natural systems that have shallow seismicity such as volcanic and geothermal systems, and other manmade shallow seismicity related to mining and oil and gas operations.

In Chapter 3 the potential bias that can arise in the determination of moment tensors for shallow sources is investigated by performing a series of synthetic tests to document and understand the effects of FSVT on the total seismic moment, isotropic seismic moment and the source mechanism. We evaluate the sensitivity of the moment tensor solution as a function of source depth, data quality, frequency bandwidth, and the velocity model. The results of the synthetic studies are then applied to the determination of seismic moment tensors of small industrial chemical explosions. These small chemical explosions are approximately 10 m deep and are recorded at up to several km in distance. Therefore the data represent rather severe source-station geometry in terms of the vanishing traction issues, and is therefore an excellent dataset for improving the understanding of FSVT on source recovery, and in evaluating the discrimination capabilities of the moment tensor method as a function of source depth and frequency passband. We show that the combined method utilizing three-component, complete seismic waveforms and P-wave first motion polarities is able to obtain robust full moment tensor solutions that are comprised predominantly of an isotropic or explosive component. Unlike the synthetic studies, yield estimation using the real quarry blast moment tensor inversion results remains challenging, however the results show that we can put error bounds on our moment and yield estimates using the Network Sensitivity Solutions [NSS] (Ford et al., 2010) approach and that the derived yields are consistent with an empirical relationship obtained from a much larger yield nuclear explosion data set (Stevens and Murphy, 2001).

In source studies it is necessary to assume a velocity structure to compute the needed Green's functions for the inverse problem. Typically it is assumed that a 1D velocity model is adequate, and this is often justified by using long period waves that have wavelengths larger than the spatial extent of the source and much of the heterogeneity in the Earth for the particular path and receiver distance. In seismic source studies (e.g. Dziewonski et al., 1981; Dreger and Helmberger, 1993; Ekström and Nettles, 1997) typically one uses the longest period waves with good signal to noise levels to estimate the seismic moment tensor because the assumptions of the spatio-temporal point-source and the suitability of 1D velocity structure are robust. However even at low-frequency there can be multipath of body and surface waves along particular paths that could lead to bias in moment tensors, and therefore affect the ability to discriminate the source-type of seismic events. In addition, in the monitoring of low yield nuclear explosions noise levels can be high in the traditional moment tensor passband affecting discrimination capability. The desire to extend capability to smaller yields and resolve explosion source depth necessitates the need to incorporate shorter-period data in the analysis. In general the limits of the 1D velocity model assumption is not very well defined in terms of receiver distance and inversion passband, nor is it routinely explored in

the published literature.

As a result of the unprecedented coverage of the NSF EarthScope transportable array (network code TA), a number of high-resolution regional 3D Earth models have been published in the literature (Bensen et al., 2009; Moschetti et al., 2010; Shen et al., 2013; Porritt et al., 2014). These finer resolution regional tomography models may be used to compute Green's functions for regional distance source inversion. In addition, advancements in high-performance, parallel computing, and development of capable numerical 3D wave propagation codes (e.g. Olsen et al., 1995; Pitarka, 1999; Aagaard et al., 2008; Appelo and Petersson, 2009) makes the computation of short period Green's functions for regional scale 3D velocity models a tractable problem. Chapters 4 and 5 utilize the high-performance finite-difference code SW4 (Appelo and Petersson, 2009) and the Western US velocity model of Moschetti et al. (2010), determined from joint inversions of surface wave dispersion maps derived from ambient noise cross-correlation and earthquake data, to investigate the effect of unmodeled 3D velocity structure on moment tensor recovery through synthetic tests, and then by re-examining Western US earthquakes and explosions (Ford et al., 2009a).

In Chapter 4 the assumption of the 1D velocity model as a good approximation for real Earth structure is examined through numerical simulation. Synthetic data are constructed using the 3D velocity model and then the data re constructed for pure double-couple, pure explosion and compound events. The synthetic data are then inverted assuming the regional 1D velocity model for western U.S. (Song et al., 1996). The results indicate that the 1D model assumption is valid for moment tensor inversions at periods up to 10 seconds. Path-calibration, in which source-receiver path specific 1D representations of the 3D structure are utilized can reduce non-double-couple components in earthquakes studies and improve the fit to the data for the three source-types.

In Chapter 5 we develop a platform to perform routine 3D moment tensor inversions. Of the 32 explosions, earthquakes and collapses studied by Ford et al. (2009a), we select six explosions and earthquakes in the vicinity of NTS, and compare the 1D and 3D full moment tensor solutions in different frequency bands. We apply the source-receiver reciprocity principle (Aki and Richards, 2002) to compute 3D Green's functions (Eisner and Clayton, 2001; Graves and Wald, 2001; Zhao et al., 2006). The advantage of seismic reciprocity is a drastic decrease in computation cost, especially when the number of sources outweighs the number of receivers. This approach is very attractive for seismic monitoring where we can set-up a grid of virtual source points across an area of interest and invert for a moment tensor using pre-computed Green's functions at each grid point. The results of the application of 3D Green's functions on the inversion of the explosion and earthquake data show that the 3D model needs further refinement for some paths to model data between 8 to 20 seconds, where the dominant period is around 10 seconds. At longer periods the 3D model improves the fit to the data and the estimated moment magnitude is in better agreement with the reported body wave magnitude.

Finally, in chapter 6 the results from each chapter are summarized and recommendations for future research are provided.

Chapter 2

Source characterization of underground explosions in Eastern Kazakhstan and Northwestern China

Published as: **Source characterization of underground explosions from combined regional moment tensor and first motion analysis** by Andrea Chiang, Douglas S. Dreger, Sean R. Ford, and William R. Walter, published in *Bulletin of Seismological Society of America*.

2.1 Abstract

In this study we investigate the 14 September 1988 US-Soviet Joint Verification Experiment (JVE) nuclear test at the Semipalatinsk test site in Eastern Kazakhstan, and two nuclear explosions conducted less than ten years later at the Chinese Lop Nor test site. These events were very sparsely recorded by stations located within 1600 km, and in each case only 3 or 4 stations were available in the regional distance range. We have utilized a regional distance seismic waveform method fitting long-period, complete, three-component waveforms jointly with first-motion observations from regional stations and teleseismic arrays. The combination of long-period waveforms and first-motion observations provides a unique discrimination of these sparsely recorded events in the context of the Hudson et al. (1989) source-type diagram. We demonstrate through a series of Jackknife tests and sensitivity analyses that the source-type of the explosions is well constrained. One event, a 1996 Lop Nor shaft explosion, displays large Love waves and possibly reversed Rayleigh waves at one station, indicative of a large F-factor due to tectonic release. We show the combination of long-period waveforms and P-wave first motions are able to discriminate this event as explosion-like and distinct from earthquakes and collapses. We further demonstrate the behavior of network sensitivity solutions for models of tectonic release and spall-based tensile damage over a range of F-factors and K-factors.

2.2 Introduction

The use of regional distance long-period, complete waveform data to determine the seismic moment tensor and discriminate the source-type of earthquakes, underground cavity collapse and nuclear explosions has been demonstrated for events in the western United States (Dreger et al., 2008; Ford et al., 2008; Ford et al., 2009a), and for the recent 2006 and 2009 North Korean nuclear tests (Ford et al., 2009b; Ford et al., 2010). In these studies populations of earthquakes, underground cavity collapses and nuclear explosions are found to separate when considered on a Hudson et al. (1989) source-type diagram. The source type plot simplifies the moment tensor into two parameters that depend on the eigenvalues of the moment tensor. These parameters T and κ describe the deviation from a pure double-couple (DC) in terms of non-volumetric (compensated linear vector dipole, CLVD) and volumetric components. Ford et al. (2010) utilized the Hudson et al. (1989) source-type representation to develop a network sensitivity solution (NSS), which tests on the order of 100 million moment tensor solutions uniformly distributed in source-type space to determine the best fitting solution, the uncertainty in the solution, and the capabilities of the method given the topology of a recording station network. The regional distance moment tensor inversion, coupled with NSS analysis, and the characterization of sensitivities and uncertainties due to random errors and systematic velocity model errors enable the discrimination of source-type in relatively sparse regional distance monitoring.

We investigate the 14 September 1988 US-Soviet Joint Verification Experiment (JVE) nuclear test at the Semipalatinsk test site in Eastern Kazakhstan, and two nuclear explosions conducted less than ten years later at the Chinese Lop Nor test site (Table 2.1). These events were very sparsely recorded by stations located within 1600 km, and in each case only 3 or 4 stations were available in the regional distance range for moment tensor analysis. Following the results of Ford et al. (2012) we incorporated first-motion data from the regional stations, as well as teleseismic stations to provide additional constraint in the NSS analysis. The results show that unique discrimination of these events is possible under these extremely sparse monitoring conditions when long-period regional waveforms and P-wave first-motion polarities are combined.

2.3 Data Processing and Methods

Data and instrument response for the US-Soviet Joint Verification Experiment (JVE) and Lop Nor nuclear tests were downloaded from the Incorporated Research Institutions for

Table 2.1: Event Information

	1988 JVE	1995 Lop Nor	1996 Lop Nor	1999 Lop Nor EQ
Origin Time (UTC)	03:59:57.30	04:06:00.20	02:56:00.06	03:51:05.42
Latitude	49.882	41.553*	41.5804*	41.674
Longitude	78.882	88.7496*	88.6893*	88.463
Depth (km)	< 1.0	0.7*	0.5*	17
m_b†	6.1	6.1	5.9	5.9
M_s‡	4.8	5.0	4.3	5.3
M_w	5.2	5.2 to 5.4	5.2	5.3
F	0.97 to 1.15	3.79 to 4.20	-12.75 to -20.44	
K	2.59 to 2.73	2.80 to 2.88	2.81 to 2.90	
T	-0.87 to -0.91	-0.82 to -0.83	-0.62 to -0.66	0.1424
κ	0.57 to 0.59	0.56 to 0.57	0.36 to 0.39	0.0540

* Waldhauser et al. (2004)
† Priestley et al. (1990); Yang et al. (2003)
‡ ISC catalog (explosions); NEIC catalog (earthquakes)

Seismology (IRIS) that consists of a collection of stations from the regional broadband seismic network in China, the Global Seismic Network (GSN), and other temporary networks (Figure 2.1a). In addition to data from IRIS for the 1988 Soviet JVE, we also have data from temporary deployments of short period instruments located at near-regional distances < 260 km (Priestley et al., 1990) and the Borovoye station (BRVK) at a distance of 690 km. The data was instrument corrected, integrated to displacement, rotated to radial and transverse components, and filtered between 12.5 to 80 seconds with an Butterworth filter depending on instrument type and signal-to-noise levels (SNR). Table 2.2 lists the stations used for each event, and the frequency passband that was employed. The processed data were then inverted using the time domain full waveform moment tensor inversion of Minson and Dreger (2008). For JVE we used a source depth of 1 km that gives the highest goodness of fit between data and synthetics, and for the two Lop Nor events we used the source depths from Waldhauser et al. (2004). We then inverted the data with Green's functions computed for a range of source depths to determine the source depth sensitivity.

The seismic moment tensor consists of nine force couples that represent the equivalent body forces for seismic sources of different geometries (Jost and Herrmann, 1989), that due to conservation of angular momentum reduce to six independent couples and dipoles. The data are represented by the convolution of Green's functions for a given Earth model, source terms and the moment tensor elements. The individual moment tensor elements are obtained using a generalized least square inversion and the goodness of fit between the data

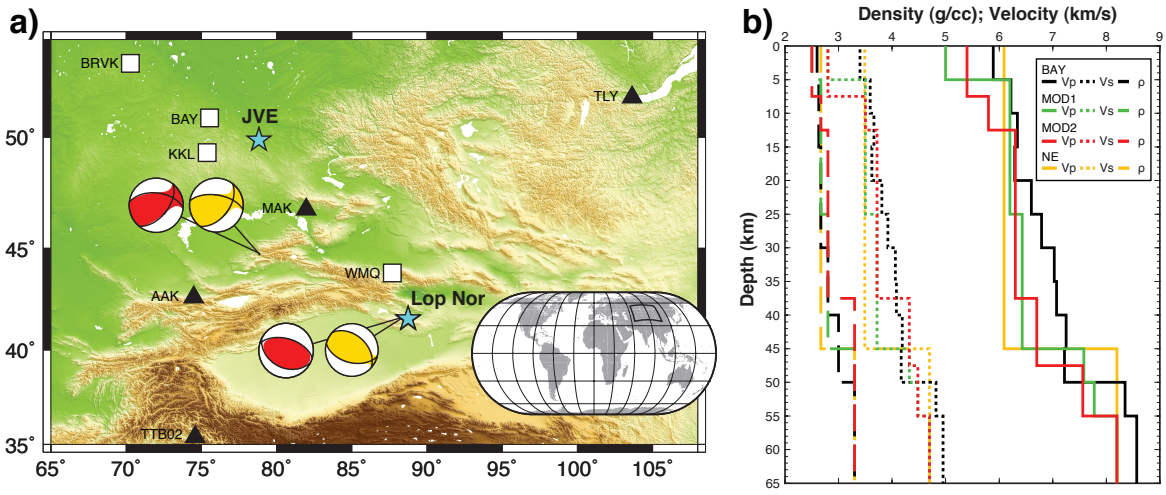

Figure 2.1: (a) Event locations (stars) and seismic stations (triangle and square) used in the moment tensor analysis. The two Lop Nor events are located very close together, hence the overlapping stars. Triangles represent the stations used in the analysis of the 15 May 1995 Lop Nor explosion and 8 June 1996 Lop Nor explosions, and squares are the stations used in the 14 September 1988 U.S.Soviet Joint Verification Experiment (JVE). Focal mechanisms of local earthquakes used in the velocity model calibration are also plotted, with the solution from this study (right) and Global Centroid Moment Tensor solution ([GCMT],left).(b) Velocity models used in the analysis: BAY from Walter and Ammon (1993); MOD1 from broadband waveform modeling of local earthquakes in (a); MOD2 is a 1D model simplified from a 3D surface wave tomography model (Sun et al., 2010); NE is a simple layer over halfspace model.

and synthetics is measured by the variance reduction (VR) given by:

$$VR = \left(1 - \frac{\sum_i (d_i - s_i)^2}{\sum_i {d_i}^2}\right) \times 100 \tag{2.1}$$

where d represents the data and s represents the synthetic waveforms. Because the data are linear combinations of the Green's functions weighted by their associated moment tensor elements, we need a well-calibrated velocity model in order to estimate robust seismic source parameters. For each test site we utilized several published seismic velocity models, and for some paths we additionally calibrated models by modeling earthquake records. The inversion method also allows for small time shifts between the data and Green's functions to compensate for errors in origin time, location, and in velocity structure.

In addition, we use two alternative methods in order to fully characterize the source solution space. One utilizes a grid search to find the best-fitting double-couple (DC), pure-

isotropic/explosion (ISO), or DC+ISO source mechanism. The other, described below, utilizes a moment tensor grid search in order to assess solution uniqueness and resolution of source-type.

Although the seismic moment tensor inversion gives a unique moment tensor solution, the decomposition of the moment tensor solution is non-unique. Therefore we implemented the Hudson et al. (1989) source-type representation that circumvents the need to decide on a particular moment tensor decomposition scheme. The source-type diagram has two key parameters T = -2ε and κ on the x- and y-axis, respectively, given by the two equations:

$$\varepsilon = \frac{-{m_1}'}{|{m_3}'|} \tag{2.2}$$

$$\kappa = \frac{M_{ISO}}{|M_{ISO}| + |{m_3}'|} \tag{2.3}$$

${m_1}'$ and ${m_3}'$ are the deviatoric principal moment associated with the minimum and maximum principal compressive stress axes, and MISO is the isotropic moment. Equation 2.2 measures the deviation from a pure shear dislocation and equation 2.3 describes the volume change. In this convention, ε is 0 for a pure DC source and $\pm$0.5 for a pure CLVD source, and κ is $\pm$1 for a spherical explosion and implosion, respectively. Understanding the relative contributions of the different moment tensor elements provides insights into the complex source processes of explosions as well as other seismic events. This representation of the seismic source has been shown to result in separate populations for explosions, underground cavity collapse and earthquakes (Dreger et al., 2008; Ford et al., 2008; Ford et al., 2009a; Ford et al., 2009b) enabling discrimination capability.

To assess the confidence of the moment tensor solution, we implemented the Network Sensitivity Solution (NSS) technique developed by Ford et al. (2010). The technique presents the level of fit between actual data and the different theoretical solutions described by the source-type diagram for a given station configuration, Earth model, and frequency band. From the NSS of a given event we can determine whether or not the best fitting full moment tensor solution from the inversion is well-resolved to make useful interpretations about the source. We included regional and/or teleseismic P-wave first motions in addition to waveform data in the NSS analysis to better constrain the moment tensor solution. To include P-wave polarities as additional constraints, we take the suite of synthetic moment tensor solutions from the previous waveform NSS, compute their P-wave polarities, and compare them to the observed P-wave polarities. We assign -1 for downward motion and $+1$ for upward motion. The VR is calculated as:

$$VR = \left(1 - \frac{\sum \left(Pol_{obs} - Pol_{synth}\right)^2}{\sum {Pol_{obs}}^2}\right) \times 100 \tag{2.4}$$

Then we calculate the combined waveform and first motion VR as:

$$VR = (sVR_{reg} \times sVR_{fm}) \times 100 \tag{2.5}$$

where sVR_{reg} and sVR_{fm} are normalized by the maximum regional waveform and first motion VR, respectively. The take-off angles are calculated using iaspei-tau (Snoke, 2009) and the iasp91 reference Earth model (Kennett and Engdahl, 1991). Incorporating the first motion data proves to be a powerful tool eliminating solution non-uniqueness, and in assessing the confidence of a solution under sparse station coverage monitoring situations. We find that additional polarity constraints assist by uniquely discriminating the events as predominantly explosive.

This powerful result is due to the fact that the tradeoff between a pure explosion and −CLVD (Ford et al., 2012) only occurs for a −CLVD in which the compressional major vector dipole is vertically oriented. For these two sources and combinations of the two, the surface wave radiation patterns are identical for Rayleigh waves, and are theoretically null for Love waves. This vertical CLVD mechanism predicts dilational first motions in the center of the focal sphere. For explosions, the incorporation of P-wave first motion data, particularly teleseismic observations with low takeoff angle proves to be an effective test against the negative CLVD source type. Naturally challenges remain for cases with low SNR in P-waves, or cases in which free-surface reflections, or interactions with nearby velocity structure result in reversed dilational polarities. Furthermore, the absence of good P-wave polarities from teleseismic arrays or stations may require the use of regional seismic waveform data alone. Nevertheless, as will be shown in the following, even in such regional distance, sparse coverage situations, the combination of low-frequency full waveform fits with regional distance P-wave first-motions, greatly enhances the discriminatory power of the method.

2.4 Results: Source Characterization

2.4.1 14 September 1988 Soviet Joint Verification Experiment (JVE)

Our analysis of the Soviet JVE event included three stations in Eastern Kazakhstan and one station in northwestern China. Stations BAY and KKL are filtered between 12.5 to 20 seconds, station BRVK is filtered between 12.5 to 30 seconds, and station WMQ is filtered between 20 to 50 seconds. The use of station-specific filters allows tailoring of the approach for path specific SNR, and with respect to the suitability of the velocity model used to compute the Green's functions. We used a well-calibrated velocity model BAY (Walter and Ammon, 1993) for the Eastern Kazakhstan stations and tested two models for the path to the Chinese station WMQ. The two models used for station WMQ are from broadband waveform

Table 2.2: Station Information

Event	Station	Passband (s)	Distance (km)	Azimuth (∘)
1988 JVE	BAY	12.5 - 20	255	257
	KKL	12.5 - 20	256	295
	BRVK	12.5 - 30	690	304
	WNQ	20 - 50	953	132
1996 Lop Nor	MAK	30 - 50	794	319
	AAK	30 - 80	1184	280
	TTB02	30 - 50	1410	246
1999 Lop Nor EQ	WMQ	30 - 50	246	346
	PDG	30 - 50	760	287
	MAKZ	30 - 50	770	320
	TLG	30 - 50	940	284
	TLY	30 - 50	1602	41

modeling of two local earthquakes in Kazakhstan and the Lop Nor nuclear test site, called MOD1 (Figure 2.1b), and another 1D model simplified from surface wave tomography (Sun et al., 2010), called MOD2. Figure 2.1b shows all the velocity models used in this paper to calculate the Green's functions and generate the synthetic seismograms. Table 2.3 shows the 1D velocity models used in this study. We have both regional P-wave first motions including the four stations used in the waveform inversion (Walter and Patton, 1990; Priestley et al., 1990), and teleseismic P-wave first motions from the Adirondack array in New Hampshire, reported by Battis and Cipar (1991), and Gauribidanur array in India.

The best fitting source mechanism from full moment tensor inversion of regional waveforms consists of a predominantly explosive component and a moment magnitude (M_w) between 5.21 and 5.25, depending on the velocity model used. The calculated moment used the convention for total moment described by Bowers and Hudson (1999). M_w falls close to the surface wave magnitude (M_s) in the catalog because the frequency range we used in the inversion is dominated by long period surface waves. Respective VRs for a full, deviatoric, DC, DC+ISO, and ISO mechanism are 84-85%, 79-80%, 75-76%, 81-82%, and 77-78%. Variations in VR resulted from different velocity models (MOD1 and MOD2) used for WMQ. The goodness of fit between data and synthetics are similar for the five different moment tensor decompositions shown in Figure 2.2, due to the dominance of surface waves and the presence of Love waves, but a pure DC solution has the lowest VR as compared to the other four decompositions that are either purely isotropic or included an isotropic component.

We computed the NSS using three different combinations of data sets: (1) from regional waveforms, (2) combined waveform, regional and teleseismic P-wave first motions, and (3)

Table 2.3: Velocity Models

Model	Thickness (km)	V_p (km/s)	V_s (km/s)	Density (g/cc)
BAY*	5	5.89	3.40	2.60
	5	6.22	3.59	2.63
	5	6.34	3.66	2.63
	5	6.29	3.62	2.67
	5	6.60	3.81	2.67
	5	6.79	3.92	2.67
	5	7.03	4.06	2.80
	5	7.07	4.08	2.80
	5	7.25	4.19	3.00
	5	7.22	4.17	3.00
	5	8.35	4.82	3.00
	∞	8.57	4.95	3.00
MOD1	5	5.00	2.80	2.50
	20	6.20	3.50	2.67
	20	6.43	3.72	2.80
	5	7.58	4.32	3.30
	5	7.776	4.48	3.30
	∞	8.20	4.70	3.30
MOD2	7.5	5.40	2.80	2.50
	5	5.80	3.50	2.67
	25	6.30	3.72	2.80
	10	6.70	4.32	3.40
	7.5	7.56	4.48	3.30
	∞	8.20	4.70	3.30
NE	45	6.09	3.49	2.67
	∞	8.20	4.70	3.30

* Walter and Ammon (1993)

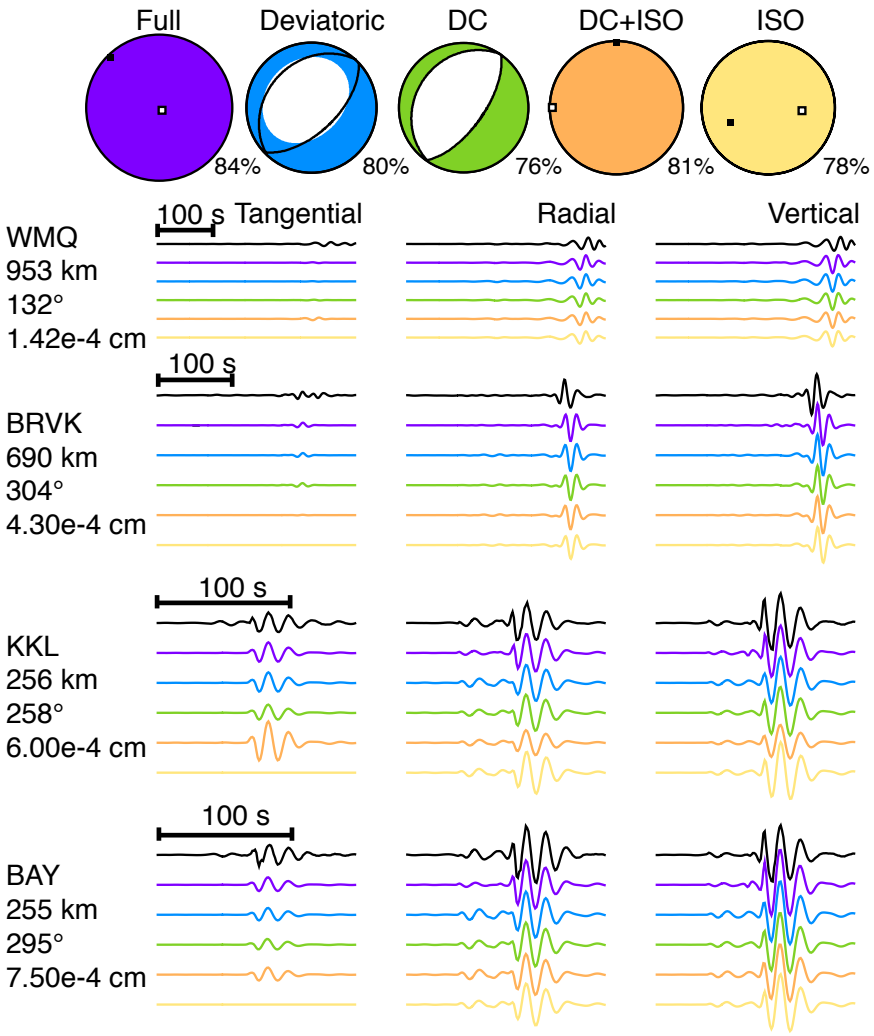

Figure 2.2: 1988 Soviet JVE Source Model and Waveform Comparisons. The top trace is the observed waveform data and the rest are synthetic waveforms according to their corresponding source mechanisms (The order from top to bottom is: data, full, deviatoric, double-couple [DC], DC+isotropic [ISO], and ISO). Station name, source-receiver distance, azimuth and maximum amplitude are shown. Associated variance reduction (VR) for each source type is plotted next to their focal mechanisms. Data shows small Love waves on the tangential component, characteristic of an explosion. We show results using Green's functions calculated from MOD2 for WMQ.

combined waveform and four regional P-wave first motions. We also compare the NSS using different Earth models MOD1 (Figure 2.3a-c) and MOD1 + MOD2 (Figure 2.3d-e) to compute the Green's functions. The regional waveforms only NSS solution (Figure 2.3a,d) shows a similar trend compare to other nuclear explosions, such as the NTS events and the two DPRK tests (Ford et al., 2010), with the best-fitting full moment tensor solution plotting near the theoretical opening crack mechanism and there being a trend in the best fitting region extending to the negative CLVD. The shaded contour regions correspond to different scaled variance reduction (sVR) in which the sVR in Figure 2.3 is scaled to the moment tensor solution in the NSS that has the maximum VR. Moment tensor solutions fitting $\geq$ 90% sVR covers the upper right half of the Hudson source type plot, whereas solutions fitting $\geq 98\%$ sVR wraps around a small region around the theoretical opening crack and includes the best fitting mechanism from the full moment tensor inversion. In the case of using just the waveform data, source mechanisms without a significant explosive component can fit the observed data just as well as a predominantly explosive mechanism (Figure 2.3a,d). However, when regional and teleseismic P-wave (Figure 2.4) first motions are included in the computation of the NSS a solution that is predominately explosive is obtained (Figure 2.3b,e). The NSS results show significant improvement in discrimination capabilities when we included additional constraints from P-wave first motions, especially for moment tensor solutions fitting better than sVR of 90%. Figure 2.3c,f suggests including just the regional P-wave polarity measurements from the same four stations used in the waveform inversion can greatly increase discrimination capabilities, which is good since good teleseismic data may not always be available. The additional constraints from P-wave first motions eliminate the common ISO-CLVD tradeoff as well as the mechanisms that do not agree with both the higher frequency polarity data and the long period waveforms.

2.4.2 15 May 1995 Lop Nor Shaft Explosion

In contrast with the 1988 Soviet JVE, the Lop Nor events studied here had only three available regional stations with adequate SNR in the intermediate- to long-periods employed by our method, and therefore this case presents a very sparse monitoring scenario. We used broadband waveform data filtered between 30 to 50 seconds period from three stations in Eastern Kazakhstan, Eastern Kyrgyzstan and Central Siberia. For the furthest station TLY in Siberia we used a simple layer over halfspace velocity model, NE. This model was obtained using forward and inverse modeling of a local earthquake in Lop Nor, the same earthquake used to obtain MOD1. We used the iasp91 crustal velocity as a starting model, and from our modeling result we observe that because of the distance and long periods the waves are not sensitive to the finer details of the velocity model, and additional layers to the halfspace model do not improve the waveform modeling results significantly. For station AAK in Kyrgyzstan we used MOD1, and for station MAK in Kazakhstan we tested both MOD1 and MOD2. The original instrument response file for MAK from IRIS resulted in anonymously low waveform amplitudes. After comparing the coda envelope functions with nearby stations

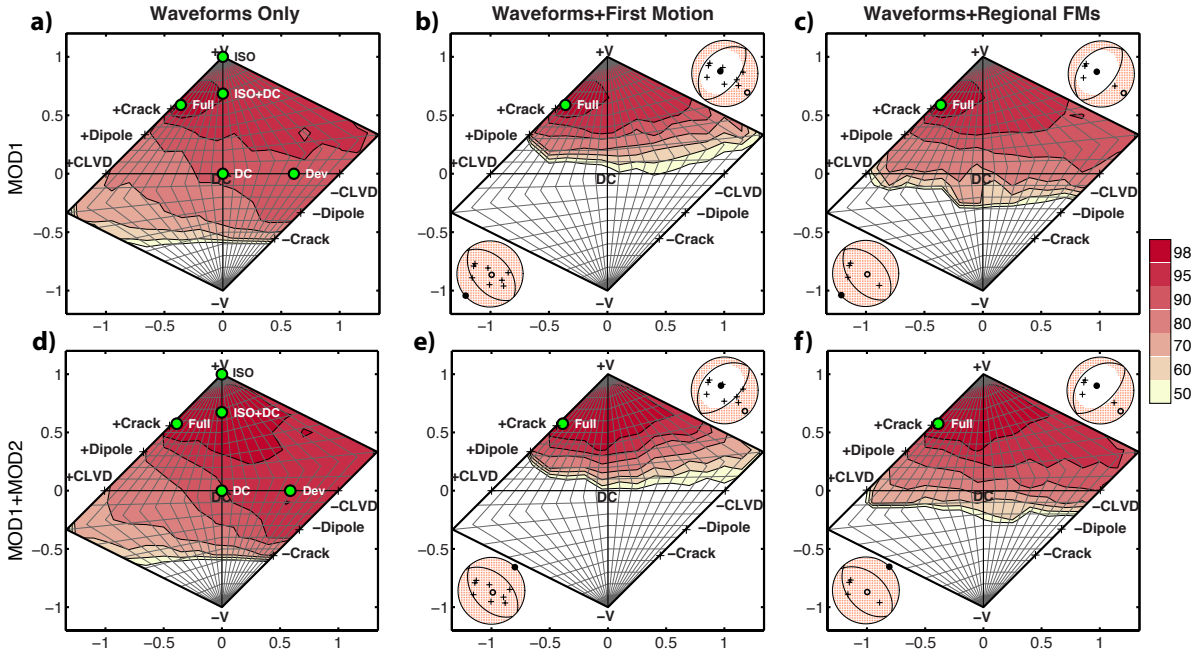

Figure 2.3: Network sensitivity solution (NSS) for the 1988 U.S.Soviet JVE. Circles are source mechanisms from Figure 2.2; crosses are the theoretical mechanisms; shaded regions are full moment tensor solutions contoured according to their scaled variance reduction (sVR). Best-fitting full and deviatoric mechanisms are also plotted. Black crosses, open circles, and circles plotted on top are P-wave up first motions, T- and P-axes. (a-c) NSS using MOD1. (d-f) NSS using MOD1 and MOD2.

we concluded the original response file could not be used because the amplitude of the coda envelope function for MAK is significantly shifted from all other nearby stations, indicative of a problematic instrument response. Rautian and Khalturin (1978) observed that coda envelope functions decay stably over time, and amplitudes only vary from event to event. Instead we used a response file from the previous date for the analysis. The first motion picks for the 1995 Lop Nor event are all from regional stations obtained through IRIS, including the three stations used in the moment tensor inversion (Figure 2.4).

The best fitting full moment tensor is a predominantly explosive mechanism and has comparable VR to the deviatoric, DC and DC+ISO mechanisms, but a pure ISO source does not fit well. Respective VRs for a full, deviatoric, DC, DC+ISO and ISO mechanisms are 81-86%, 76-78%, 73-74%, 74-78%, and 10%, depending on the velocity model used for MAK. A pure explosive source cannot generate Love waves to fit the large observed Love wave amplitudes on the tangential component, and therefore the pure explosion model has the anonymously low VR of 10% (Figure 2.5a). This is of concern since natural tectonic

earthquakes represented by a DC actually fit better than the pure explosion, however in similarity to the JVE, a pure DC solution has the lowest VR compared to other decompositions that include an ISO component (excluding a pure ISO source). Difficulty fitting the relatively small Rayleigh waves on radial and vertical components at AAK is likely caused by Love wave multipathing based on the particle motions. Surface waves on the radial and vertical components exhibit horizontally polarized Love wave particle motion. The best fitting full moment tensor solution is located near the opening crack mechanism on a Hudson source type plot. This result is consistent with the JVE event and previously studied nuclear explosions (Ford et al., 2010). The waveform only NSS results show a wide range of possible sources fitting $\geq 90\%$ of the best fitting moment tensor solution (Figure 2.5b,d), which is largely the result of the large Love wave amplitudes and the sparse station coverage. However, if we use both waveform data and P wave polarities observed at regional distances we see the combined analysis significantly reduces the distribution of solutions with high sVR ($\geq 90\%$) and uniquely discriminates the event as consistent with other nuclear explosions and inconsistent with earthquakes and collapses (Figure 2.5c,e). Figure 2.5c,e shows that the DC and deviatoric mechanisms that can fit the surface wave data well fail to fit the first motions at the sites. Velocity model variations also show some variation in the NSS as expected; however, the distribution of sources fitting $\geq 98\%$ of the best fitting solution is similar for both velocity models illustrating that the approach is capable of source type discrimination even in cases where the earth structure is not as well constrained.

2.4.3 8 June 1996 Lop Nor Shaft Explosion

For the second Lop Nor event we used regional waveform data from three broadband stations MAK in Kazakhstan, AAK in Kyrgyzstan, and TTB02 in northeastern Pakistan, and displacement data and synthetics are filtered between 30 to 50 seconds, 30 to 80 seconds and 30 to 50 seconds, respectively. For AAK and TTB02 we used MOD1 to calculate the Greens functions, and for MAK we used both MOD1 and MOD2 since its location falls within the surface tomography study of Sun et al. (2010). We used P-wave first motions at regional distances and one station at teleseismic distances (Figure 2.4). All stations are obtained from IRIS. The qualities of the picks are good and most show impulsive upward P-wave first motions on the vertical components. The 1996 Lop Nor event has a slightly smaller mb of 5.9 reported in the catalog compared to the 1995 Lop Nor event, which has an mb of 6.1. The M_w from the regional moment tensor inversion is around 5.2 depending on the velocity models used (Table 2.1). Similar to that of the 1995 event we observe significant Love waves on the tangential component. Because of the strong Love waves the goodness of fit between data and synthetic for a pure ISO solution could not fit the data well ($<10\%$ VR) and the best fitting mechanism is an implosion instead of an explosion. To further explore how a pure isotropic solution fits the data, we searched for the best fitting ISO mechanism using the vertical displacement only. A pure implosion mechanism fits station TTB02 and AAK at 44% VR and 51% VR, respectively with a seismic moment of 1.7×10^{22} dyne-cm,

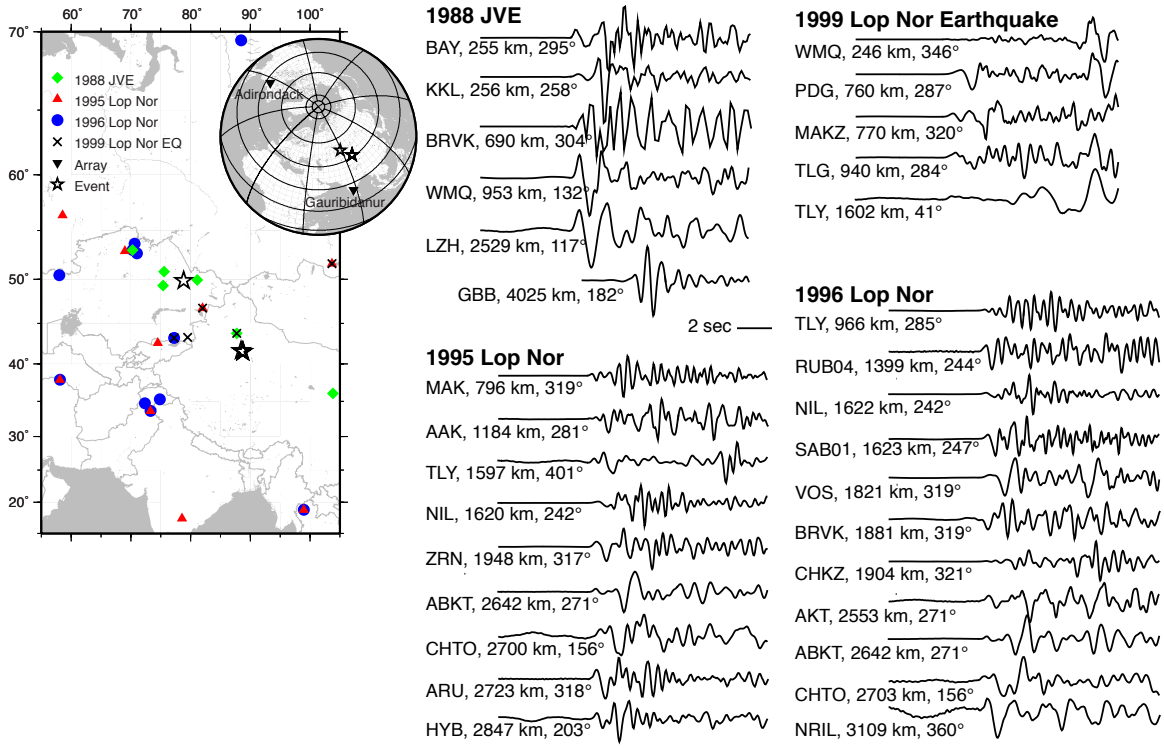

Figure 2.4: P-wave first motions for the earthquake and three explosions. The waveforms are band-pass filtered between 0.2 and 3 Hz, except BRVK for the 1988 JVE, which is filtered between 0.2 and 1.5 Hz to avoid exceeding the Nyquist frequency. P-wave polarities at KSU and the Adirondack array data (not shown here but used in the JVE analysis) are from Priestley et al. (1990) and Battis and Cipar (1991), respectively. All waveforms are in velocity except for the 1988 JVE event, which is shown as displacement. The map shows the distribution of stations and array beams for the three events. The Gauribidanur array beam (GBB) is filtered between 0.8 and 5 Hz.

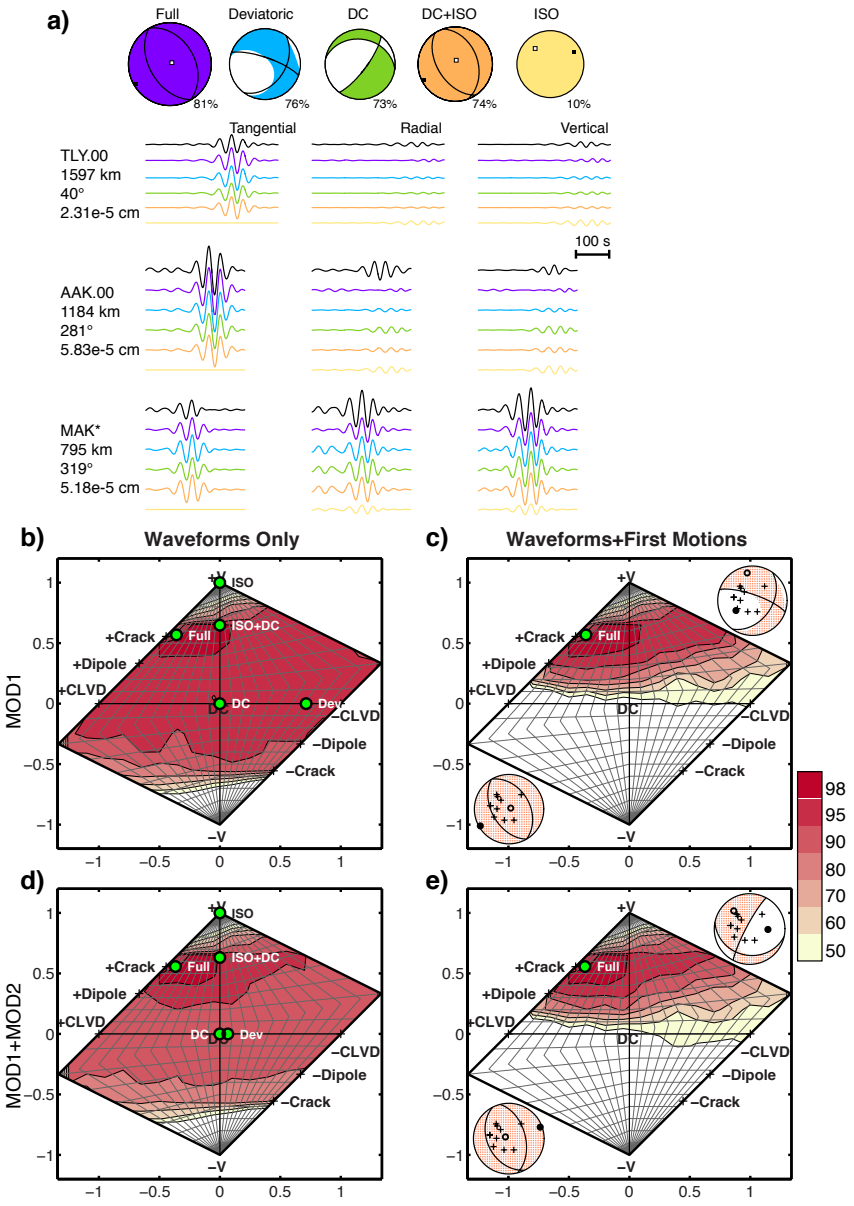

Figure 2.5: (a) The 1995 Lop Nor source model and waveform comparisons. The top trace is the observed waveform data and synthetic waveforms according to their corresponding source mechanisms. Associated VR for each source type is plotted next to their focal mechanisms. Data shows big Love waves on the tangential component.We show results using Green's functions calculated from MOD1 for MAK. (b-e) NSSs for the 1995 Lop Nor explosion. Circles are the best-fitting full, deviatoric, pure DC, ISO+DC, and pure ISO source mechanisms; crosses are the theoretical mechanisms; shaded regions are full moment tensor solutions contoured according to their sVR. Crosses, open circles, and filled circles plotted on top are P-wave up first motions, T and P axes. (b and c) NSS using MOD1; (d and e) NSS using MOD1 and MOD2.

but does not fit station MAK, in fact the synthetic is phased-shifted by $\pm\pi$ from the data. Significant contribution from non-isotropic sources resulted in poor fits to the data when we assume a purely isotropic source. It is possible that the tectonic release for this event is large and likely caused Rayleigh wave reversals (Toksöz and Kehrer, 1972; Ekström and Richards, 1994) thus the pure ISO mechanism is more implosive rather than explosive (Figure 2.6a). Rayleigh wave reversals due to large tectonic release have been observed in other nuclear explosions as well, such as the 1998 Indian test (Walter and Rodgers, 1999).

The full and deviatoric solutions for the 1996 Lop Nor event have comparable VR at 78% but are not significantly higher than the best fitting pure DC and ISO+DC mechanisms that have VR at 73% (Figure 2.6a). However, a vertical dip-slip mechanism is an uncommon shallow crustal earthquake. The majority of near-vertical or sub-horizontal dip-slip mechanisms in the Harvard Global Centroid Momnet Tensor (GCMT) catalog are associated with subduction and spreading centers. We expect the waveform only NSS result cannot uniquely discriminate the 1996 event as a predominantly explosive source due to the strong Love waves and sparse station coverage. This is indeed the case and the waveform only NSS shows many different moment tensor solutions have high $sVR \geq 90\%$, and although the NSS contours with $sVR \geq 98\%$ includes mostly explosion-like mechanisms it also extends downward and crosses into the horizontal deviatoric axis that is not observed in the 1996 event (Figure 2.6b,d). This behavior is likely due to Rayleigh wave reversal. However, after we incorporated regional P-wave first motions the combined NSS results now show similar trends as observed in the 1995 Lop Nor test and the 1988 Soviet JVE, though the difference is contours showing solutions with $sVR \geq 90\%$ are more extensive and cross slightly over to the horizontal deviatoric line (Figure 2.6c,e). Although the 1996 Lop Nor combined waveform and first motion NSS does not give a unique discrimination, it identifies the source as non-DC. Unlike earthquakes, the distribution of moment tensor solutions is not situated around the pure DC mechanism but shifted along the vertical volumetric axis and towards an opening dipole. The best fitting full moment tensor for the 1996 Lop Nor explosion lies close to the opening dipole, whereas for the Lop Nor earthquake the solution lies close to the DC. Although the 1996 Lop Nor event is not uniquely discriminated as a predominantly explosive source, NSS shows the event is unusual and unlike a typical earthquake that needs further analysis to fully characterize its source process. The earthquake shown in Figure 2.7 is one of earthquakes used to obtain MOD1, located close to the Lop Nor test site and at 17 km depth. Five stations were available in Eastern Kazakhstan and central Siberia for the inversion (Figure 2.7a) and NSS (Figure 2.7b-c) but the data are nosier compare to the explosion data.

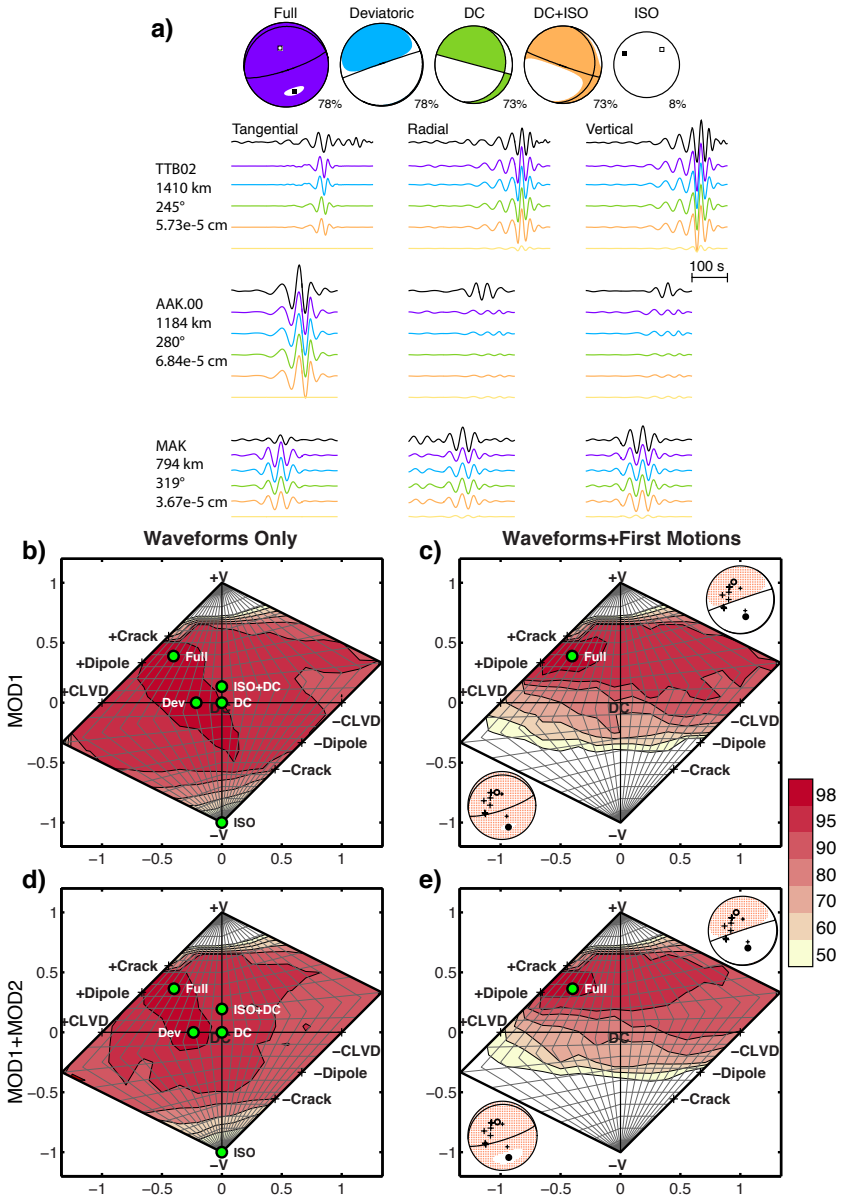

Figure 2.6: (a) The 1996 Lop Nor source model and waveform comparisons. The top trace is the observed waveform data and synthetic waveforms according to their corresponding source mechanisms. Associated VR for each source type is plotted next to their focal mechanisms. Data shows big Love waves on the tangential component.We show results using Green's functions calculated from MOD1 for MAK. (be) NSSs for the 1996 Lop Nor explosion. Circles are best-fitting full, deviatoric, pure DC, ISO+DC, and pure ISO source mechanisms; crosses are the theoretical mechanisms; shaded regions are full moment tensor solutions contoured according to their sVR. Crosses, open circles, and filled circles plotted on top are P-wave up first motions, T and P axes. (b and c) NSS using MOD1; (d and e) NSS using MOD1 and MOD2.

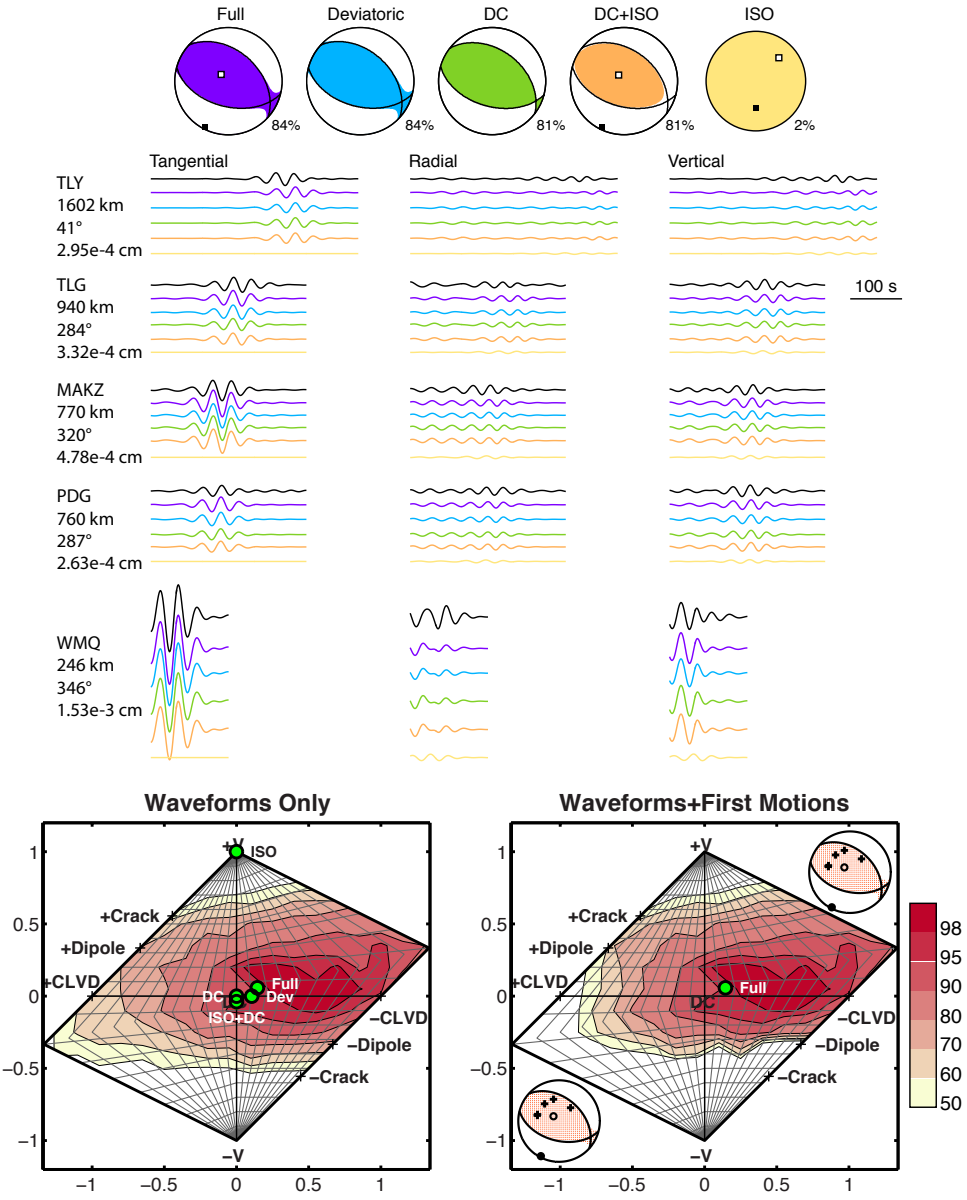

Figure 2.7: Waveform fits and NSSs for the 30 January 1999 earthquake near the Lop Nor test site. The distribution of solutions resembles the Little Skull Mountain aftershock (Ford et al., 2010) but with the center of the bullseye shifted to the right, toward the −CLVD. The station coverage is slightly better than the Lop Nor explosions with additional stations to the west, giving a better azimuthal coverage.

2.5 Discussion

2.5.1 Sensitivity to Station Geometry and Source Depth

Manmade explosions are conducted at shallow depths. For the 1988 Soviet JVE we used a source depth of 1.0 km and for the two Lop Nor shaft explosions we used initial source depths reported in Waldhauser et al. (2004), which were estimated using the relationships between mb, yield, and source depth. To test our method's sensitivity to source depth we performed regional waveform moment tensor inversion using a suite of Green's functions calculated at source depths ranging from 0.2 km to 16 km. Unlike tectonic earthquakes, explosions have much shallower source depth, generally < 1 km. Therefore, source depth can be a very useful discriminant for earthquakes and explosions.

Plotting all of the best fitting full moment tensor solution with additional constraints from P-wave first motions at different depths on a Hudson source-type plot (Figure 2.8), we see the sVR gets much worse as source depth increases. The 1988 JVE and 1995 Lop Nor event solutions with high sVR and shallow depths (< 1 km) are centered at the theoretical opening crack mechanisms. In comparison, source depth for the 1996 Lop Nor event is less constrained. Higher uncertainty from the Green's functions (path between the event and station TTB02) and possibly greater tectonic release for this event may have resulted in less sensitivity to source depth. We did not specifically model the path between the event and station TTB02, hence greater errors may be introduced into the calculation of the Green's functions. Although the 1996 Lop Nor event source depth is not as well constrained as the other two events in this paper, most of the high VR solutions are shallow and the mechanisms are close to an opening linear vector dipole. Solutions at greater depths are not explosive but also have lower VR.

In addition to depth sensitivity, we also performed Jackknife tests for the three events to discern the inversions' sensitivity to station geometry. The Jackknife tests reveal we need at least three stations to have confidence in the moment tensor solution. Solutions obtained using less than three stations are not stable, and depending on station geometry can give you incorrect source mechanism. Generally moment tensors computed using stations closer to the source ($\sim 300 - 700$ km, as in the case of JVE) resolve more isotropic component and can better constrained the NSS, regardless of the total number of stations used in the inversion.

2.5.2 Effects of Tectonic Release and Damage Source Medium

The presence of shear waves in seismic recordings of nuclear explosions indicates the explosion process is complex and involves other source processes such as interactions with the free-surface, the effects of shockwave and relaxation of tectonic strain (Patton and Taylor,

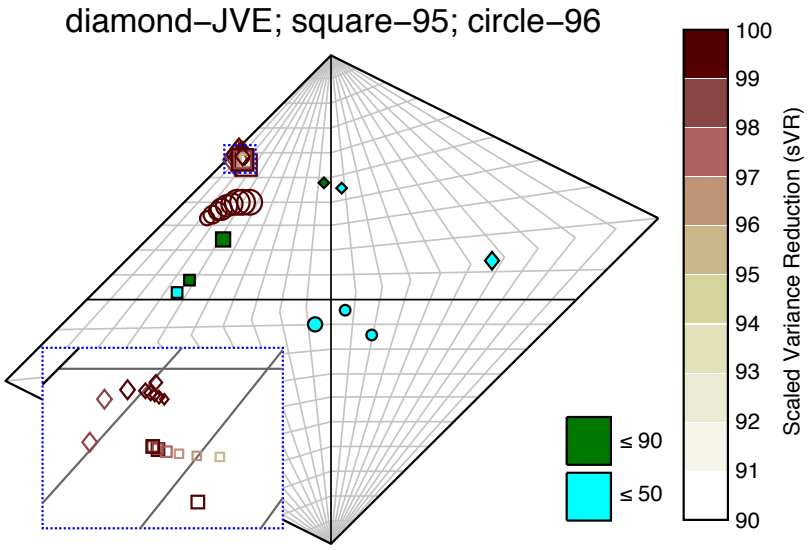

Figure 2.8: Source depth sensitivity for the three events analyzed. Best-fitting full moment tensors for the 1988 JVE (diamond), 1995 Lop Nor (square), and 1996 Lop Nor (circle) events based on regional waveform inversion and P-wave first-motion constraints. Size of the symbol increases with decreasing source depth, filled symbols have $sVR \leq 90\%$, and open symbols have $sVR > 90\%$.

2011; Toksöz et al., 1965; Toksöz and Kehrer, 1972; Burger et al., 1986; Day et al., 1987). Recent studies (Ben-Zion and Ampuero, 2009; Patton and Taylor, 2011) have suggested that significant contributions to the radiated seismic wavefield can arise from source medium damage. Material damage associated with explosions affects the Rayleigh wave radiation pattern (Patton and Taylor, 2008), therefore damage may have significant implications to source-type discrimination. Our combined waveform and first motion analysis of the Lop Nor tests shows the regional moment tensor is a promising method for source-discrimination even when tectonic release is large. The best fitting solutions located in the region between a pure explosion and tensile crack on the source type diagram is comparable to solutions for the DPRK (Ford et al., 2009b; Ford et al., 2010) and NTS explosions (Ford et al., 2009a), and is consistent with the nature of tensile damage above the shot point due to spall and other free surface interactions as proposed by Patton and Taylor (2008). To further assess the capabilities of regional moment tensor on events with tectonic release or source damage, we conducted a series of synthetic tests to examine these effects.

Two types of composite sources were tested: (1) a ISO+DC source and (2) a ISO+CLVD source. The ISO+DC source examines the effects of tectonic release and consists of an explosion and a 45-degree dipping reverse fault mechanism. The ISO+CLVD source examines the effects of source medium damage and consists of an explosion and a CLVD mechanism

with a vertically oriented major vector dipole (Patton and Taylor, 2008) To describe the relative seismic moments between the different source types, we used the relationships proposed by Toksöz et al. (1965) for tectonic release and Patton and Taylor (2008) and Patton and Taylor (2011) for material damage from a deviatoric source. The index F measures the ratio between isotropic moment (M_{ISO}) and double-couple moment (M_{DC}),

$$F = 1.5\frac{M_{DC}}{M_{ISO}} \tag{2.6}$$

The index K measures the relative strengths of the moment tensor elements,

$$K = \frac{2M_{zz}}{M_{xx} + M_{yy}} \tag{2.7}$$

and when tectonic release occurs only in the horizontal plane as in our second test case,

$$K = \frac{2\left(M_{ISO} + M_{CLVD}\right)}{2\left(M_{ISO} - M_{CLVD}\right)} \tag{2.8}$$

We used the 1988 Soviet JVE station geometry and Green's functions from our moment tensor analysis to compute the synthetic data, and added real noise collected from the stations used in the Soviet JVE analysis or from other nearby IRIS stations when pre-event seismic recordings are not available. For the two composite sources (ISO+DC and ISO+CLVD) we tested different F-factors and K-factors, and for each factor we looked at different SNRs at 5%, 10%, 15% and 20% of the maximum vertical Rayleigh wave amplitude. We performed the synthetic testing using long period waveforms only, and another one combining the waveforms and four P-wave first motion measurements recorded at the same seismic stations. For the remaining part of this section we focused on results from the tests where SNR is 20% of the maximum vertical Rayleigh wave amplitude. This is the most extreme case of SNR and generally the real data we use have SNR levels that are much lower than 20%. The distribution of individual moment tensor solutions $\geq 98\%$ sVR in the Hudson et al. (1989) source-type diagram are more compacted for lower SNR levels, but the contours outlining all possible points are very similar for all SNR levels. This observation applies to both composite source cases we tested.

The ISO+DC composite source case shows the waveform only NSS becomes more constrained with increasing contribution from tectonic release (Figure 2.9). Best-fitting full moment tensor solutions center around the opening crack mechanism, which is consistent with solutions obtained from real explosions. Although this seems counterintuitive, the NSS gives a predominantly explosive source because the contribution from a reverse fault mechanism helps eliminate the well-known ISO-CLVD tradeoff between explosion and $-$CLVD. The reverse fault radiation pattern is more similar to a +CLVD mechanism. Hence, the two competing mechanisms eliminate the ISO-CLVD tradeoff. Best-fitting full moment tensor solutions of different degree of tectonic release are all near the opening crack mechanism,

which is consistent with solutions obtained from real explosions. The waveforms only NSS and combined waveform and first motion NSS show very similar distribution for $sVR \geq 98\%$. We see no significant improvement by adding first motions because the waveforms only NSS already uniquely identifies the source as predominantly explosive. However, first motions do help constrain the NSS for solutions with $sVR \geq 90\%$, due to the fact that the P-wave radiated from the explosion is primary and precedes motions due to secondary block faulting (delay time between explosion and secondary faulting is 1 second), or tensile damage above the shot point. By using both long period waveforms and P-wave polarities we can capture the volumetric signature of the event when tectonic release has significant contribution to the explosion source processes. In the event that we cannot uniquely discriminate the event as explosive, the deviation from deviatoric mechanisms flags the event as uncommon and warrants further analysis to understand its source processes.

To look at the effects of medium source damage, we adopted the model proposed by Patton and Taylor (2008) where the cause of damage is represented by a vertically oriented CLVD source. The deformation observed at the source with this model is extensional along the vertical axis and horizontal compressions around the explosion (+CLVD). As defined by Patton and Taylor (2008), a K-factor of 1 means contribution from CLVD vanishes to zero, $K > 1$ means extension along the vertical axis, and $K < 1$ means compression along the vertical axis. Our synthetic tests with just waveform data show $K > 1$ (implying greater material damage) reduces the commonly observed ISO-CLVD tradeoff (Figure 2.10). This is the result of competing mechanism between the −CLVD and +CLVD, increasing contribution from a +CLVD source mechanism affects the Rayleigh wave radiation pattern thus enhancing the explosive characteristics of the source. In contrast, $K < 1$ where compressional deformation is along the vertical axis the ISO-CLVD tradeoff persists. In some cases when K is high (≥ 2.5) the NSS identifies the event as explosive even without additional constrains from P-wave first motions. In other cases where the event is not uniquely identified as explosive, additional P-wave first motions improve the solution by shifting the 98% sVR contours above the deviatoric CLVD mechanism and reducing the region of possible source mechanisms.

2.6 Conclusions

We have performed seismic moment tensor inversions for the 1988 Soviet JVE test and two Lop Nor nuclear tests. These cases represent sparse monitoring conditions and/or uncertainty in velocity structure. In each case we have shown that the use of long-period waveform data comprised mostly of regional surface waves result in solutions with large isotropic components that are consistent with solutions for other studied nuclear tests (Ford et al., 2009a; Ford et al., 2009b; Ford et al., 2010). Using only regional waveforms, the distribution of solutions on the source type diagram of Hudson et al. (1989) do not cleanly discriminate the

event either because of the known explosion −CLVD tradeoff (case of the JVE event) or due to large observed Love waves (cases of the two Lop Nor tests). In each case, however, the inclusion of regional P-wave polarities, and ideally observations from teleseismic arrays when available, reduces area of solutions that provide a good level of fit to the data, providing good separation from double-couple solutions and solutions on the deviatoric line.

The 8 June 1996 Lop Nor test indicates that Rayleigh waves may be reversed at some of the regional stations due to a large tectonic release. The large tectonic release is possibly due to shock driven block faulting or tensile damage (Patton and Taylor, 2008). To further investigate this we carried out a series of synthetic tests using the JVE station geometry to evaluate the regional moment tensor method capabilities for different levels of tectonic release measured by both the Toksöz F index and the Patton K index. These tests show that the combination of long-period regional waveform data and regional distance P-wave first motions are able to resolve the anomalous volumetric nature of compound explosion tensile damage and block faulting events.

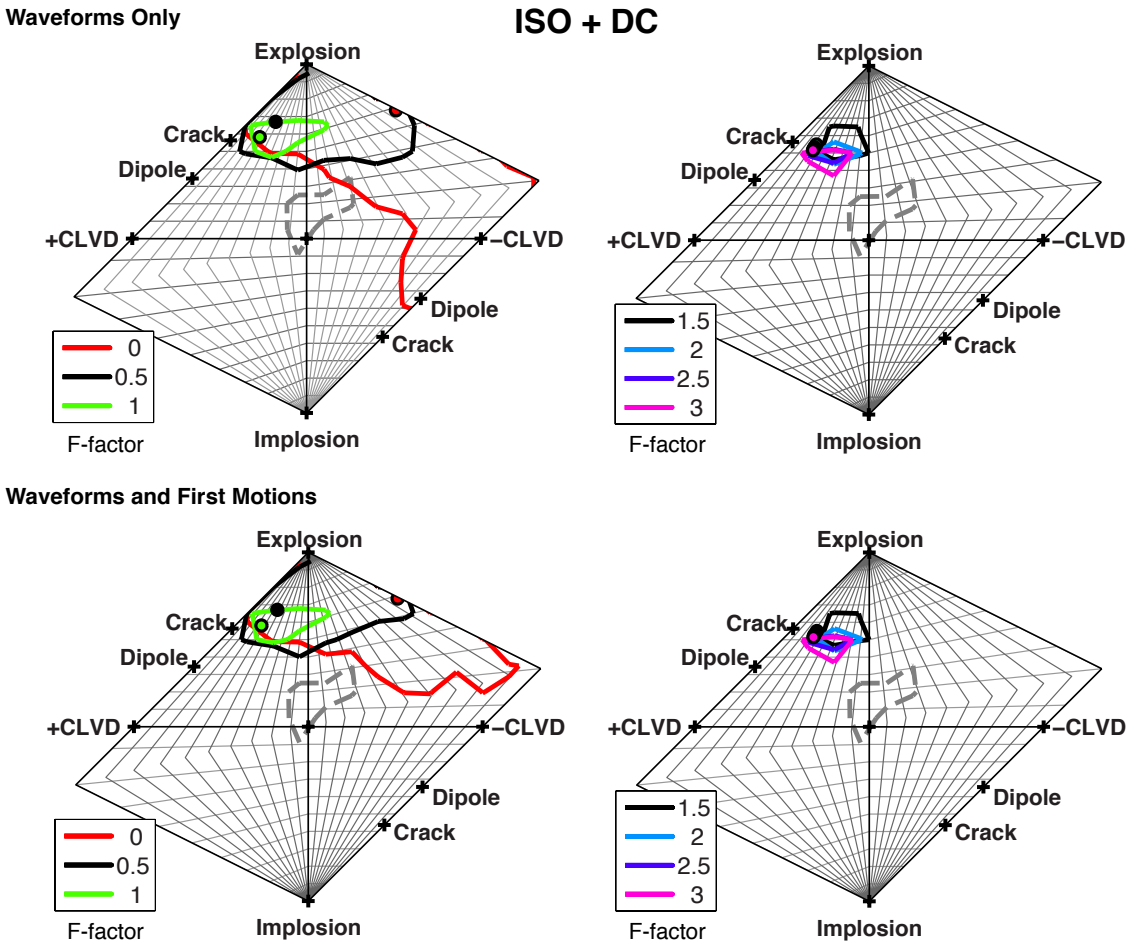

Figure 2.9: NSSs for an ISO+DC composite source. Plotted are the 98% sVR contours with increasing F-factor (therefore increasing contribution from the DC component), and dashed contours are from a pure reverse-fault (DC) mechanism. The circles are the best-fitting full moment tensor solution from waveform inversion. Here, we compare how the NSS changes when additional P-wave first motions are included.

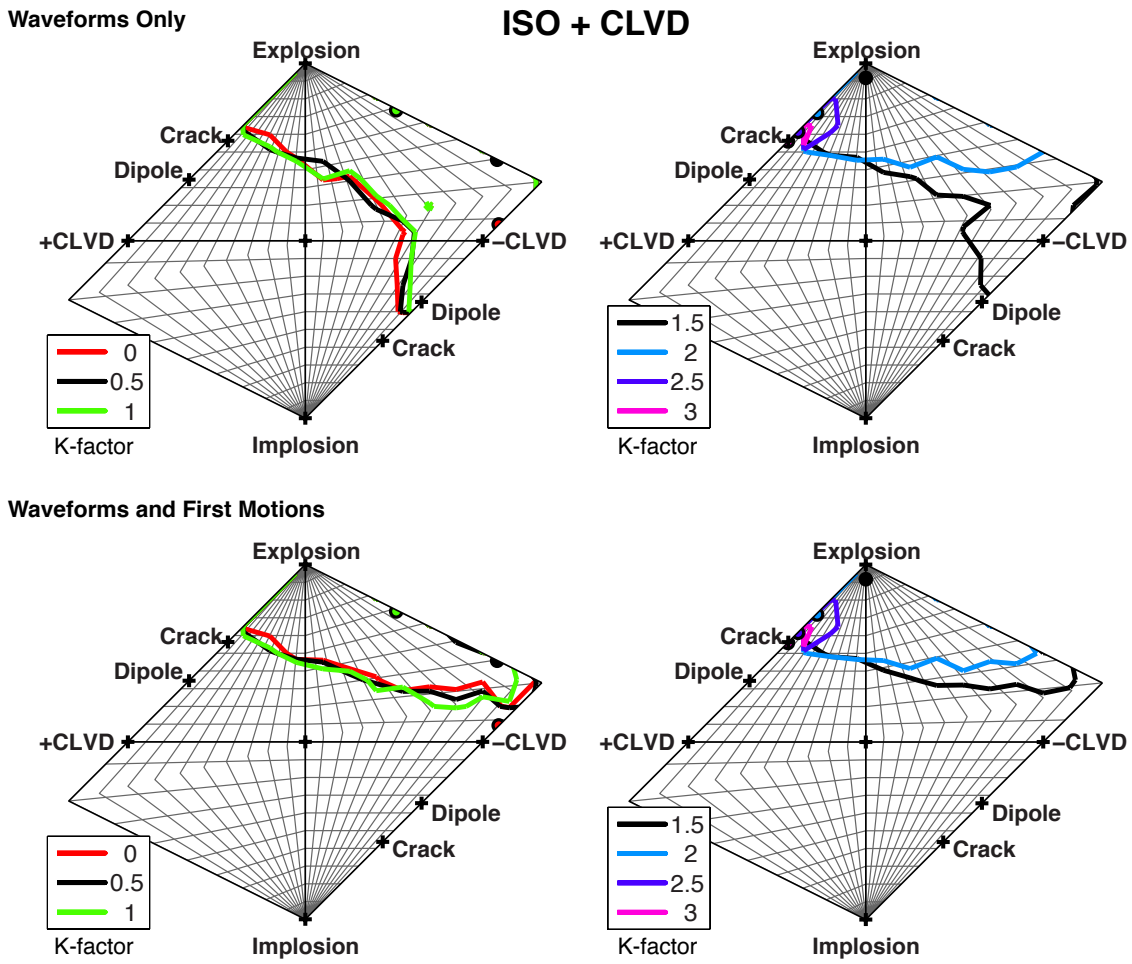

Figure 2.10: NSSs for an ISO+CLVD composite source. Plotted are the 98% sVR contours with increasing K-factor (therefore increasing contribution from the CLVD component). The circles are the best-fitting full moment tensor solution from waveform inversion. Here, we compare how the NSS changes when additional P-wave first motions are included.

Chapter 3

Moment Tensor Analysis of Shallow Sources

3.1 Abstract

A potential issue for moment tensor inversion of shallow seismic sources is that some moment tensor components have vanishing amplitudes at the free surface, which can result in bias in the moment tensor solution. The effects of the free-surface on the stability of the moment tensor method becomes important as we continue to investigate and improve the capabilities of regional full moment tensor inversion for source-type identification and discrimination. It is important to understand these free surface effects on discriminating shallow explosive sources for nuclear monitoring purposes. It may also be important in natural systems that have shallow seismicity such as volcanoes and geothermal systems. In this study, we examine the effects of the free surface on the moment tensor via synthetic testing, and apply the moment tensor based discrimination method to the HUMMING ALBATROSS quarry blasts. These shallow chemical explosions at approximately 10 m depth and recorded up to several kilometers distance represent rather severe source-station geometry in terms of vanishing traction issues. We show that the method is capable of recovering a predominantly explosive source mechanism, and the combined waveform and first motion method enables the unique discrimination of these events. Recovering the correct yield using seismic moment estimates from moment tensor inversion remains challenging but we can begin to put error bounds on our moment estimates using the Network Sensitivity Solution (NSS) technique (Ford et al., 2010).

3.2 Introduction

Waveform inversion to determine the seismic moment tensor is now a standard method for determining the source mechanism of natural and man-made seismicity, and can identify, or

discriminate different types of seismic sources. Such source-type identification is important for better understanding the physical processes of explosions as well as other man-made seismicity and earthquakes from geothermal (Guilhem et al., 2014), and volcanic environments (Templeton and Dreger, 2006; Minson et al., 2007) and oil and gas operations (McNamara et al., 2015). For the nuclear explosion discrimination problem the uncertainty in a given solution is as important as the best fitting parameters and it is therefore necessary to fully understand and model possible bias that can result in such inversions. A potential issue for shallow seismic sources that are effectively at the free surface is that as the traction vanishes the associated vertical dip-slip (DS) Green's functions (GFs) have vanishing amplitudes (Julian et al., 1998; Stevens and Murphy, 2001), which in turn can result in the indeterminacy of the M_{xz} and M_{yz} components of the moment tensor and therefore lead to bias in the moment tensor solution. The free-surface effect was noted in a study on fundamental Love and Rayleigh waves for nuclear explosions and associated tectonic release (Given and Mellman, 1986). The effects of the free surface on the stability of the moment tensor becomes important as we continue to investigate and improve the capabilities of regional full waveform moment tensor inversion for source-type identification and discrimination. It is important to understand its effects for discriminating shallow explosive sources for nuclear monitoring, but could also be important in natural systems that have shallow seismicity such as volcanic environments and geothermal systems, and other manmade shallow seismicity related to anthropogenic activities such as hydraulic fracturing and mining.

To investigate the potential issues that could arise in the estimation of moment tensors for shallow sources, we perform a series of synthetic tests to document and understand the effects of free surface vanishing traction (FSVT) on the total seismic moment, isotropic seismic moment and the source mechanism. We evaluate the sensitivity of the moment tensor solutions as a function of source depth, data quality, frequency and velocity model. Based on what we learn from the synthetic studies, we applied the moment tensor method to the HUMMING ALBATROSS quarry blast events, this is an excellent dataset in terms of understanding the effects of FSVT and evaluating the discrimination capabilities of the moment tensor method as a function of source depth and frequency. These small chemical explosions are approximately 10 m deep and are recorded at up to several km distances. Therefore the data represent rather severe source-station geometry in terms of vanishing traction issues. We show that the combined method utilizing both complete seismic waveforms and P-wave first motion polarities is able to obtain robust full moment tensor solutions that are comprised predominantly by an isotropic or explosive component. However, unlike the synthetic studies, yield estimation using the real quarry blast moment tensor inversion results remains challenging.

3.3 Methods

The seismic moment tensor consists of nine force couples that represent the equivalent body forces for seismic sources of different geometries (Jost and Herrmann, 1989), which due to conservation of angular momentum reduce to six independent couples and dipoles. The data (e.g. displacement waveforms) are represented by the convolution of GFs for a given Earth model, the source time function, and the moment tensor elements. Because relatively long-period waves are used in the inversion we assume that the source time function is an impulse. We obtain the individual moment tensor elements by inverting the 3-component, complete waveform data using a time domain, generalized least square inversion (Minson and Dreger, 2008), and the goodness of fit between the data and synthetics is measured by the variance reduction (VR):

$$VR = \left(1 - \frac{\sum_i w_i \left(d_i - s_i\right)^2}{\sum_i w_i {d_i}^2}\right) \times 100, \tag{3.1}$$

where d is the data, s is the synthetic waveforms and w is the inverse distance weighting at each station i. Because the data are linear combinations of the GFs weighted by their associated moment tensor elements, one major source of error in the inverted moment tensor solution comes from the assumed velocity model. A well-calibrated velocity model is important to obtain robust estimates of the source parameters. For HUMMING ALBATROSS we used the 1D velocity model by Saikia et al. (1990) computed from Rg wave dispersion, and calculated the GFs using frequency-wavenumber integration (Wang and Herrmann, 1980; Herrmann and Wang, 1985; Herrmann, 2013). The inversion method also allows for small time shifts between the data and GFs to compensate for uncertainties in origin time, location, and velocity structure. To properly account for non-double-couple radiation we used the Bowers and Hudson (1999) formulation to calculate the moment magnitude.

To assess the full uncertainties in the moment tensor inversion and avoid the need to decide on a particular moment tensor decomposition scheme, we examine the moment tensor solution in terms of the maximum fit surface called Network Sensitivity Solutions [NSS] (Ford et al., 2010). The NSS presents the goodness of fit between data and a suite of moment tensor solutions for a given station configuration, Earth model, and frequency band. We contoured the populations of best-fitting moment tensor solutions that have VR equal and above a certain threshold. In descending order, the contours map out the solutions that have VRs of 98%, 95%, 90%, 80%, 70%, 60%, and 50% of the maximum VR in the NSS population. From the NSS of a given event we can determine whether or not the best-fitting full moment tensor solution from the inversion is well resolved to make useful interpretations about the source. The maximum fit surface is parameterized and represented in the source-type space (Hudson et al., 1989; Tape and Tape, 2012a; Tape and Tape, 2012b; Vavryčuk, 2015). In essence the source-type diagram is a graphical representation of the full moment tensor eigenvalues. The source-type diagram has two key parameters γ and δ, which are the longitude and latitude

of a lune on the unit sphere (Tape and Tape, 2012a; Tape and Tape, 2012b):

$$tan\gamma = \frac{-\lambda_1 + 2\lambda_2 + \lambda_3}{\sqrt{3}\,(\lambda_1 - \lambda_3)}, \tag{3.2}$$

$$cos\delta = \frac{\lambda_1 + \lambda_2 + \lambda_3}{\sqrt{3\left({\lambda_1}^2 + {\lambda_2}^2 + {\lambda_3}^2\right)}}, \tag{3.3}$$

$$\delta = \frac{\pi}{2} - \beta. \tag{3.4}$$

β is the colatitude and λ_{1-3} are the eigenvalues of the full seismic moment tensor where $\lambda_1 \geq \lambda_2 \geq \lambda_3$. Equation 3.2 measures the deviation from a pure shear dislocation and equation 3.3 and 3.4 describes the volume change.

In this convention when $\delta = 0$ (no volume change): $\gamma = 0$ describes a pure double-couple (DC) source and $\pm\frac{\pi}{6}$ describes a pure compensated-linar-vector-dipole (CLVD) source; and $\gamma = 0$ and $\delta = \pm\frac{\pi}{2}$ represents a spherical explosion (+V) and implosion (−V), respectively. Understanding the relative contributions of the different moment tensor elements provides insights into the complex source processes of explosions as well as other seismic events. This representation of the seismic source has been shown to result in separate populations for explosions, underground cavity collapse and earthquakes (Ford et al., 2009a; Ford et al., 2009b; Dreger et al., 2008; Ford et al., 2008; Chiang et al., 2014) enabling discrimination capability.

Instead of the original forward-modeling approach by Ford et al. (2010) we implemented the damped least square inversion scheme by Nayak and Dreger (2015) to compute the NSS. This method significantly reduces the computation time, and recovers a true maximum fit surface in the source-type space. In addition to long period waveform data we include P-wave first motion polarities in the NSS calculations as additional constraints (Ford et al., 2012; Guilhem et al., 2014; Chiang et al., 2014). The damped least square inversion finds the moment tensor solutions that best fit both the complete waveform data and the P-wave first motion polarities. Similar to comparing synthetic waveforms to data, we compare the theoretical P-wave first motions against the observed polarities. We assign −1 for downward motion and +1 for upward motion, and each observed polarity is weighted by the quality of the pick. The first motion VR is calculated as:

$$VR = \left(1 - \frac{\sum_i w_i \left(Pol_{obs} - Pol_{synth}\right)^2}{\sum_i w_i {Pol_o bs}^2}\right) \times 100. \tag{3.5}$$

The final combined VR (Eq. 3.5) is computed by weighing the two data sets equally. Incorporating the first motion data proves to be a powerful tool in reducing solution uncertainties. Constraints from first motion can reduce uncertainties due to the theoretical ISO-CLVD (Isotropic-CLVD) tradeoff (Ford et al., 2012; Chiang et al., 2014), sparse station coverage

(Chiang et al., 2014), illuminate possible complexities in earthquake ruptures in geothermal environments (Guilhem et al., 2014), and as illustrated later in this study, free surface effects at shallow depths. We find that the additional polarity constraints assist by uniquely discriminating the events as predominantly explosive and greatly enhance the discriminatory power of the moment tensor-based method.

3.4 Free-Surface Vanishing Traction

We generate the ten fundamental GFs at a distance of 100-km from the source and with source depths ranging from 0.2 to 1.2 km. We apply an acausal bandpass Butterworth filter at 10 to 50 seconds to filter the GFs. As shown in Figure Figure 3.1a we see a strong source depth dependency on the vertical dip-slip (DS) fundamental GFs associated with the M_{xz} and M_{yz} elements for all three components: vertical (ZDS), radial (RDS) and transverse (TDS) in which there is a systematic reduction in displacement amplitude with decreasing source depth. The averaged Fourier spectral amplitude shows a linear relationship between the source depth and DS waveform amplitudes (Fig. 3.1b). In contrast, the vertical strike-slip GFs for all three components (ZSS, RSS and TSS) and the explosion GFs for the vertical and radial components (ZEX, REX) show little to no variation in amplitude and waveform with respect to decreasing source depth. The vertical and radial 45-degree dip-slip GFs (ZDD and RDD) show variations in amplitude as well due to the constructive and destructive interference of waves interacting with the free surface. While the wave interference appears minor in the 10 to 50 second period passband (Fig. 3.1a) it is more pronounced in the unfiltered displacement GFs.

Since traction perpendicular to the vertical vanishes at the free surface, the inversion may not resolve the M_{xz} and M_{yz}, as well as the isotropic components M_{xx}, M_{yy}, M_{zz} of the moment tensor. It is important to note however that while there are strong effects on amplitude, the waveforms remain similar and there is little effect on the phase of the waveforms of these components. The systematic behavior of the GF suggests that it may be possible to scale the isotropic moment (M_{ISO}) to recover the correct moment, enabling a more robust estimate of the explosive yield. But because the ability to resolve seismic waveforms at the free surface depends on the velocity model, frequency band, station configuration and background noise level, it is necessary to understand the behavior of the moment tensor inversion for each particular monitoring scenario in order to correct for bias in the seismic moment. Poor station coverage and low signal-to-noise ratio (SNR) will decrease the method's ability to fit the observed waveforms and resolve the problematic moment tensor component.

In the synthetic study we examine the ability to recover the correct moment tensor elements by generating a suite of velocity models derived from a 1D western U.S. velocity reference model (Song et al., 1996). We choose this particular model as a reference because

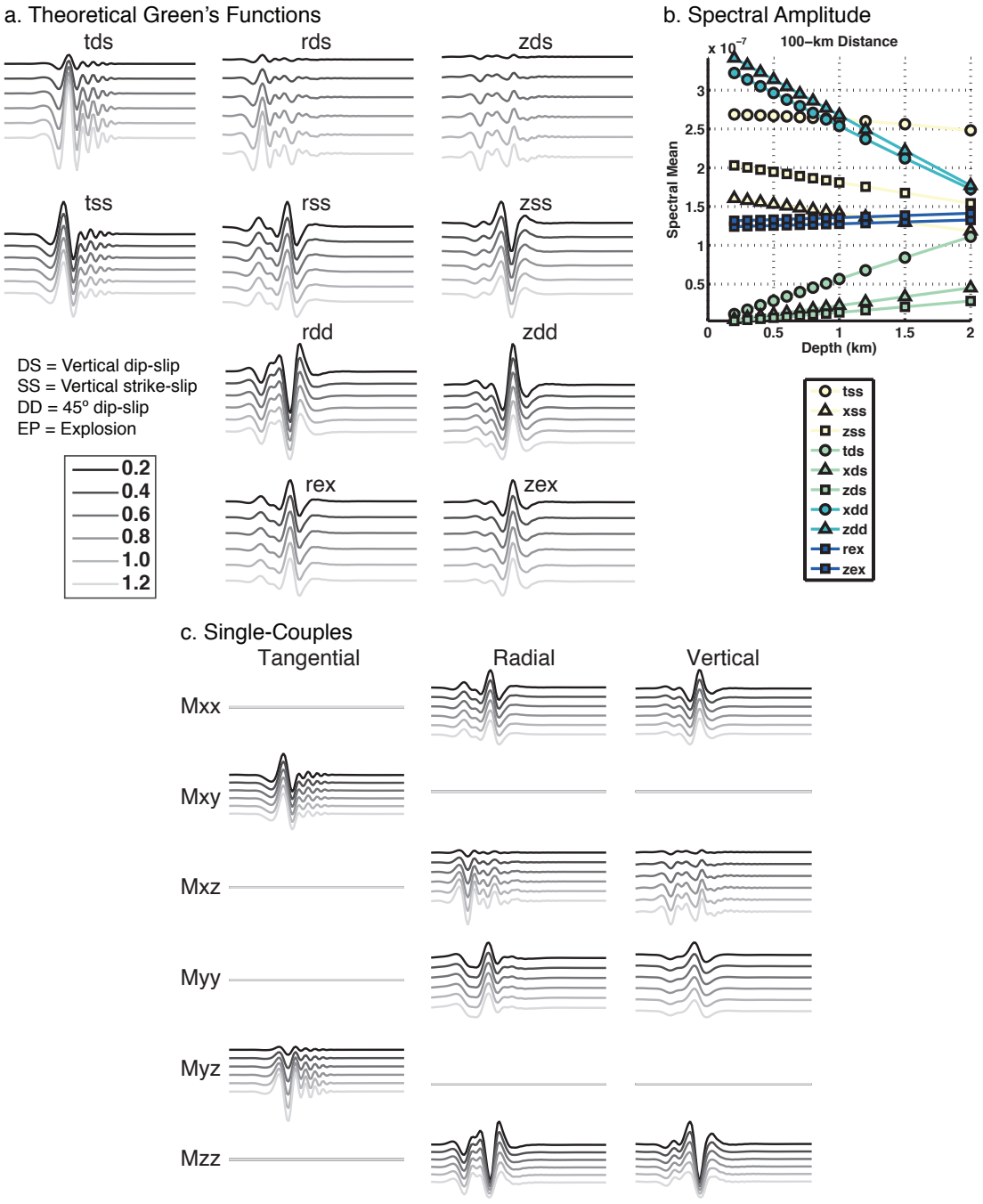

Figure 3.1: (a) Computed using the Song et al. (1996) 1D western U.S. velocity model. Green's functions are in displacement and filtered between 10-50 second period. The traces for each component, from top to bottom, are at 200, 400, 600, 800, 1000, and 1200 m source depths. (b) Averaged spectral displacement amplitudes between 10 to 50 seconds for the ten fundamental Green's functions. (c) Moment tensor elements computed using the same velocity model and filtered between 10-50 second period.

it was used to model the NTS explosions in Ford et al. (2009a). We generated the suite of models by splitting the top 2.5-km thick layer in the reference model into two separate layers. We systematically adjust the thickness and velocity of the two new layers (Fig. 3.2), but constrain the perturbations of the two parameters (velocity and layer thickness) to maintain the same vertical travel time as the reference model. The reason to maintain the same vertical travel time is to generate different but comparable velocity models and to minimize travel-time differences. For each 1D model, we generate displacement GFs at regional distances between 100 and 400 km with source depths ranging from 0.2 to 3.5 km. Using the same set of GFs we generate two types of synthetic data with different source mechanisms: 1) a pure explosion case (EXP) and 2) a composite source case (DC and EXP) with a DC to EXP ratio of 2:3. We compute the synthetic data following the expressions from Minson and Dreger (2008), and add random Gaussian white noise. We scale the amplitude of the random noise for a given SNR using the following equation:

$$SNR = 20 \log_{10} \left(\frac{RMS_{signal}}{C_{noise} RMS_{noise}} \right) \tag{3.6}$$

The scaling factor C_{noise} is calculated for a given SNR using the root mean squared (RMS) amplitudes of the signal and noise, then the noise-included data and GFs are bandpass-filtered between 10 to 50 seconds using an acausal Butterworth filter. To model after real-life monitoring capabilities we use an SNR of 10 but also tested different SNRs. We implemented a semi-ideal four-station coverage for the moment tensor inversion, consisting of source-to-receiver distances at 100, 200, 300 and 400 km, and distributed in semi-regular azimuths.

In this test we keep the source depths of the synthetic data and the GFs used in the inversion the same to isolate the effect of only vanishing traction for shallow depth of burial. Of the 59 velocity models tested the full moment tensor inversion successfully recovers the correct mechanism for both the pure explosion case and the composite case over the targeted depth range (< 1 km) for nuclear explosions, as well as at deeper depths. Given the same filter parameters and station configuration, models that have a thick continuous layer generally have larger deviations in the moment estimates, whereas the more gradient-like models show little to no change. Figure 3.3 shows the sensitivity of total and isotropic scalar moment with respect to source depth. At the shallowest depths (< 0.5 km), for the pure explosion case the M_{ISO} estimates all fall within about 10% of the input values (Fig. 3.3a), whereas the total moment varies even less. The composite case exhibits greater deviations from the input value at the shallowest source depths, however all moment estimates are within about 20% of the input values (Fig. 3.3b). In general the seismic moment estimates approach the correct value as the source depth increases. The M_{zz} component is not as well constrained, thus affecting the method's ability to resolve the M_{ISO}. In most cases the FSVT has little effect on recovering the correct mechanism for models with a shallow velocity gradient. However, as the noise level increases the bias in the seismic moment and mechanism also increases. The key observation from the synthetic tests is that the bias in the recovered moment and source mechanism of very shallow sources depends on various factors, including the velocity

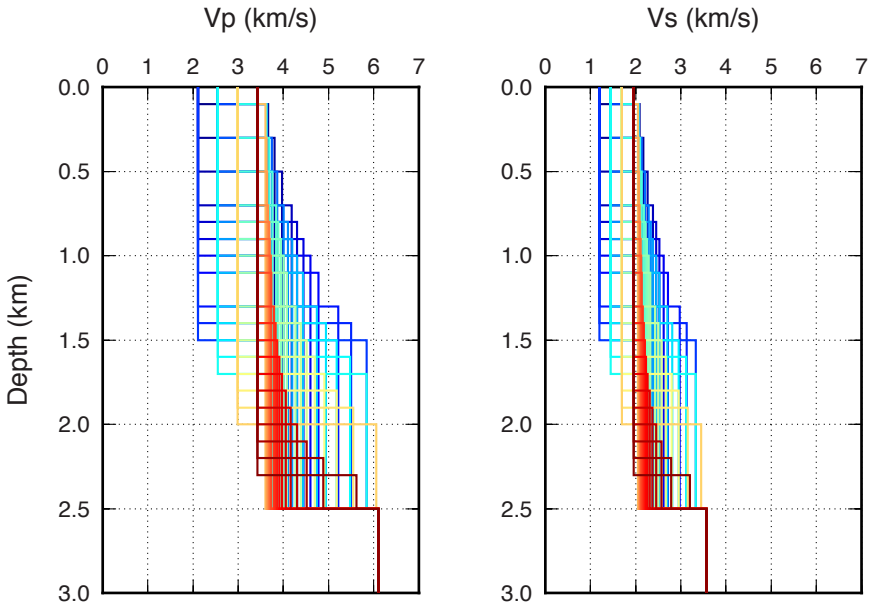

Figure 3.2: Derived from the Song et al. (1996) 1D model by keeping the top 2.5-km vertical travel time constant. The model parameters are the same below 2.5-km depth.

model.

In practice when we perform moment tensor inversions the source depth is also tested because we do not know the true source depth. Thus we also looked at synthetic comparisons where we fixed the source depths to 0.2, 0.5, 1.5 and 3.0 km and for each depth the full suite of GF depths are tested. The results for both source types are shown in Figure 3.4. In this synthetic test the deviation from the true seismic moment is much greater due to errors from incorrect source depth, the percent change in total and isotropic moment decrease as the GF depths approach the correct value. For the four source depths we examined, the mean percent changes in moments are similar but the spreads are different. For example when source depth is at 1.5 km the change in isotropic moment away from the true source depth encompasses a much wider range compare to other tested source depths. The change in VR is most prominent at source depth of 3.0 km because a layer boundary exists at 2.5 km for all the velocity models.

3.5 HUMMING ALBATROSS

The synthetic tests show that although the loss of traction at the free surface can affect the method?s ability to resolve the moment at shallow depths, the impact on the recover-

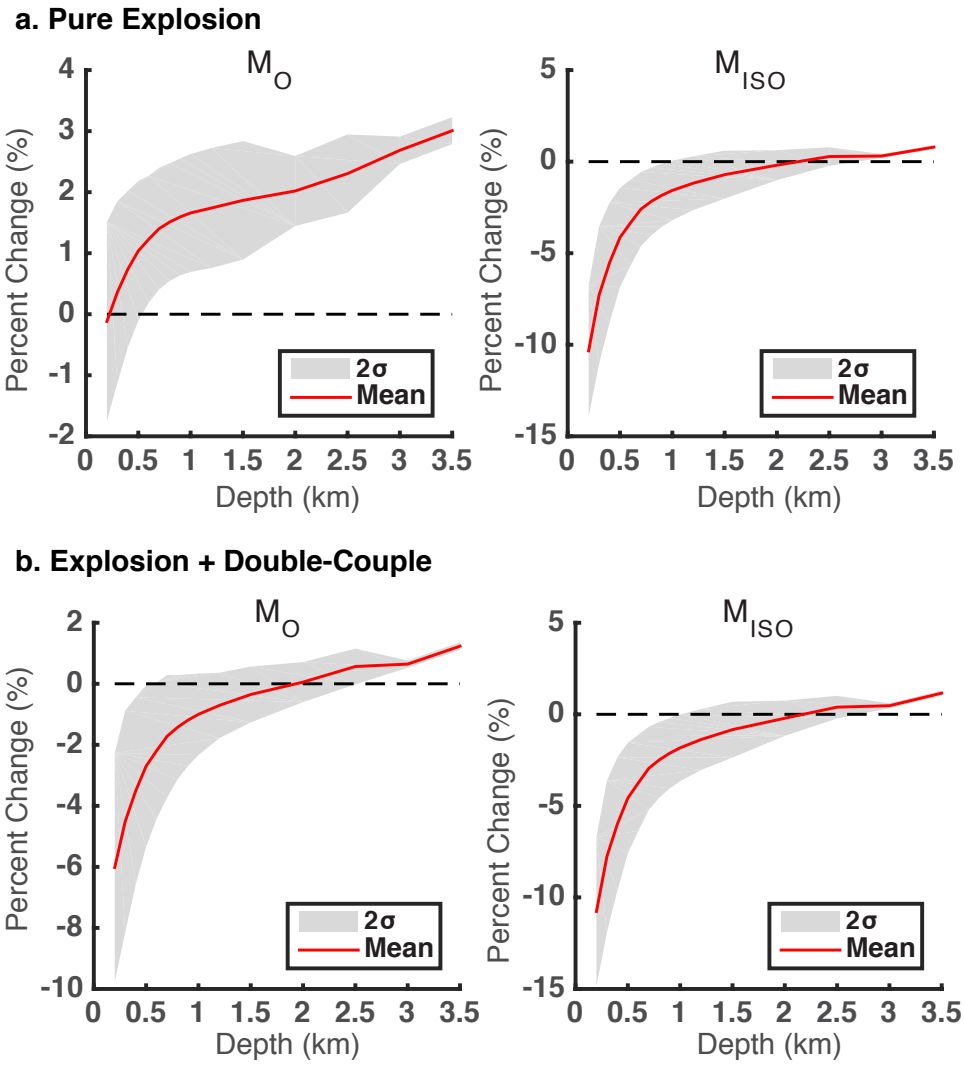

Figure 3.3: Percent change for (a) a pure explosion source and (b) a composite source, plotted as a function of source depth. The average value of all 59 models is the solid red line, the shaded region is 2σ from the mean, and the dashed line represents no deviation from the input seismic moments.

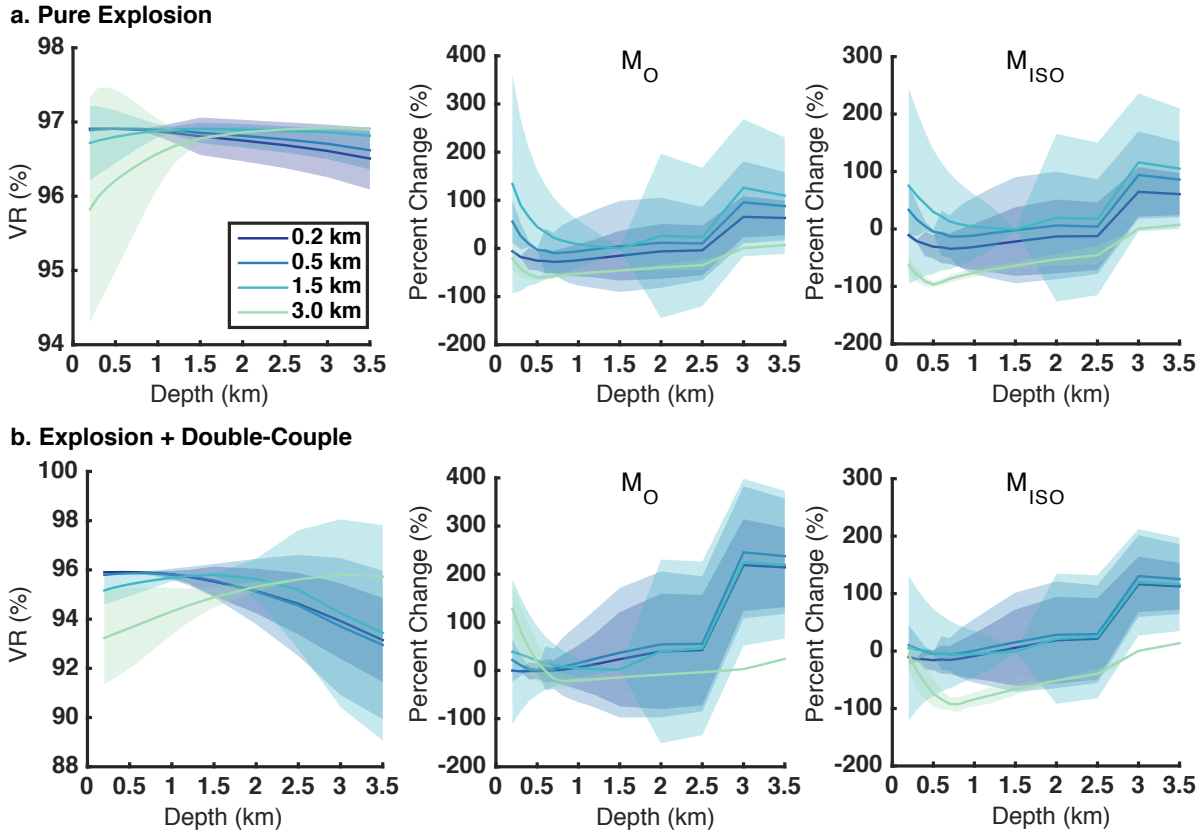

Figure 3.4: Source depth is fixed while we tested the full suite of Green's function depths (x-axis), and compare the VR, total moment percent change and isotropic moment percent change as a function of varying Green's function depth for (a) a pure explosion source and (b) a composite source. Similarly, the solid lines are the average values of all 59 models and the shaded regions are 2σ from the mean. The lines and shaded regions are color-coded according to source depths (data).

ability of the source mechanism is much less. To further evaluate the performance of the moment tensor method for shallowly buried sources we apply the method to data from the HUMMING ALBATROSS series. The data sets consist of twenty-six broadband, strong motion and short-period seismic recordings (Fig. 3.5). The chemical explosions are denoted at very shallow depths (< 20 m) and recorded at stations up to the several kilometers. We apply the moment tensor based discrimination method to three of the five chemical explosions, the two smallest events in the series have poor SNR below 3 Hz and we cannot estimate the source parameters with high confidence. Weston Geophysical Corp. provided the instrument corrected velocity and acceleration data for HUMMING ALBATROSS, and we prepare the velocity waveforms for source analysis by rotating the horizontal recordings to radial and transverse components, and bandpass-filtered the data and GFs with an acausal Butterworth filter. Depending on the instrument response and data quality the bandpass filter applied to each station ranges between 0.4 to 1.25 seconds. Table 3.1 lists the source depth and filter corners used, and the moment magnitude (M_W), M_{ISO} and waveform fits (VR) from time domain full moment tensor inversions.

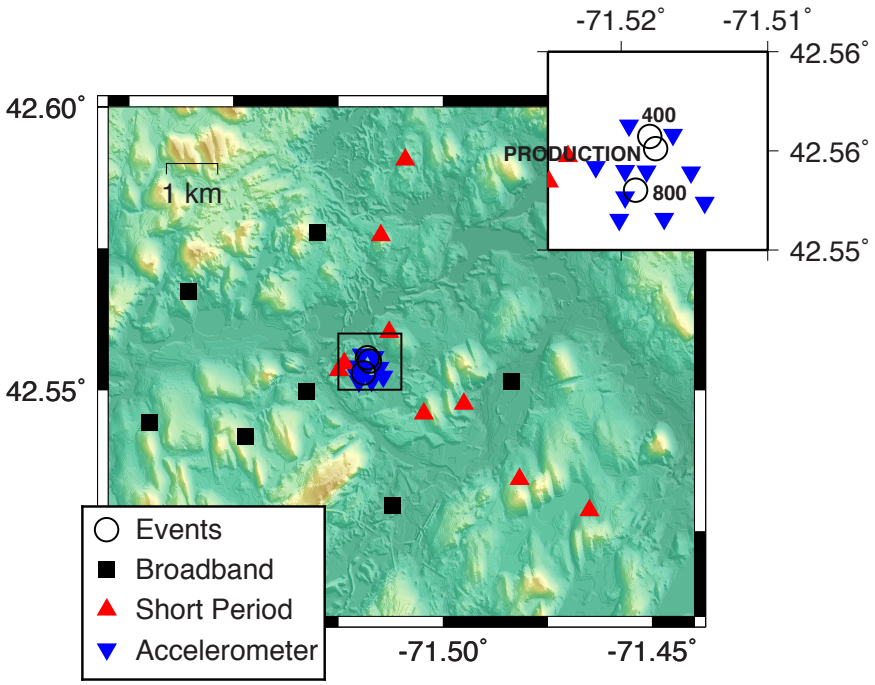

Figure 3.5: Event and station locations for the HUMMING ALBATROSS series. The seismic array includes broadband instruments (square), short period sensors (triangle) and accelerometers (inverted triangle). We looked at three of the five chemical explosions (circle) and the background colors represent the local topography where green is lower elevation.

Following the results of Ford et al. (2012) and Chiang et al. (2014) we utilize full waveform

data from broadband and/or short period stations for the time domain waveform inversion, and include both waveform and P-wave first motion polarities from all twenty-six stations into our source-type uncertainty analysis. We present results from the moment tensor sensitivity analysis both as a function of depth and frequency for the largest, delayed-fire production shot.

Table 3.1: Moment Tensor Solution and Yield

Event	Centroid Depth (m)	Filter (sec)	M_W	M_{ISO} (dyne-cm)	VR (%)	Estimated Yield (tons)	Design Yield (tons)
Production	Varied	0.5-1.25	2.5	$3.25\text{x}10^{19}$	70	29	9.22
800	9	0.5-0.83	1.9	$3.36\text{x}10^{18}$	72	3.0	0.357
400	11	0.4-1	1.4	$9.91\text{x}10^{17}$	64	0.9	0.182

The time-domain moment tensor inversion yields similar results for all three explosions in which the full moment tensor solutions all have relatively large isotropic components that are approximately between 40 to 50 percent of the total seismic moment, and the deviatoric inversions all result in vertical dip-slip-like mechanisms (Fig. 3.6). The deviatoric solutions are thus dominated by the M_{xz} and M_{yz} components, which as shown in Figure 3.1c, the TDS, RDS and ZDS GFs, show a marked reduction in amplitude with decreasing source depth. An example of the waveform fits and moment tensor solutions for the production shot is shown in Figure 3.7. All three explosions have strong shear wave energy in the transverse component, and many of those component have amplitudes comparable to Rayleigh waves on the vertical component. We avoid using stations in the direction of the free face (quarry cliff) for the production shot because of spallation at the cliff face. For shot 800 we tried a combination of stations with and without those in the direction of the free face and found the moment tensor solutions to be very similar.

The production shot source parameter uncertainties using only seismic waveforms show the best-fitting mechanisms are mostly isotropic (Fig. 3.8a). The source parameters are well constrained for solutions with VRs equal and above 95% of the maximum VR, but if we relax the threshold down to 90% of the maximum VR the population of well-fitted solutions extends across the DC/deviatoric line. Previous NSS studies of nuclear explosions have shown tradeoffs between ISO (+V) and −CLVD mechanisms, but generally not between ISO and DC mechanisms (Ford et al., 2012; Chiang et al., 2014). A combination of strong Love waves and free-surface effects most likely contributed to this apparent ISO-DC tradeoff and it is especially pronounced for the two smaller shots. To increase the confidence in our moment

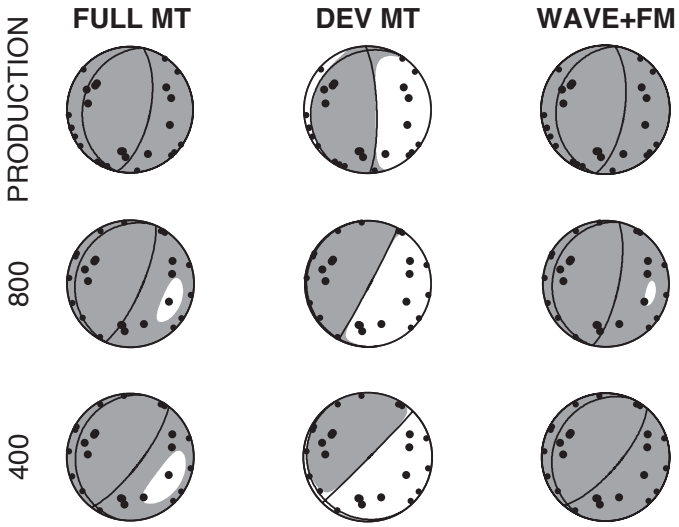

Figure 3.6: Tme domain full and deviatoric inversion and the best solution from combined waveform and P-wave first motion (filled circle) Network Sensitivity Solutions. All polarities are up.

tensor solutions we bring in constraints from P-wave first motion polarities. We have excellent azimuthal coverage for the first motion observations that sampled the entire focal sphere, significantly reducing the NSS to a predominantly explosive mechanism (Fig. 3.8b). The best solutions from the combined NSS are similar to the solutions from the waveform-only inversions (Fig. 3.6) Moment tensor solutions that deviate away from a theoretical opening crack do not fit the observed polarities. NSSs for shots 800 and 400 show similar behaviors, namely the ISO-DC tradeoff using only waveforms, and a well-constrained solution when combining both waveform (dominated by surface waves) and P-wave first motion polarities. We also present an example of a first motion only NSS (Fig. 3.8c), the maximum fit surface using only polarity data is extensive, therefore first motions only are not sufficient for event source-type discrimination.

Given the frequency band and source-receiver distance, the moment tensor inversion is not very sensitive to source depths shallower than ∼100 m. We estimate source depth sensitivity by looking at the VR as a function of source depth and observe that the deviatoric VR drops sharply starting around 100 m, whereas the full VR shows a more gradual decrease in VR. If we have no prior knowledge on source depth, the sensitivity analysis shows we can constrain the depth to be shallower than ∼100 m, indicative of possible manmade seismicity since natural earthquakes rarely occur at these depths. Although we do not have much sensitivity at the very shallow depths, the mechanisms remain stable and predominantly explosive at the borehole depths (Fig. 3.9a-b). We start to see a tradeoff between the mechanism and incorrect source depth at around 100 m for the production shot, and around 50 m for 800

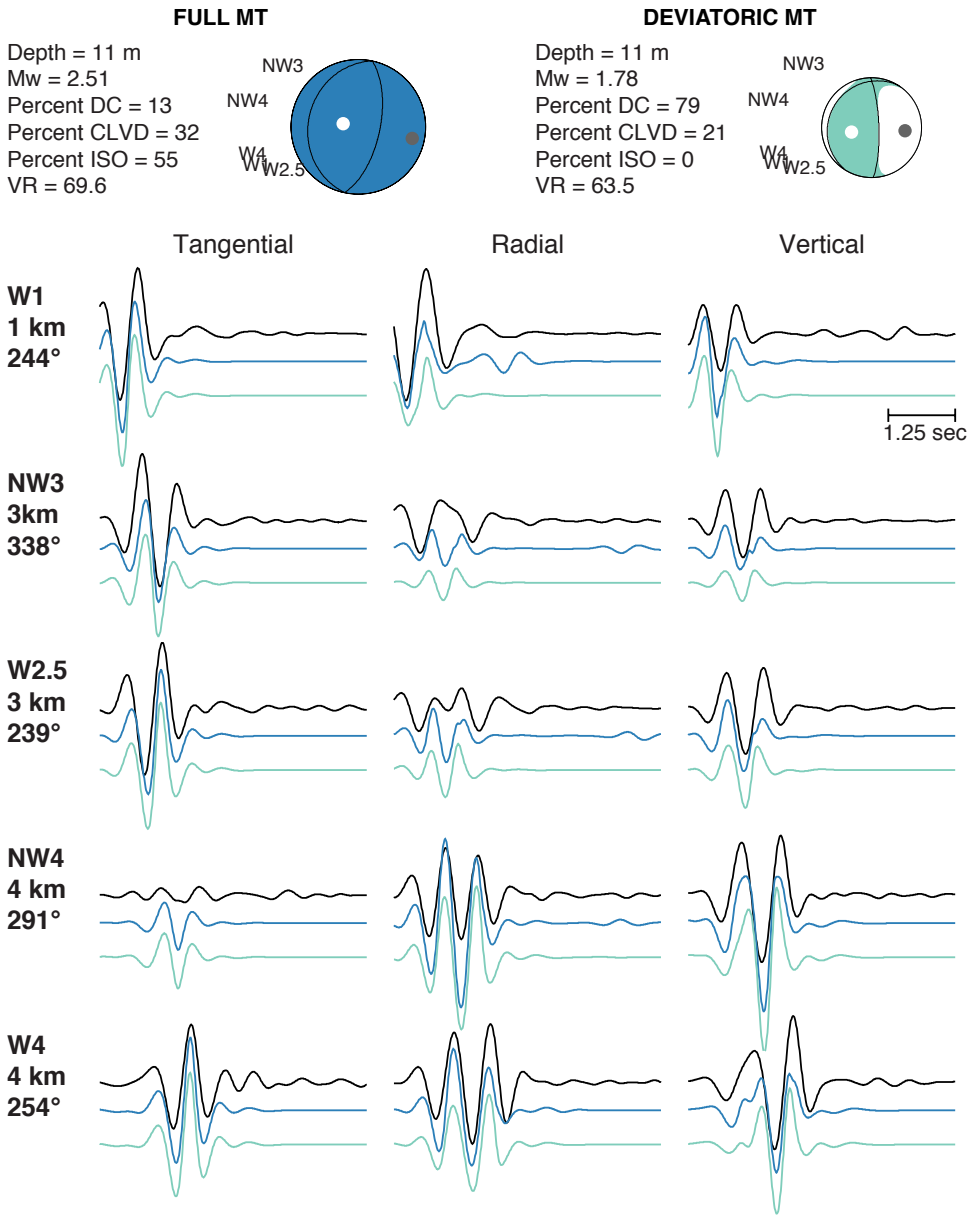

Figure 3.7: Focal mechanisms and waveform fits from full and deviatoric moment tensor inversions.

and 400; however the combined waveform and first motion inversion eliminates this tradeoff. Because we know the depth of the borehole where the explosions are detonated, we focus on the behavior of seismic moment at depths less than and equal to 20 m. Due to free surface effects the total and isotropic moment increases as source depth decreases (Fig. 3.9c-d), and the increases in seismic moments are controlled by changes in the M_{zz} and M_{yz} components (Fig. 3.9d), components that we anticipated to be strongly influenced by the free surface. The behavior of the moment tensor solution as a function of depth is similar for shots 800 and 400, although the free surface effects are more pronounced at the shallowest depths, where the full moment tensor solutions become vertical dip-slip due to a greater increase in moment from the M_{yz} component.

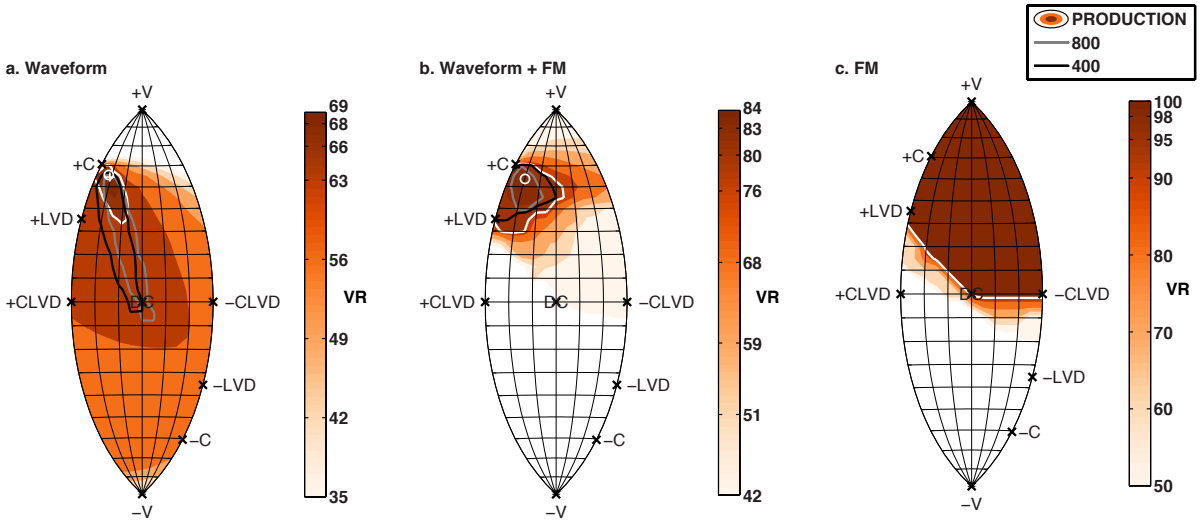

Figure 3.8: (a) waveforms, (b) waveform and first motions, and c) first motions. Best MT solutions from time-domain inversion (plus) and NSS (circle) are plotted in (a) and (b). Production shot NSS are plotted as shaded contours, and the white, gray and black contours are populations of solutions with normalized VR $\geq$ 95% relative to the maximum for the Production, 800 and 400, respectively.

The Earth becomes very heterogeneous at high frequencies where the smoothed 1D model is no longer adequate in characterizing the complexities in high frequency wave propagation between the source and receiver. Therefore the reason for utilizing low frequency waveform data is to minimize the bias from unaccounted velocity structures. However, the challenge for moment tensor inversion at these very shallow depths for the HUMMING ALBATROSS data is that the free surface effect not only increases with decreasing source depth but also at longer periods. The production shot has relatively good SNR at periods up to 2.5 seconds, but if we fix the source depth to 11 m and look at the free surface effects on the inversion as

a function of filter passband we see the solutions become vertical dip-slip at longer periods (Fig. 3.10a-b). The total moment increases (Fig. 3.10c) as we go towards longer periods due to rapidly increasing contributions from the M_{xz} and M_{yz} components (Fig. 3.10d). Hence finding the optimal filter passband that minimizes both the effects of the velocity structure at high frequencies, and the free surface at low frequencies is especially important and potentially challenging for moment tensor analysis of shallow sources. However, it is important to note again that by combining the first-motions with the waveforms this issue is eliminated or at least surppressed.

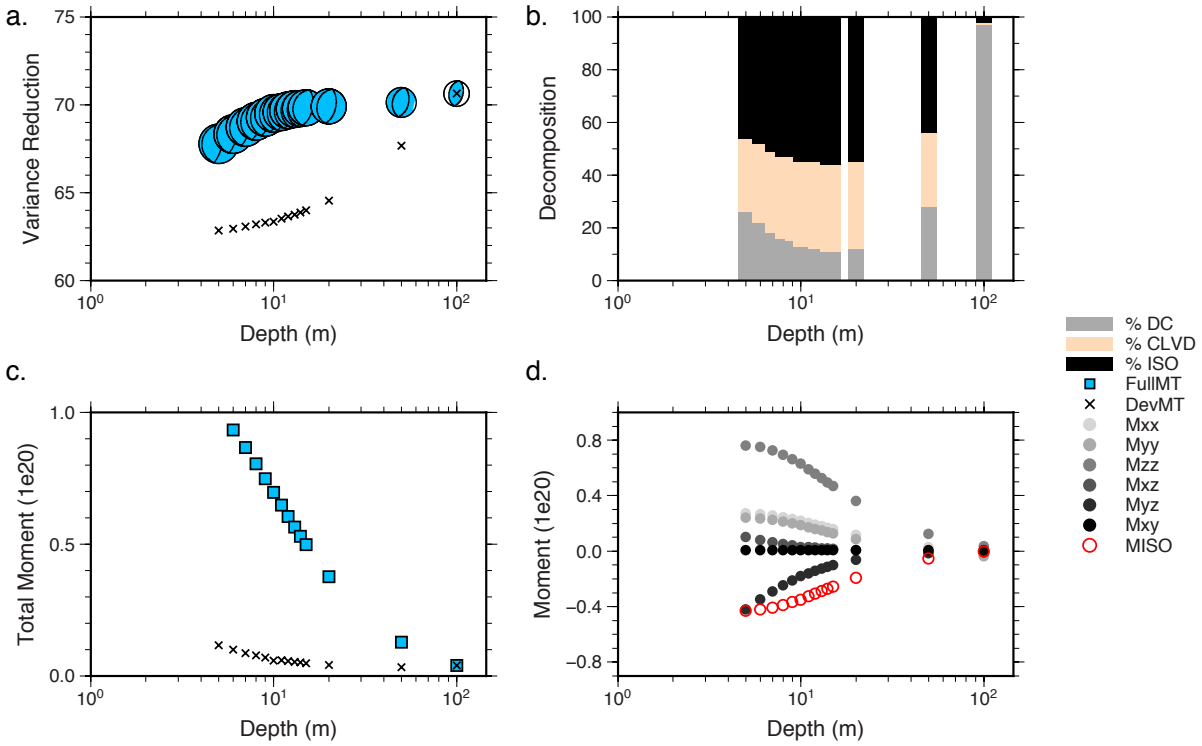

Figure 3.9: Production shot moment tensor solutions as a function source depth, using only waveform data. (a) VR from full moment tensor inversion (focal mechanism) and deviatoric moment tensor inversion (cross), (b) full moment tensor decomposition. Shaded bars are the percent DC, CLVD and ISO components, (c) total moment from full inversion (square) and deviatoric inversion (cross), and (d) moment tensor elements (filled circles) and isotropic moment (open circle).

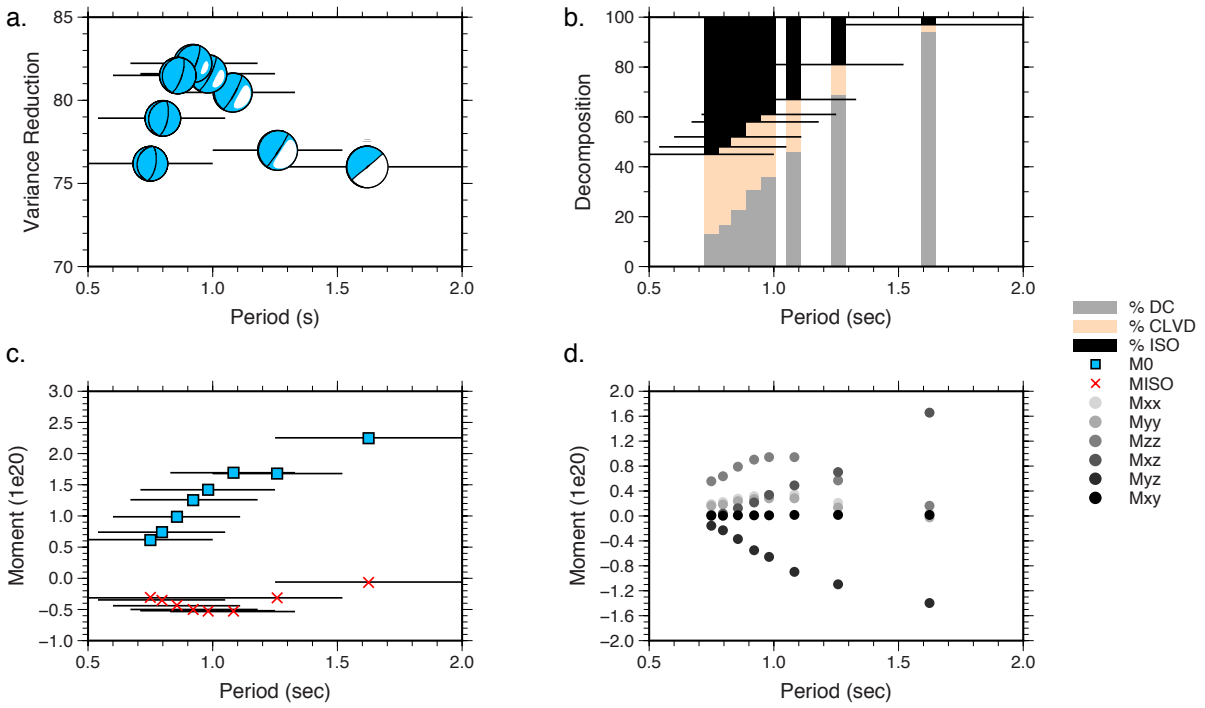

Figure 3.10: Production shot full moment tensor solutions as a function of filter passband, using only waveform data. (a) VR and focal mechanism), (b) decomposition, (c) total moment (square) and isotropic moment (cross), and (d) moment tensor elements (filled circle). Horizontal lines in (a)-(c) specify the filter passband used for each inversion at 11 m depth.

3.6 Yield Estimates

Empirically the magnitude-yield relationship can be described by the following equation:

$$M = A \log_{10} Y + C, \tag{3.7}$$

where M is the seismic magnitude, Y is the yield in kilotons and A and C are constants that depend on the magnitude measurement used. C may also include additional corrections to account for differences in source medium that are independent of the yield. Empirical relationships to estimate yield have been developed using body wave magnitudes (mb) and surface wave magnitudes [Ms] (Mueller and Murphy, 1971; Murphy, 1977; Burger et al., 1987; Murphy, 1996, e.g.) from past nuclear explosions with known yields. Given and Mellman (1986) and Ekström and Richards (1994) performed moment tensor inversions on the Shagan River explosions from the former Soviet Union and explosions from the U.S. Nevada Test Site (NTS), and computed the moment-yield relationships for those event. Yield estimation using the M_{ISO} from moment tensor inversions can be challenging due to difficulties

assessing the contributions from the isotropic and the non-isotropic radiation of the source as discussed in Stevens and Murphy (2001), as well as due to free surface effects at shallow depths. However as demonstrated in Ford et al. (2012) and Chiang et al. (2014) and the previous sections of this paper, source-type analysis (NSS), and the combination of waveform and first motion data can help to better constrain the isotropic radiation of the moment tensor.

We calculated the yields for HUMMING ALBATROSS using the waveform moment tensor results at the reported centroid depths, and the M_{ISO}-yield relationship $M_{ISO} = \log_{10} Y + 14.05$ from Stevens and Murphy (2001). The empirical relationship is derived from previously published moment tensor inversion results, and announced yields or estimated yields from Shagan and NTS explosions (Fig. 3.11a). To use Stevens and Murphy (2001)'s empirical relationship we extrapolate the curve down to very low values of yield and isotropic moment. Because the empirical relationship is derived from nuclear explosions, differences in the seismic coupling efficacy between nuclear and chemical explosions (Murphy, 1996) can also bias our yield estimates. We present our yield estimates and the design yields in Table 3.1. The moment tensor inversion at shallow depth overestimates the yields for all three explosions; the estimated values are 2.8 times, 7.6 times and 4.4 times greater than the true yield for the production shot, 800, and 400, respectively. However, from our combined NSS analysis, we can estimate the errors associated with our moment tensor solutions. We choose a population of moment tensor solutions with normalized VRs $\geq 90\%$ and computed the mean and 2σ from the mean. For the Production shot, the mean is very close to the Stevens and Murphy (2001) scaling, and for the two smaller shots the lower error bounds overlaps with the empirical scaling.

From our synthetic studies on the effects of the free surface at regional distances, we observe the recovered mechanism is less sensitive to the source depth, but there can be bias in the moment due to the loss of traction at the surface. Although the deviations from the true moment are all within 20% from our synthetic tests, the amount of deviation also depends on station coverage, frequency passband and station quality. Additional synthetic tests on varying the station coverage, frequency passband and SNR suggest that although the amount of bias in M_{ISO} varies, the asymptotic behavior as a function of depth remains similar, and that the recovered M_{ISO} approaches the true value as the source depth increases. Thus in order to minimize the vanishing traction effects, it may be possible to invert for the source parameters at a deeper depth where the synthetic tests show the M_{ISO} approaches the true value. Here we investigate the possibility to recover the correct yield by intentionally inverting for the source at a deeper depth.

We first perform similar synthetic tests for a pure explosion scenario using the production shot station configuration, filter passband and 1D velocity model to predict the depth range in which we can minimize both the effects from vanishing traction and incorrect source depth. We fix the depth of the data but vary the depth of the GFs (as what is done in practice

when source depth is unknown or has large uncertainties), and found that the moment tensor inversion is able to recover the correct focal mechanism and seismic moment at depths between 0.02 and 0.05 km. This is an idealized case with no time shift in the inversion, high SNR and prefect knowledge of the Earth structure, the question remains whether this adjustment in the source depth can correctly estimate the yield from real explosions where we have imperfect knowledge of the Earth structure.

In Figure 3.11b the yield estimates for HUMMING ALBATORSS as a function of source depth are compared. In general because M_{ISO} decreases as source depth increases, the estimated yield also decreases. Yields computed from M_{ISO} obtained at 0.02 and 0.05 km depth do agree with the true yield, but as noted previously we start to see tradeoff between incorrect source depth and source mechanism around 50 to 100 km where the moment tensors are no longer predominately explosive using only waveform data. Unlike the synthetic case, with real data when we introduce additional errors from incorrect source depth can have a greater impact on the recoverability of the mechanism, particularly for the smaller shots 800 and 400 where we use higher frequency waveforms.

3.7 Discussion

Synthetic moment tensor inversion tests show that although the loss of traction at the free surface affects the moment tensor inversion?s ability to resolve the seismic moment at shallow depths, the impact on the recoverability of the source-type (explosion, double-couple, composite mechanism) is substantially less. This is illustrated by the successful discrimination of the NTS, DPRK, Soviet JVE, Chinese Lop Nor and HUMMING ALBATROSS events as explosions. However, the degree in which free-surface vanishing traction affects the seismic moment depends not only on the station geometry, noise levels and filter passband but also on the velocity model. Free surface effects are more pronounced when modeling longer wavelengths.

Non-isotropic radiation in the HUMMING ALBATROSS moment tensor solution results from a combination of both the free-surface effects and the strong SH waves. SH and Love wave generation from chemical explosions is not an uncommon observation, and a number of studies on quarry blasts suggest that the non-isotropic radiation results from spall of material from the quarry face (Goforth and Bonner, 1995; Bonner et al., 1996), and the interaction of the wavefield with the severe topographic features of quarry benches (Barker et al., 1993). McLaughlin et al. (2004) modeled observed short period Love and Rayleigh waves from a Texas quarry and found that the horizontal throw of material from the free face (spall model) is the dominant mechanism. Our moment tensor analysis does not take into account the horizontal single-force component due to spall, the collapse of the quarry cliff face, and for the production shot, the temporal and spatial spread from the delay-firing

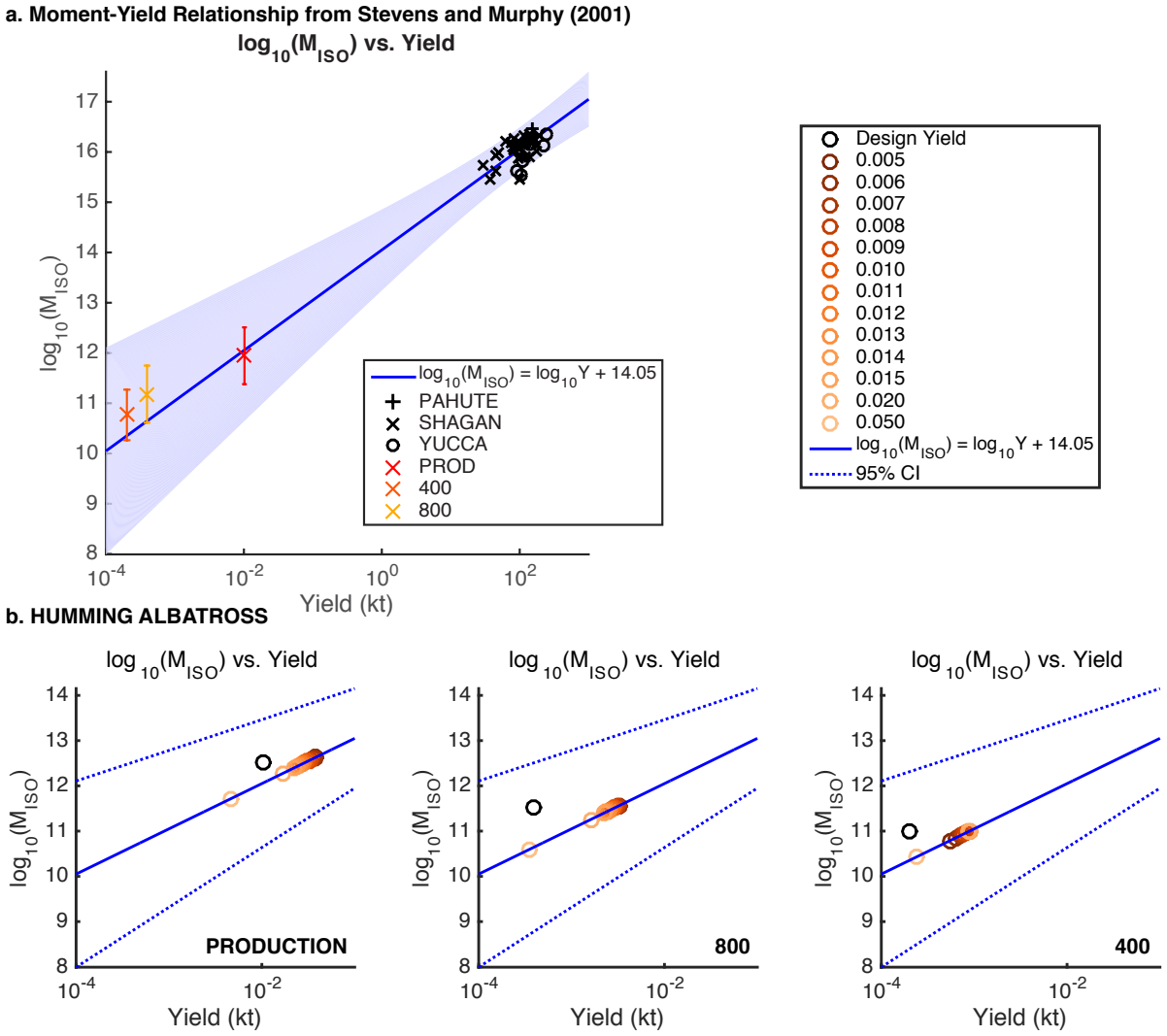

Figure 3.11: (a) Isotropic moment vs. yield from nuclear explosions listed in Stevens and Murphy (2001) and HUMMING ALBATROSS chemical explosions. Blue line is the moment-yield scaling relations from Stevens and Murphy (2001). The shaded regions are the 95% confidence bounds. The mean isotropic moment and error bars (2σ) for the three HUMMING ALBATROSS events are computed from a population of moment tensors with normalized VRs $\geq 90\%$ in the combined NSS, as shown in Figure 3.8b. (b) Isotropic moment vs. yield for HUMMING ALBATROSS at various depths. The yields are computed using the empirical scaling relation by Stevens and Murphy (2001), and the isotropic moment (at the reported centroid depth) from waveform moment tensor inversion vs. the true yield is also plotted.

scheme. These complications contribute to the difficulty in obtaining unique source-type identification using long-period waveforms only (Figure 3.8a). The non-isotropic component of the inversion results is manifested as a reverse mechanism with either a near-vertical or near-horizontal dipping layer, and a vertical dip-slip mechanism in the deviatoric solution. Because the high frequency P waves may be more sensitive to radiated energy from the initial rupture (Pearce and Rogers, 1989; Guilhem et al., 2014), including P-wave first motion polarities are particularly useful to constrain the isotropic component of explosive events where the first arrivals come from the detonated explosion. As illustrated in Figure 3.8, the added constraints from first motion observations greatly reduces the ambiguity in source mechanism from waveforms and results in a unique identification of the events as having substantial volumetric components consistent with explosions.

Moment tensor based event discrimination for shallow sources is reliable when SNR is high, especially with the combination of data from waveforms and first motions. When we include errors in the isotropic moment estimated from the NSS analysis, we see although there is still a bias towards larger moment (events 800 and 400) even at such low yields and low magnitudes, the isotropic moments intersect with the empirical scaling relation. Although source inversions at greater depth reduce the effects of vanishing traction, in cases of extreme free-surface effects and complexities in the source such as the chemical explosions from this study, added errors from incorrect source depth can impact event discrimination. Incorrect source depth can result in biases up to a factor of 2 in the total seismic moment and isotropic moment based on the average values in our synthetic study (Fig. 3.4). Two other factors that are difficult to quantify can also contribute to the difference in our estimated yield and the design yield, one is the nature of the explosive and also the frequency content of the waveforms used to derive the magnitude-yield scaling law. The Stevens and Murphy, 2001 scaling law is derived from modeling large nuclear explosions at relatively long periods (17-60 seconds; Given and Mellman, 1986). For the same yield, nuclear explosions, single-fired buried chemical explosions, and ripple-fired quarry blasts exhibit differences in radiated seismic energy (Murphy, 1996).), therefore additional scaling is required to factor in the differences in seismic coupling for different types of explosions. All three shots are partially confined but the production shot uses a ripple-firing scheme and the two smaller shots are single-fired chemical explosions. Traditionally single-fired shots are designed to maximize the strength of the seismic signal (Khalturin et al., 1998). In addition, possible site effect due to the use of higher frequency waveforms from temporary surface sensors may also contribute to the overestimation of the yield.

3.8 Conclusion

Theoretical vertical dip-slip GFs associated with the M_{xz} and M_{yz} components have vanishing amplitudes at shallow depths (< 1 km) due to the loss of traction at the free surface,

while the GF waveforms look similar with little phase distortion. However synthetic calculations at shallow depths show moment tensor based event discrimination is reliable and the resolvability of the moment tensor solution depends on station configuration, noise level, the frequency band and the velocity model.

We are able to recover a predominantly explosive source mechanism for the three HUMMING ALBATROSS chemical explosions from moment tensor inversions. Although the source-type uncertainty analysis shows that we cannot uniquely characterize the events as predominantly explosive using only waveform data, the combined waveform and first motion method enables the unique discrimination of these events. This method has been applied in previous studies which have shown the inclusion of P-wave first motions in addition to full waveform data eliminates the common ISO-CLVD tradeoff (Ford et al., 2012; Chiang et al., 2014) and reduces the uncertainties of sparsely recorded underground explosions with strong Love waves and reversed Rayleigh waves (Chiang et al., 2014). In this study we further demonstrate that incorporating the two data sets is particularly useful in constraining the isotropic component of explosions, and the method not only applies to large events, but also small magnitude, very shallow explosions that are effectively at the free surface. The combination of both low frequency full waveform data and high frequency P-wave polarities greatly enhances the capabilities of the moment tensor source-type discrimination method in cases of sparse station coverage, strong Love waves and free-surface effects.

The moment tensor method is capable of event discrimination, although yield estimation using the recovered absolute seismic moment from moment tensor inversion remains challenging and can have large uncertainties, we can begin to put error bounds on our moment estimates, and therefore yield, using the NSS technique and combining waveform and first motion. Pure explosion synthetic tests suggest source inversions at deeper depths reduce the free surface effects on the moment, but we cannot draw definite conclusions using the results from the HUMMING ALBATROSS data set due to not only free-surface effects, but uncertainties associated with imperfect knowledge of the Earth structure, unaccounted non-isotropic radiation due to the mass movement of the quarry face and differences in seismic coupling between different types of explosions. In addition, the moment-yield relationship derived from larger nuclear explosions may not be adequate for such low magnitude chemical explosions.

Chapter 4

Sensitivity of Seismic Moment Tensors to 3D Velocity Structure: A Synthetic Study

4.1 Abstract

The estimation of seismic source parameters is dependent upon having a well-calibrated velocity model to compute the Green's functions for the inverse problem. Ideally, seismic velocity models are calibrated through broadband waveform modeling (e.g. Dreger and Helmberger, 1990; Bhattacharyya et al., 1999), however in regions of low seismicity, velocity models derived from body or surface wave tomography may be employed. For purposes of broadband strong motion simulation regional 3D velocity models have been constructed (e.g. Rodgers et al., 2008; Kim et al., 2010; Aagaard et al., 2010). Whether a velocity model is 1D or 3D, based on broadband seismic waveform modeling or the various tomographic techniques the uncertainty in the velocity model can be the greatest source of error in moment tensor inversion. These errors have not been fully investigated for the nuclear discrimination problem. This study focuses on the effects of the 1D model assumption on moment tensor inversion through a synthetic sensitivity study, where we produce synthetic 3D velocity model seismogram data and invert them using 1D velocity models. The effect of 1D model assumption can then be interpreted via the difference between input and inverted moment tensor solutions.

4.2 Introduction

We have established in the previous two chapters that the regional seismic moment tensor (MT) method is a robust and reliable technique to identify different seismic source types under sparse monitoring situations, at shallow source depths, and when the complexities in

isotropic source processes are often not well understood (e.g. Massé, 1981). For this study we will explore possible biases associated with one of the most fundamental assumptions in seismic source analysis, which is the assumption that a 1D velocity model is a good approximation to real Earth structure.

The ground motion (u) recorded at the receiver is a linear combination of the source (seismic moment tensor, $\mathbf{M}$) and the Green's tensor ($\mathbf{G}$), where $\mathrm{u} = \mathbf{GM}$. The Green's tensor represents the impulse response of the medium, describing the seismic wave propagation between the source and receiver for a reference Earth model. Basic source types are typically comprised of fundamental fault representations (e.g. Jost and Herrmann, 1989), but they can also be fundamental single-couples and vector dipoles. In previous studies (e.g. Ford et al., 2009b; Walter et al., 2009; Nayak and Dreger, 2014; Chiang et al., 2014) simple but well-calibrated 1D velocity models have been used to compute the Green's function and invert for the MT. This assumption is valid at relatively long periods where the wavelengths being inverted are much larger than the spatial dimension of the sources, and the source time history is short compared to the frequency passband of the inversion. However the limits of the definitions are not very well defined, nor are they thoroughly explored in the published literature.

The approach to compute Green's functions, especially in regions of low-seismicity where high-resolution velocity models are not available, is through waveform modeling of regional earthquakes to produce calibrated 1D velocity models (e.g. Dreger and Helmberger, 1990; Bhattacharyya et al., 1999; Baise et al., 2003; Kim et al., 2011). However, the 1D velocity model assumption can be the greatest source of error in the MT solution and has never been thoroughly investigated for the source-type discrimination application. In Ford (2008), the sensitivity of full MT solutions for the 2009 Memorial Day DPRK nuclear explosion to 1D velocity structure was examined. In that study 880 1D velocity models for the region from the North Korean test site to regional distance broadband stations, derived from the Monte Carlo Markov Chain inversion results (Pasyanos et al., 2006), were tested to investigate the effect on the recovery of the seismic MT source type (e.g. Hudson et al., 1989; Ford et al., 2010). The results indicated that while there was a strong effect on the source-type and the ability of the Green's functions for the individual velocity models to fit the data, overall the velocity model uncertainty was not large enough to affect the discrimination of the seismic event as an explosion. The spread of the derived solutions in source-type space (e.g. Hudson et al., 1989) in that study does illustrate however that the effect needs to be examined further, particularly for cases where precise source-type determination is important, and for very sparse monitoring conditions where the range of acceptable solutions in terms of the ability to fit the data can become large due to poor station coverage. From our study of explosions in Eastern Kazakhstan and Lop Nor (Chapter 2; Chiang et al., 2014) we also observe similar variations in waveform fits, moment and MT derived source-types as a function of velocity model. Thus, a comprehensive understanding of the uncertainties associated with the assumed 1D velocity structure is crucial in being able to apply the MT based discrimination method to new regions of interest in order to fully assess populations

of MT results for explosions, collapses, earthquakes, geothermal and volcanic events.

There are some studies that have examined errors in regional MT inversions due to biases from velocity models. Wei et al. (2012) shift the theoretical seismograms used in their 1D Green's functions according to a 2D correction surface. Comparison with and without the time shift shows the solution improved when the authors incorporated the correction. This is similar to what Ford (2008) found in which when time shifts were employed the spread of MT solutions for different 1D velocity model Green's functions in source type space was reduced. In the Berkeley MT code (Dreger, 2003; Minson and Dreger, 2008) a time shift is applied for optimal alignment of the data with the applied Green's function which takes into account, to a degree, the discrepancy between the velocity model and the actual Earth structure (Pasyanos et al., 1996). Šílený (2004) has investigated the sensitivity of full regional MT inversion for an M_W4.8 earthquake in Italy to perturbed 1D velocity models and found that the DC mechanism is well-resolved from 10 to 50 second but not from 5 to 10 seconds. Liu et al. (2004) obtain MTs for three earthquakes in Southern California with a regional 3D model using the spectral element method and compare the 3D solutions with those obtained from body wave and surface wave inversions, and found that the solutions agree well. Covellone and Savage (2012) calculated 3D Green's functions for earthquakes in the Middle East and show improved waveform fits and a reduction of non-double-couple (non-DC) components. Panning et al. (2001) included near source 3D velocity heterogeneity and found its effect to be minimal in the bandwidth of interest, although small isotropic components ($\sim$10% of the total scalar moment) could arise due to the unmodeled near-source 3D structure. Although there have been studies on the effects of 3D structure on source inversions (e.g. Panning et al., 2001), to our knowledge, there has not been much work investigating the effect of 3D heterogeneity along the full source-receiver path on the full regional MT for earthquakes aside from the Covellone and Savage (2012) work. For non-DC sources, Tkalčić et al. (2009) determined the source parameters of a volcanic earthquake using data from 20 to 50 seconds and path-specific 1D velocity models to account for 3D heterogeneity. This work offers the first systematic investigation of potential bias due to unaccounted 3D structure on regional MT inversion.

As a result of the unprecedented coverage of the NSF EarthScope transportable array (TA), a number of high-resolution regional 3D Earth models have been published in the literature (Bensen et al., 2009; Moschetti et al., 2010; Porritt et al., 2014; Shen et al., 2013). The availability of these finer resolution regional tomography models, particularly the ambient noise surface wave models allow us to generate synthetic waveforms in the frequency range relevant for regional waveform modeling of small to moderately-large events. Previous work by Ford et al. (2009a) studied a variety of events in the western U.S. with the majority of events near or at the Nevada Test Site (NTS). These events included nuclear and chemical explosions, earthquakes and mine and nuclear cavity collapses. For these events we study the impact of the 1D velocity model assumption on moment tensor results be means of a series of synthetic studies. In the synthetic studies we compute 3D velocity model GFs using the

anelastic finite-difference (FD) code, Seismic Waves, 4^{th} order (SW4), developed at the Center of Applied Scientific Computing at Lawrence Livermore National Laboratory (Sjögreen and Petersson, 2012; Petersson and Sjögreen, 2014). We use the Moschetti et al. (2010) tomographic model for the western U.S. and station geometries from Ford et al. (2009a). We then invert these 3D synthetic data using GFs for a 1D model to determine the seismic MT and compare the results to the known input moment MT. The effects of the 1D velocity model assumption can then be interpreted via the difference between input and inverted solutions.

4.3 Velocity Model and Computation Set Up

The synthetic experiment is set up to evaluate the effects of 3D heterogeneity along the source-receiver path. We simulate three-component velocity records using the Moschetti et al. (2010) 3D Earth model and the FD code SW4, and perform the standard MT analysis using Green's functions computed from a well-calibrated 1D Earth model for the Western U.S. (Song et al., 1996). The Moschetti et al. (2010) model spans the entire western U.S. and is constructed based on surface wave dispersion measurements from teleseismic earthquakes and regional-scale ambient noise measurements; the combination of data and dense station coverage better constrains the shear wave velocity structure in the crust and uppermost mantle than previous, earthquake only tomographic models. Moschetti et al. (2010) invert for both isotropic and anisotropic models but in this study we only consider the isotropic model. The 3D velocity model consists of a low velocity sediment layer and three crystalline crustal layers above the Moho, and a smoothly varying upper mantle below the Moho. The compressional wave velocity to shear wave velocity (Vp/Vs) ratio and density structure of the inverted 3D model are based on empirical relations between wave speed and density (Brocher, 2005). Focusing on California and Nevada (Fig. 4.1), the California Coast Ranges have slow wave speeds in the upper and middle crust, and beneath the Central Valley of California the low wave speeds are associated with thick sediments in the San Joaquin Basin to the south and the Sacramento Basin in the north. In the Central Valley and southernmost end of Sierra Nevada the Moho varies between 20 to 40 km, and the crust thickens near the eastern edge the Sierra Nevada. Moschetti et al. (2010) contribute the low velocity anomalies of the lower crust beneath eastern California, the Basin and Range and the High Lava Plains to conductive heating. The Basin and Range in northern Nevada have relatively uniform crustal and mantle structure, as the relatively long-period surface waves used to construct the model are not sensitive to large impedance contrasts from very thin layers.

For our FD simulation we did not include any water layers. We account for attenuation Q using a function of local Vs [km/s] (e.g. Graves et al., 2008; Olsen et al., 2009), such that Qs = 50Vs and Qp = Qs. The FD code SW4 solves the seismic wave equation in a displacement formulation using a summation-by-parts principle and it is fourth-order accurate in space and time (Sjögreen and Petersson, 2012; Petersson and Sjögreen, 2014).

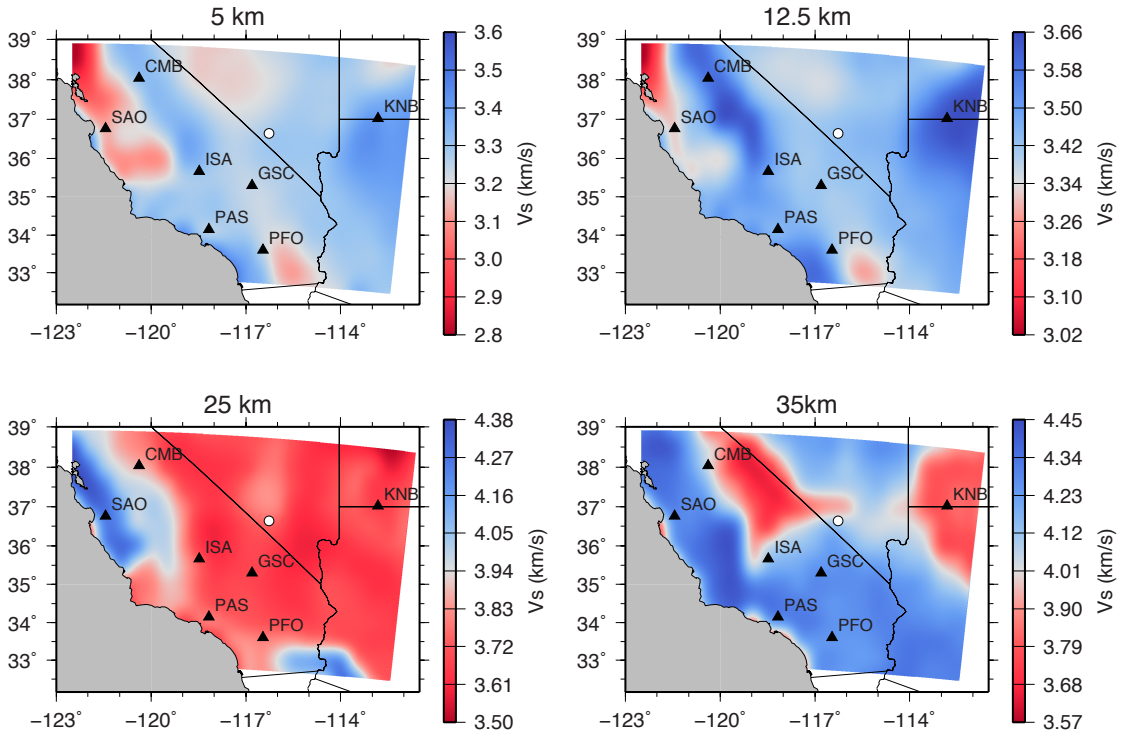

Figure 4.1: Background color represents the shear wave velocity (Vs) from Moschetti et al. (2010) at various crustal depths, white circle is the event location, and black triangles are the station locations.

The code utilizes a Cartesian mesh to solve for the seismic wave equations and the mesh can be built using the PROJ.4 cartographic projections library (Developed by G. Evenden, https://trac.osgeo.org/proj/) to ensure accurate mapping between geographic and Cartesian coordinates. In contrast to a staggered grid finite difference scheme (e.g. Larsen and Shultz, 1995), SW4 uses a node-centered formulation to reduce computation memory. The computation domain consists of a free-surface boundary at the top with the option for irregular topography (Appelo and Petersson, 2009), and absorbing super-grid boundaries in the far field to minimize boundary reflections from the side and the bottom of the computation domain. We performed the calculations on the Livermore Computing Center (LC) 8-core Xeon 35-2670 Linux cluster, cab, consisting of 1,296 nodes, each with 16 cores per node and 32 GB memory. The velocity model is discretized on a Cartesian grid with 500 m grid spacing and a minimum Vs of 1.1 km/sec. SW4 internally resamples the coarser 3D tomographic model (0.5 degree grid spacing) on to the finer computation grid via 2-steps: (1) linear interpolation in the vertical direction and (2) Gaussian averaging in the horizontal directions. The model domain extends approximately 665 km x 950 km x 70 km, and we apply a Dirac delta forcing function at the source to simulate a seismic source in our FD

calculations. To avoid numerical artifacts due to grid dispersion we consider 10 grid points per minimum wavelength, and therefore the maximum resolvable frequency is 0.2 Hz for the given minimum Vs. Since we are inverting data between 0.01 to 0.1 Hz and given the magnitude range (M $<$ 5) of the events we are investigating it is not necessary to consider a source time history beyond the basic Dirac delta function.

Prior to performing the synthetic sensitivity tests, we performed benchmark testing to validate the wave propagation simulated using SW4. We generated and compared 1D velocity waveforms using the two different methods: (1) the frequency-wavenumber (FK) integration method (Wang and Herrmann, 1980; Herrmann and Wang, 1985; Zhu and Rivera, 2002) and (2) the numerical FD method (SW4). The FK code is included as part of a software package called Computer Programs in Seismology (CPS3.30) developed by Herrmann (2013) at St. Louis University. We use a simple three-layer model with no attenuation and computed the synthetics at 100 km distance for the fundamental Green's tensor force couples (Fig. 4.2). Both methods agree closely, where deviations are mostly due to small amplitude differences in the G_{XZ}, G_{YZ} and G_{ZZ} components.

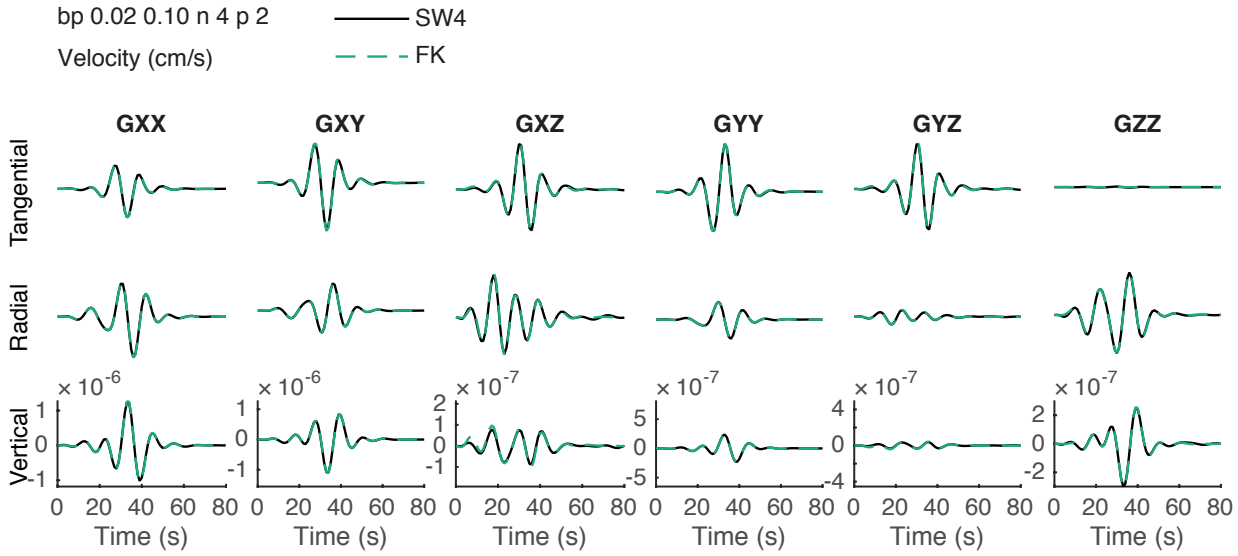

Figure 4.2: Waveform comparison between finite-difference (SW4, solid black line) and frequency wavenumber integration (FK, dashed line).

4.4 Sensitivity to 3D Velocity Structure

We set up the synthetic experiment to simulate the standard processing procedure used in regional MT analysis. The simulated 3D, three-component velocity records (north-south, east-west and up-down) from SW4 are treated as "data" in our synthetic test. For each station, we rotate the data to transverse, radial and vertical, and add random Gaussian white noise to the data by scaling the amplitude of the noise to 10% of the maximum amplitude of the three components. 1D Green's functions were calculated using the FK method Herrmann (2013). The 3D synthetic data and 1D Green's functions are both filtered between 10 to 50 seconds. Differences between the input and recovered MT reveals the bias due to 3D structure. A direct comparison of the 3D and 1D synthetics for a normal earthquake mechanism shows minor differences in the arrival times and waveforms, and almost no difference in the 20 to 50 second period range which is a commonly used passband in regional waveform source inversion Pasyanos et al. (1996). This is due to the large wavelengths in the 20 to 50 second passband and the smooth nature of the 3D tomographic model. Nevertheless, as regions of monitoring interest are calibrated the 3D models produced are likely to be with the same type of regional-scale surface wave approach used to construct the 3D tomographic model examined in this study. The following section describes the results for the three types of sources we have tested: (1) double-couple (earthquake), (2) isotropic (explosion) and (3) composite source mechanisms. We used the Little Skull Mountain mainshock station geometry of Ford et al. (2009a) for all of the synthetic sources in this experiment to reflect a real regional monitoring configuration.

4.4.1 Double-Couple Sources

First we examine the 1D model assumption for the double-couple (DC) sources. We tested two DC mechanisms: a normal earthquake and an oblique reverse event, both at 4.5 km depth. The normal faulting mechanism is taken from the Little Skull Mountain mainshock MT solution in Ford et al. (2009a). For the DC synthetics, both deviatoric and full MT inversions can recover the correct source mechanism (Fig. 4.3), and the variance reduction (VR), a measure of the goodness-of-fit between data and synthetics, are very similar for both inversion schemes. Although the full MT results have up to 16% ISO component in the full MT inversion (Fig. 4.3), the change in VR is not statistically significant as determined by an F-test (Menke, 1989; Templeton and Dreger, 2006; Menke, 2012), where the level of significance is only 57%. Similarly, the Network Sensitivity Solution [NSS] (Ford et al., 2010), a mapping of the goodness of fit parameter in the complete source-type space, shows an earthquake-like surface centered on the origin (pure DC). The CLVD components are 17% and 40% for the normal and oblique mechanisms, respectively (Fig. 4.3). Interestingly the oblique earthquake was found to have larger variability in the non-DC components compare to the normal earthquake (Fig. 4.4a). The best solutions for the oblique mechanism are more widely distributed in the NSS. The differences in the NSS distribution and non-DC compo-

nents between the two types of DC mechanisms are likely the result of different radiation patterns, and the non-uniform sampling of the radiation from the sparse station coverage. All stations except one are located to the west of the source (Fig. 4.1).

Total moment from the full MT solution is quite close to the true value, estimates of seismic moment are all within 10% of the true value. The source depth can be determined from the goodness of fit curve (Fig. 4.4b), however there is some mechanism sensitivity. The source-type plots (Fig. 4.4b) illustrate the tradeoff between source depth and mechanism that as source depth deviates from the true depth the ISO component also increases. But for both cases the MT solutions are stable with respect to source depth and the solutions with the best waveform fits (VR $>$ 60%) are between 5 and 7 km. The best fitting solutions yield the correct mechanism and depths close to the correct source depth of 4.5 km. In summary for the two DC cases, we can recover the correct fault plane solution using only regional waveforms and it appears that the 1D model assumption is adequate, but one must be careful when trying to interpret the CLVD component. Apparently the effect of 3D heterogeneity is negligible at these periods for recovering the correct DC mechanism using a 1D model, but 3D heterogeneity can increase contributions from the CLVD. However, the NSSs show a pure DC mechanism fits the data equally well and can be used to quantify the level of variability in the non-DC components (Fig. 4.4a).

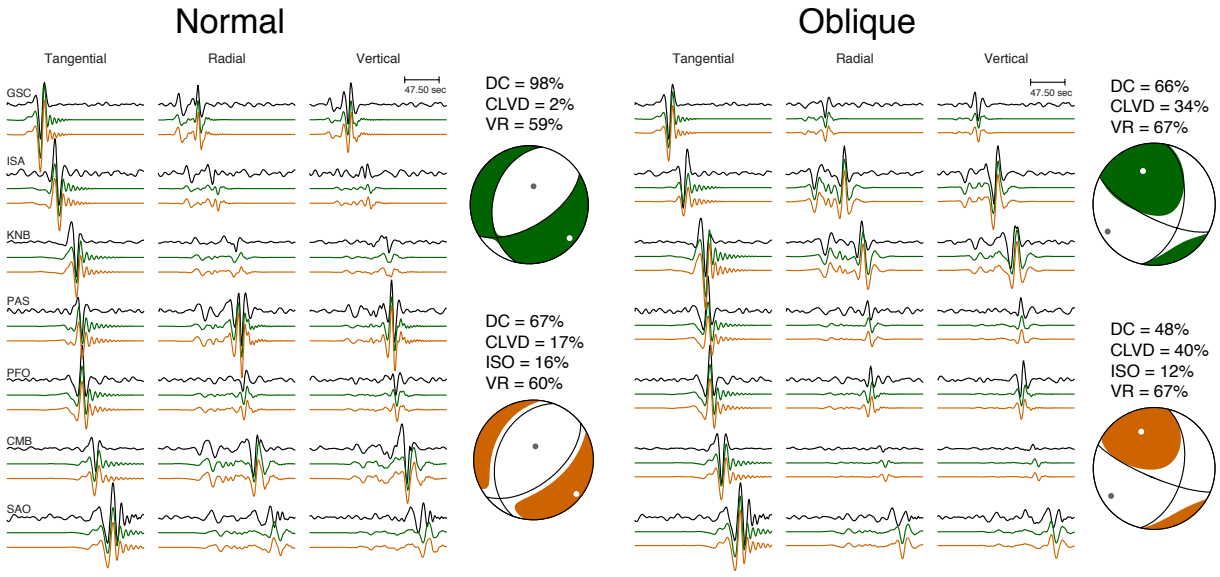

Figure 4.3: The simulated 3D data is in black, the deviatoric solution is in green and the full solution is in brown. All waveforms are in displacement (cm).

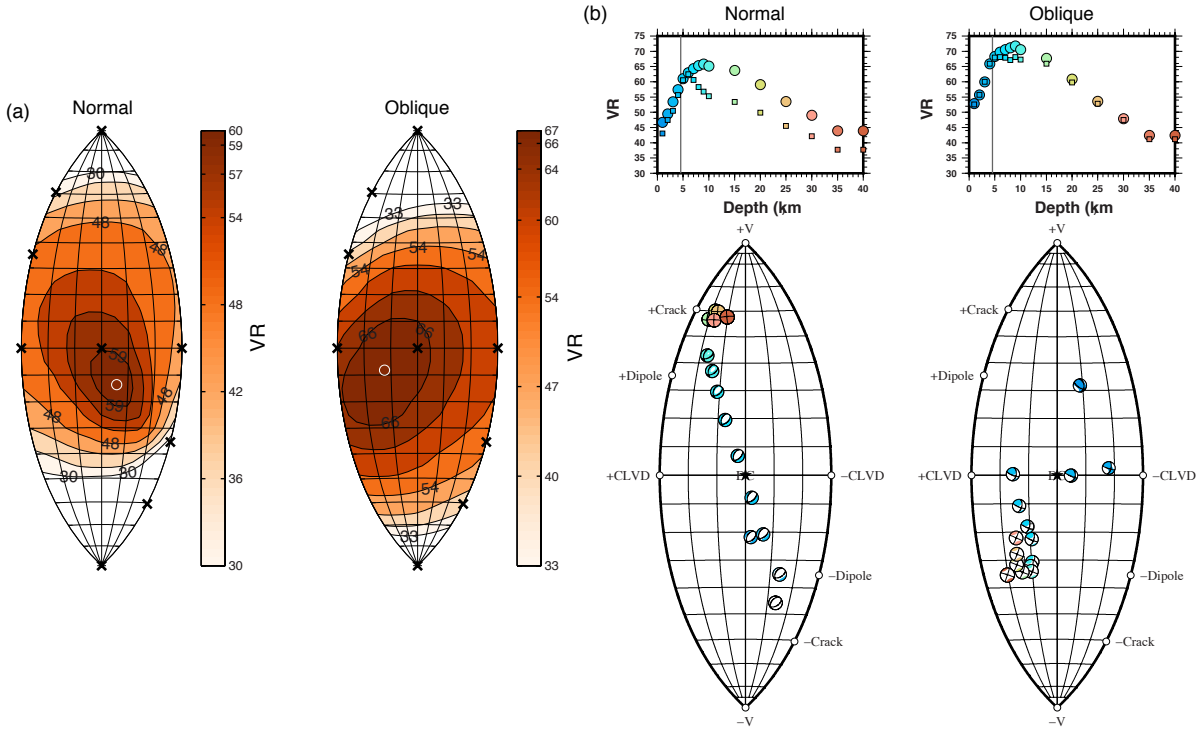

Figure 4.4: (a) Network Sensitivity Solutions color-coded by variance reduction (VR) presented on the Tape and Tape (2012a) and Tape and Tape (2012b) Lune. The white circle represents the location of the best full moment tensor solution in source-type space. (b) VR with respect to source depth for two different DC mechanisms and color-coded by source depth. The filled circles are full moment tensor solutions and the filled squares are deviatoric moment tensor solutions. The full moment tensor solutions are also plotted in source-type space and color-coded by source depth as well.

4.4.2 Isotropic Sources

A direct comparison between 1D and 3D synthetic data for the explosion case shows more variation in waveforms compared to the earthquake cases (Fig. 4.5), which is likely due to the shallow explosion source depth that was considered (500 m). In addition, the averaged 1D model is less representative of the shallow structure in the 3D tomographic model. Since the isotropic source radiation pattern has no azimuthal dependence, variations in waveforms due to the 3D structure are more prominent; whereas an earthquake source imposes an order of magnitude variation in the radiation pattern as a function azimuth. At long periods the source variation is large compare to the effects of 3D structure in this long-period passband. The recoverability of the explosion source depth is similar to what was found in the previous 1D synthetic studies (Fig. 4a in Chapter 3) and real explosions (Fig. 8 in Chapter 2) in

that the source depth recoverability primarily depends on the frequency band used in the MT inversion. Because the source depth is much less than the wavelengths considered, we cannot resolve the source depth in detail and can only constrain it to be shallower than 1 km. The MT analysis shows the deviatoric MT solutions are stable at shallow depths (Fig. 4.6b), but the isotropic component is not well constrained in the full MT inversion since the isotropic component is very sensitive to the time shifts in the inversion. The full MT solutions alternate between an explosion and a CLVD mechanism with the major vector dipole in compression depending on the time shifts due to the fact that the long-period surface wave radiation of the isotropic source and a CLVD with a major vector dipole in compression are the same. The tradeoff between these two source types is seen in the NSS for this test (Fig. 4.6c), where a pure explosion mechanism obtained from a grid-search method has a VR of 75% and the full MT has a VR of 76%.

The alternation between the two mechanisms is the manifestation of the classic tradeoff for an explosion source (e.g. Ford et al., 2009b). For an isotropic source, the level of false non-ISO components in the moment tensor results from unmodeled 3D structures and the theoretical ISO-CLVD tradeoff, and thus it is difficult to tease out how much of the CLVD component is due to unmodeled 3D structure. Combining waveform and first motion polarities can eliminate the tradeoff to get the best MT, and we obtain a solution located close to the theoretical explosion (Fig 4.6c). The best solution consists of a predominantly explosive mechanism with 60% ISO, 28% CLVD and 12% DC. The MT still has a relatively high CLVD component but the level of false-DC is low. This is an important result for discrimination because it shows that unmodeled 3D structure at the typical passband used in regional distance nuclear monitoring does not introduce false-DC in the inversion results.

4.4.3 Composite Sources

Explosion processes are often not purely isotropic, and they typically exhibit evidence of complex seismic radiation, particularly from the presence of long-period Love wave energy. Large non-ISO components have been observed in real explosion data, sometimes referred to as tectonic release (e.g. Massé, 1981; Ekström and Richards, 1994), and this component can become large enough to reverse the Rayleigh wave polarities (e.g. Walter and Rodgers, 1999; Chiang et al., 2014) which can complicate discrimination, as well as generate long-period (20 to 50 s) Love waves that can have the largest amplitudes of all three-components at a given station (e.g. Dreger and Woods, 2002; Ford et al., 2009a). In addition, shear failure is often seen in real explosions (Toksöz et al., 1965; Toksöz and Kehrer, 1972; Burger et al., 1986; Day et al., 1987). Therefore it is necessary to examine whether the MT inversion method breaks down and can become biased when both the effects of complex source processes and unaccounted for 3D effects are included, and whether the ability to successfully identify a given seismic event as an explosion can be compromised.

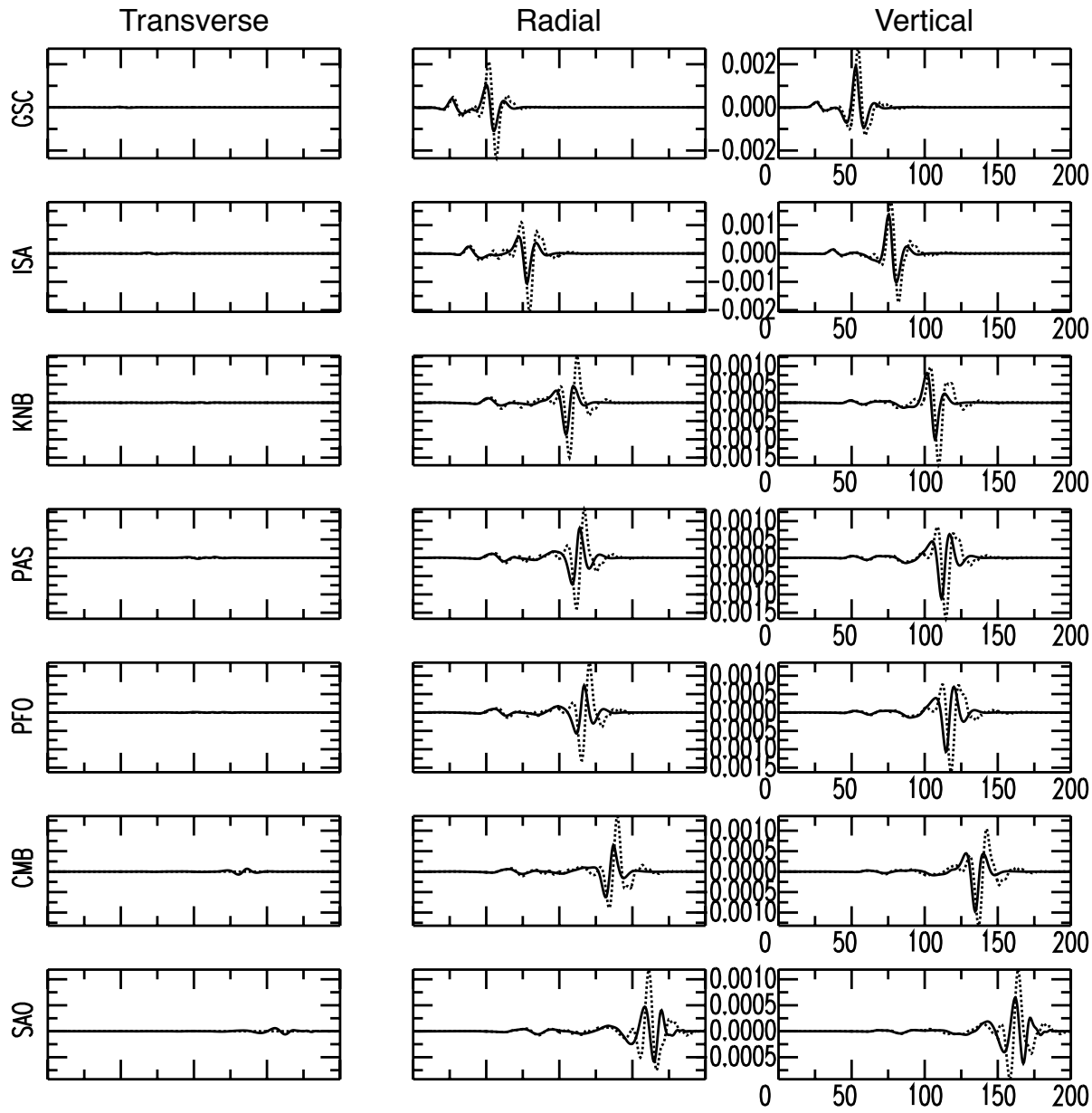

Figure 4.5: Dashed lines are waveforms calculated using a 1D Earth model and solid lines are waveforms calculated using a 3D Earth model. The waveforms are in displacement (cm) and band-pass filtered between 10-50 seconds.

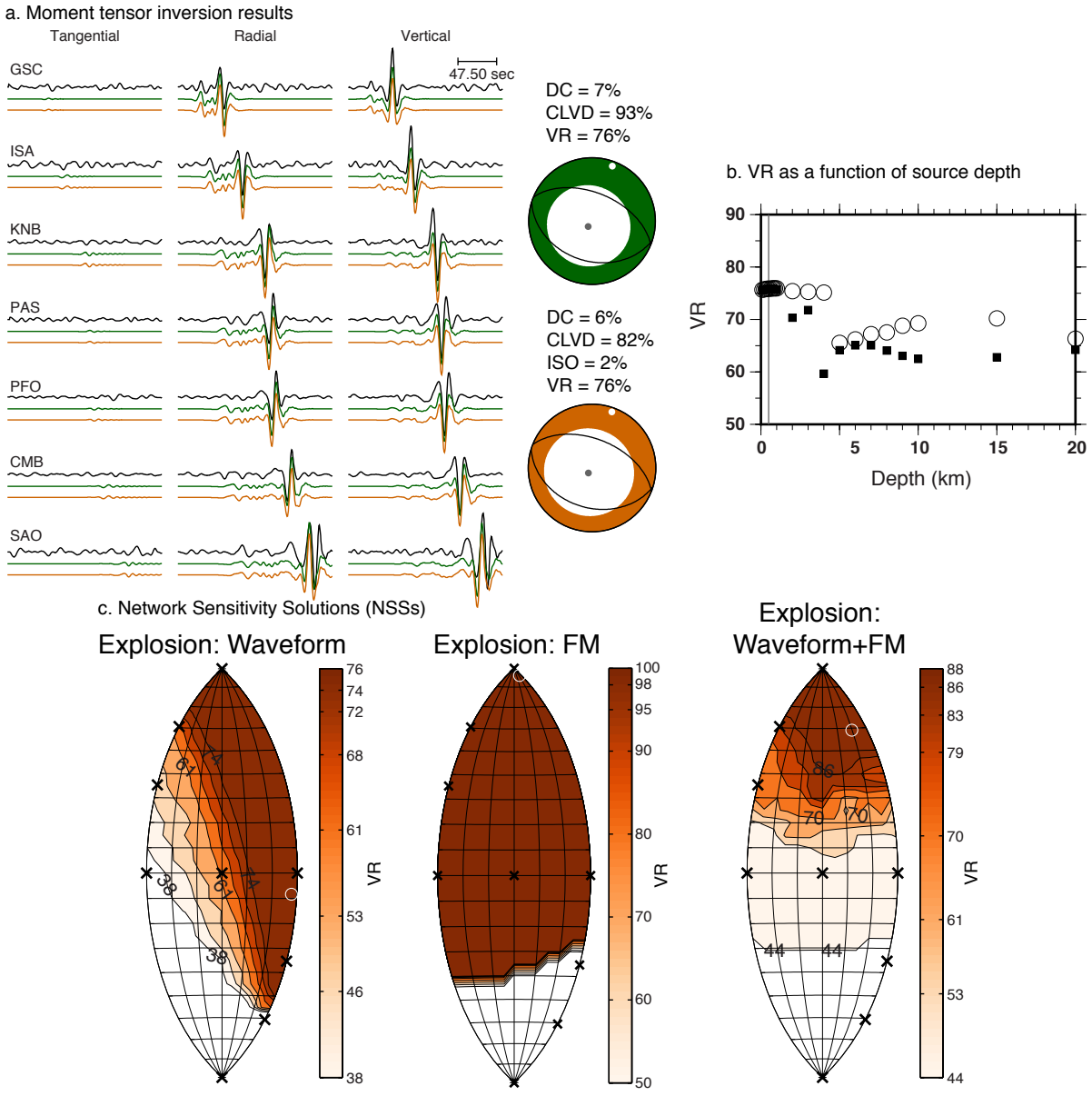

Figure 4.6: (a) Explosion moment tensor solutions and waveform fits from 10 to 50 seconds. The simulated 3D data is in black, the deviatoric solution is in green and the full solution is in brown. All waveforms are in displacement (cm). (b) Variance reduction (VR) as a function of source depth. Circles are full moment tensor solutions and the squares are deviatoric moment tensor solutions. (c) Network Sensitivity Solutions using only waveforms, only first motions or combining waveforms and first motions. The white circle represents the location of the best full moment tensor solution in source-type space.

The composite source considered here consists of a pure explosion and reverse mechanism (strike= 135; dip= 40; rake= 105) both at 500 m depth. We apply the same data processing procedure and station configuration used for the DC and ISO cases, and added random Gaussian white noise. For a composite source that is predominantly explosive, the combination of 3D effects and source tradeoff appears to have an impact on the inverted solution. The level of CLVD can be as high as 60% (for the case with 40% DC). The MT solutions and waveforms fits for a composite mechanism with 30% DC is shown in Figure 4.7a. The full MT solution is 45% CLVD suggesting that the solution is still dominated by the theoretical trade-off for explosive mechanism. Figure 4.7b shows that the solutions for composite sources with varying percentages of DC are still dominated mostly by the explosion-CLVD trade-off and the waveform NSS distributions remain more explosive-like even as the contribution from the DC increases. Although the recovered DC components for the MT inversions are close to the input value (30% DC), the inversions do not recover the correct DC mechanism. Instead of a reverse mechanism the full MT inversion for a composite source with 30% DC recovers a normal mechanism (strike= 169; dip= 72; rake= -104). The inversion recovers a shallow dipping reverse component only when the DC contribution reaches 50% (Fig 4.7b). The orientation of the DC cannot be resolved for a predominately explosive composite source. The results of this test and the previous tests indicate that there can be substantial variability in the minor components of a recovered moment tensor. These minor components appear to be the most strongly affected from the unaccounted for 3D velocity model. It is good news, however that the primary moment tensor components, namely a DC for tectonic earthquakes, and the isotropic component for explosions are not strongly affected and therefore the discrimination of the two types of mechanism remains robust.

4.4.4 Path Calibrations

One solution for trying to reduce possible MT solution bias due to unaccounted for 3D wave propagation effects is to develop source-receiver specific 1D velocity models. Given earthquake data in the source region and independent constraint on the focal mechanism, it would be possible to perform broadband waveform modeling either by forward modeling, genetic algorithm, or full grid-search approaches (e.g. Dreger and Helmberger, 1990; Bhattacharyya et al., 1999; Baise et al., 2003; Kim et al., 2011) to improve the source-receiver velocity. On the other hand if there is independent information from tomography and receiver functions the information can be used to compute path specific 1D models to improve seismic MT recovery in regions of large lateral heterogeneity (Tkalčić et al., 2009). Here we use the 3D synthetic data to evaluate the procedure of using source-receiver path specific 1D velocity structure interpreted from tomographic models.

We use the averaged elastic properties and attenuation from the 3D tomographic model for each source-receiver pair, with a total of seven path-specific 1D velocity models (Fig.

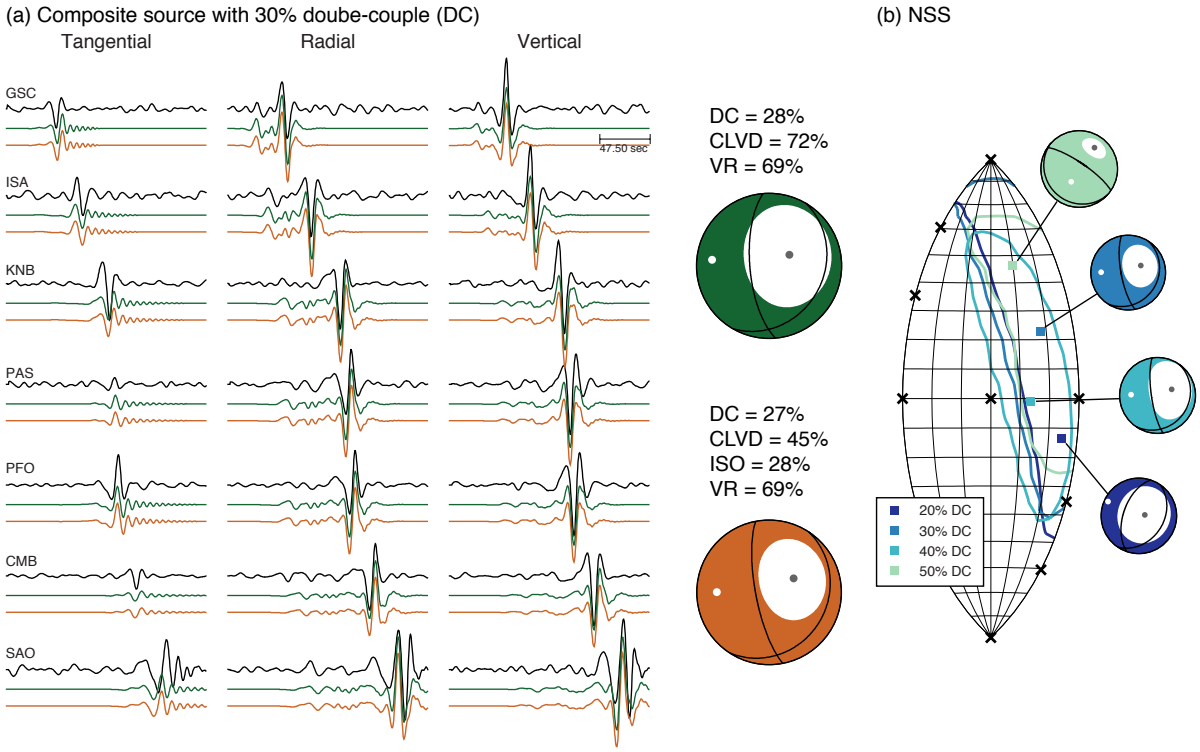

Figure 4.7: (a) Deviatoric (green) and full (brown) moment tensor solutions and waveform fits. The simulated data for an explosion plus reverse fault mechanism are in black. The example shown here is a composite source with 30% DC. (b) The best-fitting full moment tensor solution and NSS in source-type space for four composite sources. All solutions have the same mechanism (explosion + reverse fault) but different percentage of DC. The contours represent moment tensor solutions with normalized VR$\geq$ 98%.

4.8a) and compute the Green's functions for each of these models. The average 1D models have slightly shallower sediment layer and mantle velocities compared to the Song et al. (1996) model. But the Moho depths are very similar (within 5 km) for all the models. Our synthetic study shows path-specific calibration does help in cases where one simple layered model cannot adequately characterize the underlying Earth structure between different source-receiver pairs, it reduces the non-DC components in earthquakes in the time-domain waveform inversion and increases the waveform fits. The MTs are 88% and 69% DC for the normal and oblique mechanisms, respectively. The biggest difference in the NSS using a universal 1D model for all stations and using path-specific 1D models for the pure DC sources is that for the path-specific models the goodness of fit distribution is centered on the pure DC solution and is not shifted along the deviatoric or isotropic axes. Comparing Figure 8b to Figure 4 we see that the region of best fitting solutions (normalized VR$\geq$ 98%) has a smaller distribution for the oblique mechanism whereas for the normal mechanism the

area of the contoured region remains similar to the results using a single velocity model. For the explosion case, the tradeoff between explosion and CLVD persists although the best solution becomes more isotropic compared to the result without path calibration. For the composite source with 30% DC, the best MT is explosive and the CLVD has reduced to only 12%. However we still cannot recover the correct DC mechanism, which is surprising, the recovered fault plane solution is a shallow dipping normal mechanism. In this study, we found that the DC sources benefited more from the path-specific approach.

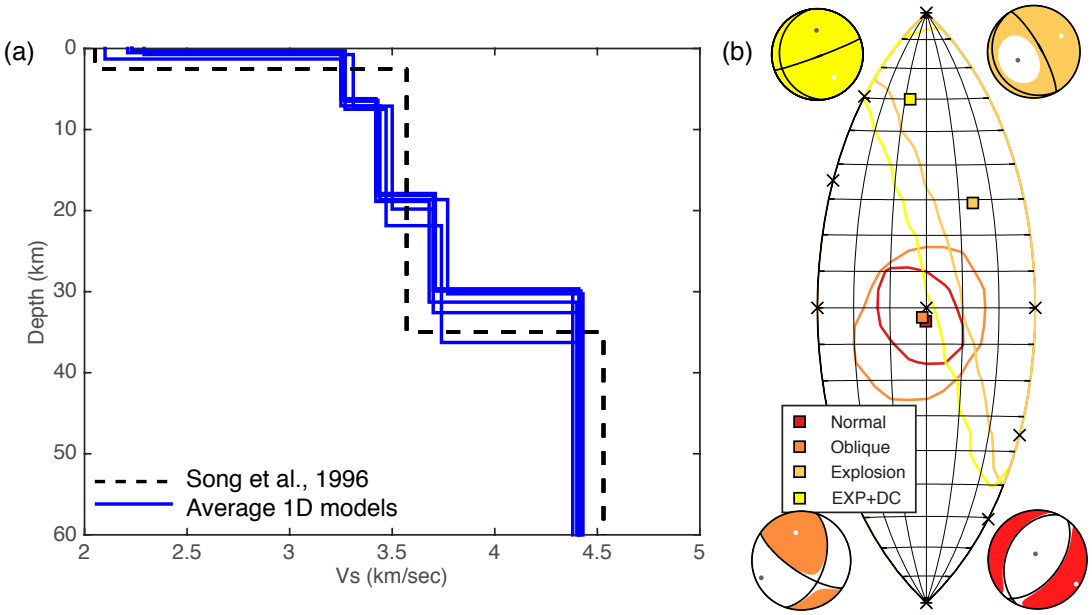

Figure 4.8: (a) Seven 1D models derived from the 3D model by Moschetti et al. (2010). (b) Full moment tensor solutions and NSS result using path-specific 1D models for each source-receiver pair. The contours are the best-fitting solutions with a normalized VR$\geq$ 98%.

4.4.5 Random Velocity Perturbations

Since the 3D tomographic models are smooth representations of Earth structure we wanted to examine a more severe case in which we apply random velocity perturbations in the model to increase the effects of scattering and multipath in the 3D synthetic data. A realistic description of the inhomogeneous Earth can be described by the von Karman correlation function (Goff and Jordan, 1988):

$$C(r) = \frac{r_\upsilon K_\upsilon(r)}{2_{\upsilon-1}\Gamma(\upsilon)} \tag{4.1a}$$

$$r = \sqrt{(\frac{x}{a_x})^2 + (\frac{y}{a_y})^2 + (\frac{z}{a_z})^2} \tag{4.1b}$$

K_υ is the modified Bessel function of the second kind order υ, where $0 < \upsilon < 1$. υ is the Hurst number which describes the roughness of the medium, Γ is the Gamma function, x, y, and z are vectors in the 3D random field, and a_x, a_y, a_z are the correlation distances. The von Karman correlation function is self-variant and rich in short wavelength components, making it a common approach to model geologic structures with a fractal nature over a wide scale (Wu, 1982). The Hurst number, which controls the correlation decay, is typically less than 0.5 from modeling of seismic reflection data (e.g. Holliger and Levander, 1992; Nielsen and Thybo, 2006). Correlation distances on the order of a few kilometers to tens of kilometers have minimal effect on the 10 to 50 second waves, therefore very large values are necessary to observe changes in the synthetic waveforms relative to the smooth 3D model in the period range of interest. We use a Hurst number of 0.3 and horizontal and vertical correlation lengths of 250 km and 50 km, respectively, to perturb the crustal velocities. We apply velocity fluctuations up to 20% (Fig. 4.9) and obtain a rough model with crustal velocities following a von Karman distribution. Figure 4.10a shows the perturbed model at 5 km depth. The velocity contrast between the California coast and the Basin and Range is preserved but with rough edges. Figure 4.10b shows a cross section of crustal velocities from the coast to the Nevada Test Site, near the location of the synthetic source (-116 degree longitude). The layers are well defined but with small-scale heterogeneities scattered throughout the crust.

We generate 3D synthetics using the perturbed model for a normal earthquake and an explosion, and compare the MTs to the solutions from the smooth model. A comparison between normal earthquake synthetics generated from the 1D model and perturbed 3D model low-pass filtered at 0.15 Hz shows the complexities due to scattering in the 3D synthetics (Fig. 4.11). The scattering (ringing) on the tangential component in the 1D synthetics is due to the low velocity layer in the 1D model (Fig. 4.8a). When these data were inverted from 10 to 50 seconds a normal mechanism was obtained but the goodness of fit was lower than the typical level (VR$>$ 60%) considered indicating a well-constrained solution. Figure 4.12a shows the deviatoric MT is 83% DC, which is 10% lower than the solution using the smooth model, whereas the full MT remains similar to the previous result (Fig. 4.3) with 68% DC. But the NSS (Fig. 4.12b) shows the population of best-fitting solutions (VR$\geq$46%) deviates further away from a pure DC source and are more broadly distributed compare to Figure 4.4a. The increase in the area of the best-fitting MTs can be interpreted as increasing bias in the solution due to unmodeled structure.

In contrast to results for the smooth 3D model, explosion deviatoric and full MTs (Fig. 4.13a) show false-DC components increased to almost 50%. VR is 57% for both deviatoric and full MTs, a value close to the level of fit for a well-constrained solution, and a pure explosion mechanism obtained using a grid-search method has a VR of 52%. Although the

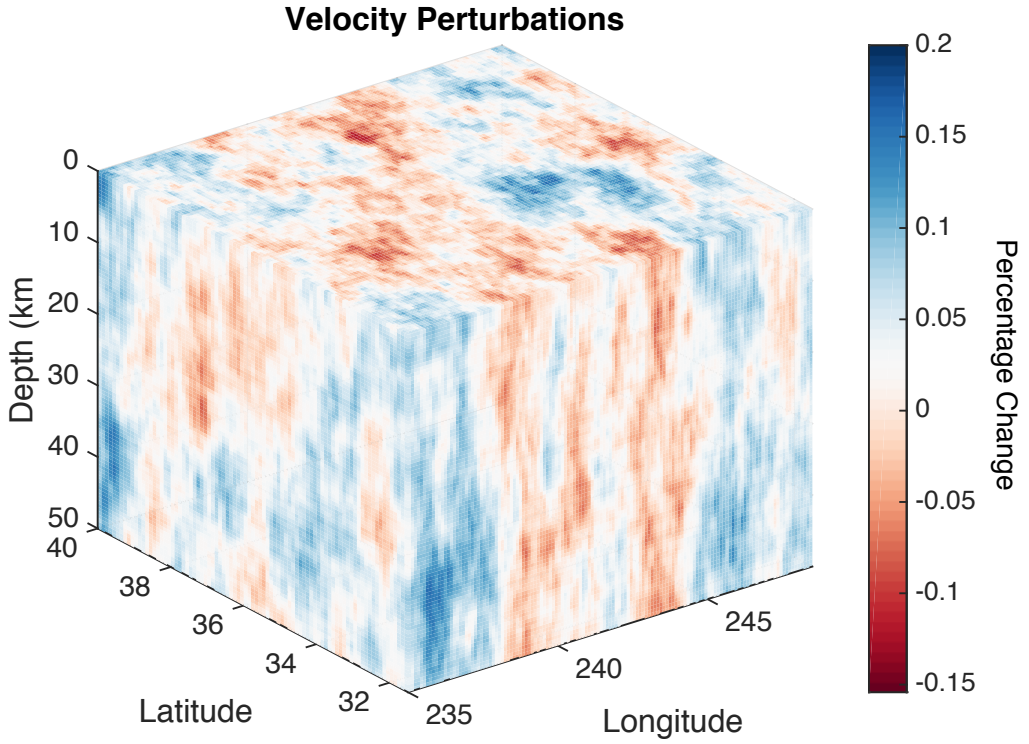

Figure 4.9: Velocity fluctuations following a von Karman distribution with a Hurst number of 0.3, horizontal and vertical correlation distances of 250 km and 50 km, respectively.

waveform NSS (Fig. 4.13b) still shows an explosion-like distribution the best-fitting solutions encompass almost half of the area in the source-type space, including a pure DC source. The first motion constrained NSS eliminated the tradeoff and pure DC source types but compared to Figure 4.6c the uncertainties estimated from the constrained NSS are slightly larger. The first motion-constrained full MT solutions for the smooth and perturbed 3D model are both 60% ISO, but the solution for the perturbed model has a slightly greater DC of 31%. In this study we show that the MT uncertainty increases when the 3D model becomes more heterogeneous and the false-DC component increases when an explosion source is considered.

4.5 Conclusion

The results of the synthetic 3D model sensitivity tests show that using 1D velocity models to compute Green's functions for use in long-period (as short as 10 seconds) MT inversions is reasonable, and that at least synthetically we do not find significant bias in solutions,

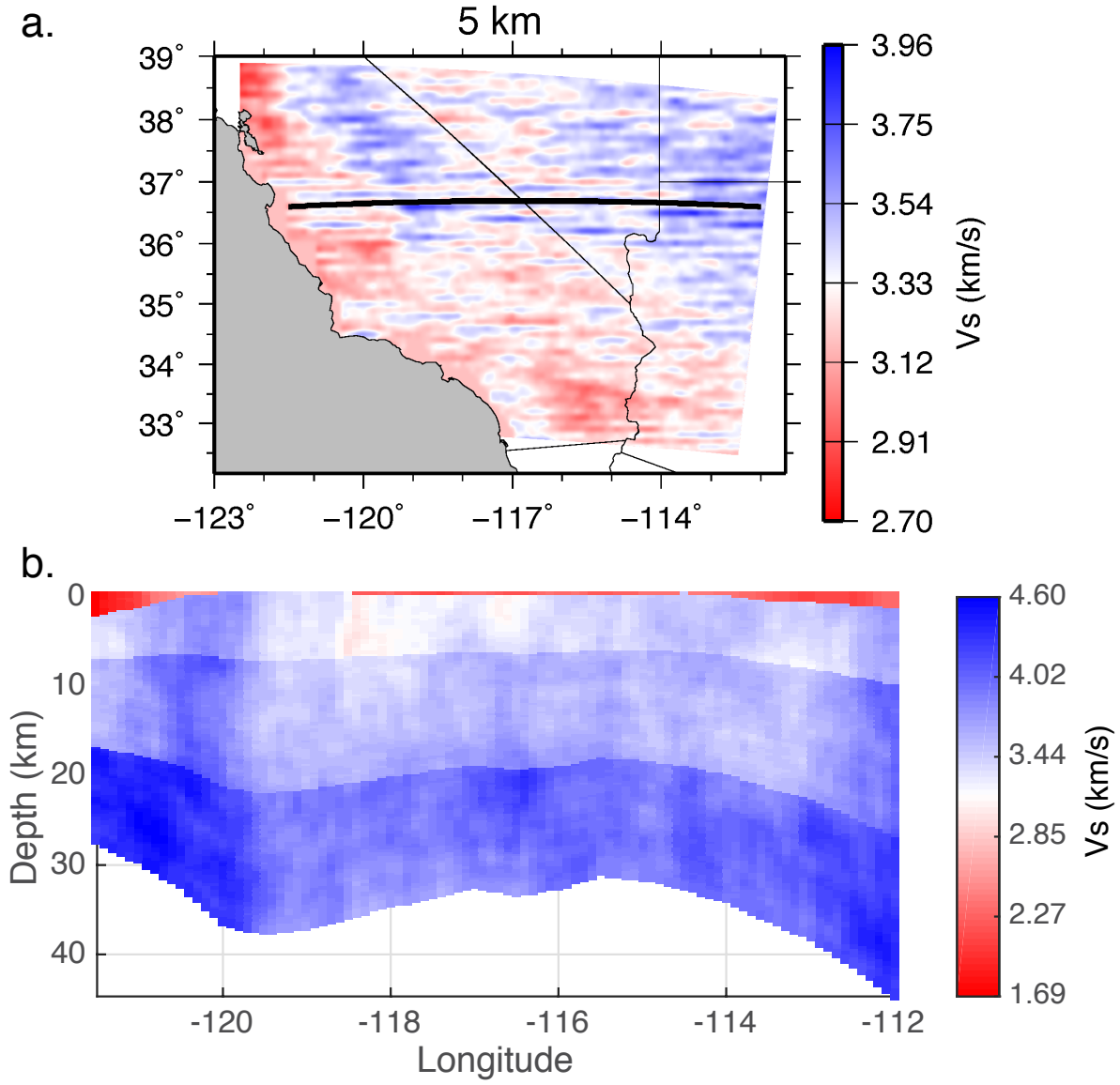

Figure 4.10: (a) Shear wave velocities (Vs) at 5 km depth. Black line denotes the location of the cross section. (b) Cross section of the crustal velocities at depth.

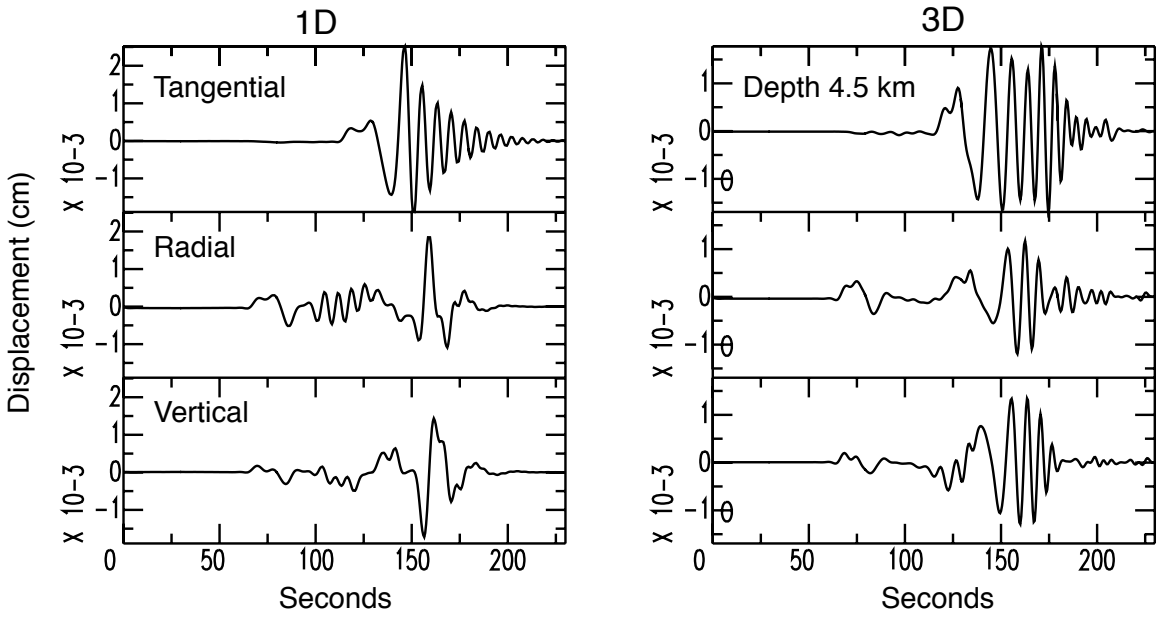

Figure 4.11: 1D and 3D synthetic waveforms for a normal mechanism (strike=202; rake= −100; dip=36) at SAO. 3D synthetics are computed from the perturbed model.

nor issues in being able to discriminate different types of sources. For the DC case, we can recover the correct mechanism and source depth using a universal 1D velocity model for all stations. The ISO component in the full MT is less than 20% for the two DC mechanisms explored. But for the oblique mechanism the inversion recovers a solution with a high CLVD component, resulting in a solution that is 50% DC. The observation of false non-DC components up to 50% for the earthquake source shows that although the correct fault plane solutions for the DC can be recovered at relatively long periods, the CLVD component can be large in full MT inversions, however the NSS remains earthquake-like focused at the origin of the source-type plot. For the explosion cases, the level of false non-ISO is dominated by the ISO-CLVD tradeoff, although the recovered MT consists of a CLVD solution the DC component is less than 10%, and the NSS exhibits the typical explosion-like signature in source-type space (e.g. Ford et al., 2010). Including additional data from first motion polarities can eliminate the trade-off and the correct solution can be recovered. The constrained MT solution is predominantly explosive and has a very low DC of 9%. Similarly, results for the explosive composite source show the tradeoff affects the recoverability of the MTs. The fault plane orientation of the DC component in a composite source cannot be constrained well, except for the case with 50% DC and 50% ISO. Results from synthetic tests using a more heterogeneous 3D model with crustal velocity fluctuations following the von Karman distribution show the full MT inversion can recover the correct DC mechanism. The percentage of non-DC remains the same compare to the result for a smooth model but the

solution has higher uncertainties as indicated by lower waveform fits and larger variability in the NSS. When an explosion source is considered the false-DC component increases to almost 50% in the inversion. The NSS exhibits an explosion-like signature in the source-type space but with large variability that extends to a pure DC source. But considering the best solution with first motion constraints shows a predominantly explosive source with a slightly higher DC of 28% compare to the results from a smooth model. The false non-DC components in earthquakes and the false-DC components in explosions arising from unaccounted for 3D path effects can be reduced by using path-specific 1D Green's functions. The Green's functions are computed by taking the average 1D model for each source-receiver path from the 3D tomographic model. Path-calibration also reduces the large uncertainty in the NSS for the oblique mechanism.

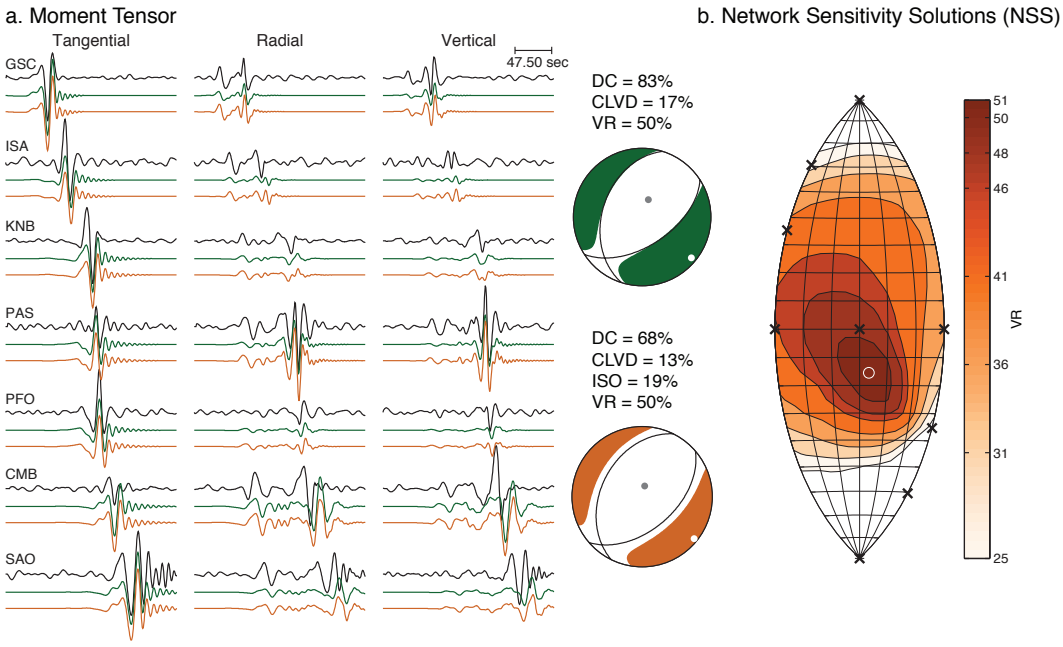

Figure 4.12: (a) Normal earthquake moment tensor solutions and waveform fits at 10 to 50 seconds. The simulated 3D data using the perturbed model is in black, the deviatoric solution is in green and the full solution is in brown. All waveforms are in displacement (cm). (b) NSS using only waveforms and combined waveforms and first motions. Solutions are color-coded by VR. The white circle represents the location of the best full moment tensor solution in source-type space.

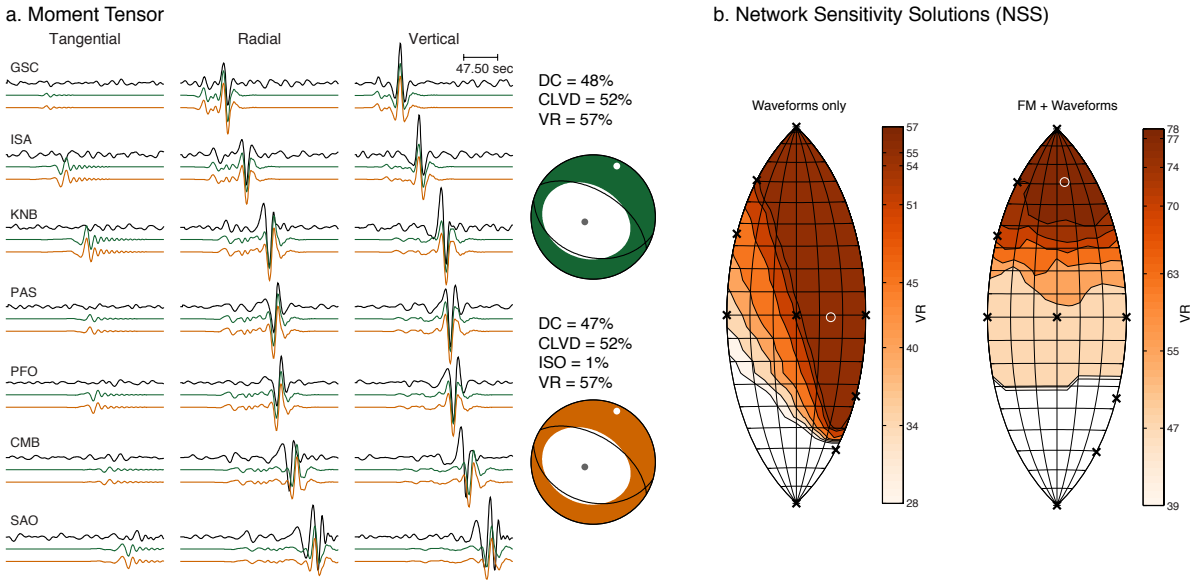

Figure 4.13: (a) Explosion earthquake moment tensor solutions and waveform fits at 10 to 50 seconds. The simulated 3D data using the perturbed model is in black, the deviatoric solution is in green and the full solution is in brown. All waveforms are in displacement (cm). (b) NSS using only waveforms and combined waveforms and first motions. Solutions are color-coded by VR. The white circle represents the location of the best full moment tensor solution in source-type space.

Chapter 5

Comparing 1D and 3D Source Inversions: Application to the Western United States

5.1 Abstract

In this study we have established a procedure to compare and evaluate source inversions using both 1D and 3D velocity model Green's functions. The 3D velocity model Green's functions are computed with the finite-difference approach invoking source-receiver reciprocity (Eisner and Clayton, 2001; Graves and Wald, 2001; Aki and Richards, 2002; Dahlen and Tromp, 1998). Using the complete waveform moment tensor (MT) inversion method (Minson and Dreger, 2008) we analyze earthquakes and explosions at the Nevada Test Site (NTS) and compare the MT and associated uncertainties at different period bands using both the 1D and 3D Green's functions. At long periods (20-50 seconds), there is good agreement in the solutions for the two velocity models, with slight improvement in waveform fits when using the 3D velocity model Green's functions. At shorter periods (8 to 20 seconds) the advantage of the 3D model is limited except for paths along BKS and MHC where the 3D velocity model Green's do provide better waveform fits. There is no clear reduction in source uncertainties when using the 3D velocity model Green's functions, and a larger event sample size is required to make useful interpretations about the use of 3D models in estimating source uncertainties. The results indicate that the 3D model for the Western U.S. still needs further refinement to adequately model wave propagation at short periods for the purpose of routine source inversion. Although 3D Green's functions are computationally expensive the calculation only has to be performed once. Once the database of pre-computed 1D and 3D Green's functions is compiled, the MT inversion can be easily automated for monitoring purposes.

5.2 Introduction

Obtaining reliable source mechanisms of small magnitude seismic events at regional distance can be challenging due to poor station coverage, high noise levels in the long period waves, or both. Commonly long period waveforms are utilized to minimize errors due to unaccounted Earth structure, but with small magnitude events the signal-to-noise ratios (SNR) of long period waves often degrade rapidly with increasing distance from the source. The need for regional distance monitoring of low yield explosions therefore necessitates the use of shorter period information that may have higher SNR, but which also requires Green's functions (GFs) that account for the more complex short period wave propagation. Recent advancements in waveform modeling and high-performance computing techniques have made the use of source inversions at relatively short periods and structurally complex regions an attractive and viable option, and has been shown in several studies (Ramos-Martínez and McMechan, 2001; Liu et al., 2004; Zhao et al., 2006; Walter et al., 2010; Covellone and Savage, 2012) to be effective. However, there has not been a systematic analysis of the impact of 3D velocity structure on the estimation of seismic source parameters for the purpose of explosion monitoring.

The efficacy of GFs depends on the accuracy of the 3D model. Using a 3D reference model to account for complex wave propagation in and near the Los Angeles Basin, Liu et al. (2004) and Lee et al. (2011) computed source mechanisms of small to moderate-sized earthquakes in Southern California using the spectral element method and finite-difference method, respectively, and found good agreement between the 1D and 3D solutions. Hingee et al. (2011) observe improvements in 3D synthetics over 1D synthetics for some regions in Australia. The reduction in waveform misfit is limited to certain regions suggesting the 3D model for the Australian region needs further improvement. Covellone and Savage (2012) computed deviatoric and full moment tensors (MTs) for 195 Mw$\sim$5.5 earthquakes in the Middle East and found little difference among the solutions due to the fact that a large number of observations are available to provide good constraints in the full MT inversion. They compared the deviatoric 1D and 3D MTs and found that there is an improvement in waveform fits and a reduction in the non-double-couple (non-DC) components when using 3D GFs. Although it is important to note that in their comparison study, the 3D synthetics were evaluated against 1D synthetics computed from the preliminary reference Earth model (PREM; Dziewonski and Anderson, 1981).

The focus of most studies has been on earthquakes, the application of 3D source inversions on non-DC events have not been thoroughly investigated. Walter et al. (2010) computed full MT solutions for icequakes near the base of the Swiss Alpine Glacier and determined seismic events are results of near-horizontal tensile cracks. The authors concluded the 1D models provided robust estimates of the source parameters, although the more complex 3D model improved the fits between data and synthetics, particularly for reflections from the basal moraine and rock. There has not been a systematic study of the effects of 3D GF on

the recovery of seismic MT of explosions and the effect on discrimination capability.

The purpose of this study is to develop a platform to perform routine 3D MT inversions and to compare source-type discrimination results for explosions and earthquakes using both 1D and 3D GFs. The same techniques (e.g. Ford et al., 2010) developed to evaluate the quality of 1D models can also be applied to 3D models. Ford et al. (2009a) obtained full MT solutions using a well-calibrated 1D model (Song et al., 1996) for explosions, earthquakes and mine collapses in the western United States. In this study we compare 1D and 3D full MT solutions at two frequency bands: 20 to 50 seconds and 8 to 20 seconds. The high frequency cutoff is limited by the resolution of the Earth model. We use the 3D surface wave tomography model by Moschetti et al. (2010) determined from surface wave dispersion measurements at periods as short as 6 seconds. Of the 32 explosions, earthquakes and collapses previously studied by Ford et al. (2009a), we select six explosions and earthquakes in the vicinity of the former Nevada Test Site (NTS) for source inversions. The events are listed in Table 5.1 where the earthquake event information comes from the Northern California Seismic Network (NCSN) and the explosion event information comes from Springer et al. (2002). We apply the source-receiver reciprocity principle to compute 3D GFs using the finite-difference (FD) method (Eisner and Clayton, 2001; Graves and Wald, 2001). The advantage of seismic reciprocity is a drastic decrease in computation cost, especially when the number of sources outweighs the number of receivers, because for a set of three FD simulations in which unit forces are applied at the receiver location in the north, east and vertical directions the complete MT GF can be determined at all interior points in the model. Thus in the monitoring of a region it is possible to develop GF over the desired depth range for a calibrated 3D model obtained independently from tomography or other methods.

Table 5.1: Table 1. Event Information

Name	Date	Latitude	Longitude	Depth (km)	Magnitude
Amargosa	1996/09/05, 08:16:56.09	36.6827	-116.3378	5000	3.38 (Md)
Little Skull Mt.	2002/06/14, 12:40:45.82	36.6438	-116.3448	8750	4.32 (Md)
METROPOLIS	1990/03/10, 16:00:00.08	37.112	-116.056	469	4.94 (Md)
COSO	1990/03/10, 16:00:00.08	37.104	-116.075	417	4.50 (Md)
HOYA	1991/09/14, 19:00:00.08	37.226	-116.429	658	5.40 (Md)
JUNCTION	1992/03/26, 16:30:00.00	37.272	-116.361	622	4.82 (Md)

5.3 Method

We perform the MT inversion in the time-domain using three-component displacement seismograms for receivers located in the western United States (Fig. 5.1). The data are instrument corrected, rotated to the radial, transverse and vertical components and bandpass filtered between 8 to 50 seconds period using an acausal 4-pole Butterworth filter. For the 3D MT inversions, an additional step is taken by convolving the data with the Gaussian source time function used to compute the 3D GFs via the FD method. This is done since it is more stable to convolve the finite-difference source time function with the data, essentially applying a filter, than it is to deconvolve the source time function from the computed Green's functions. We use data recorded at stations from the Berkeley Digital Seismic Network (BSDN), Southern California Seismic Network (SCSN) and the Lawrence Livermore Seismic Network. The United States Geological Survey, Berkeley Seismological Laboratory and California Institute of Technology jointly manage the networks in California. BDSN and SCSN data and instrument responses can be obtained from the Incorporated Research Institutions for Seismology Data Management Center (IRIS DMC, http://ds.iris.edu/ds/nodes/dmc/) and the Northern California Earthquake Data Center (http://www.ncedc.org/).

5.3.1 Inversion Procedure

The MT inversion follows the method developed by Minson and Dreger (2008) where the complete waveform is inverted in a weighted linear least square formulation. The displacement waveform is expressed as a linear combination of the GFs weighted by the MT elements. The first step is data preparation where the hypocenter and station location are specified, and the data are processed as described in the beginning of this section. After reading the data files, the MT inversion algorithm then loads the pre-computed GFs for each station, and performs a waveform cross-correlation between the data and GF at each station to determine the initial time shifts (Pasyanos et al., 1996). A more detailed description on computing the GF is provided in the next subsection. The time shift that gives the highest correlation between data and GFs is selected (Pasyanos et al., 1996). We do not allow for time shifts greater than half a cycle of the minimum wavelength to avoid cycle shifting. Applying time shifts prior to the actual inversion is a common procedure used to account for imperfect travel time predicted by the model and errors in event origin time. The final step is the inversion where we do not constrain the inversion to have zero trace, instead it solves for all six components of the seismic MT.

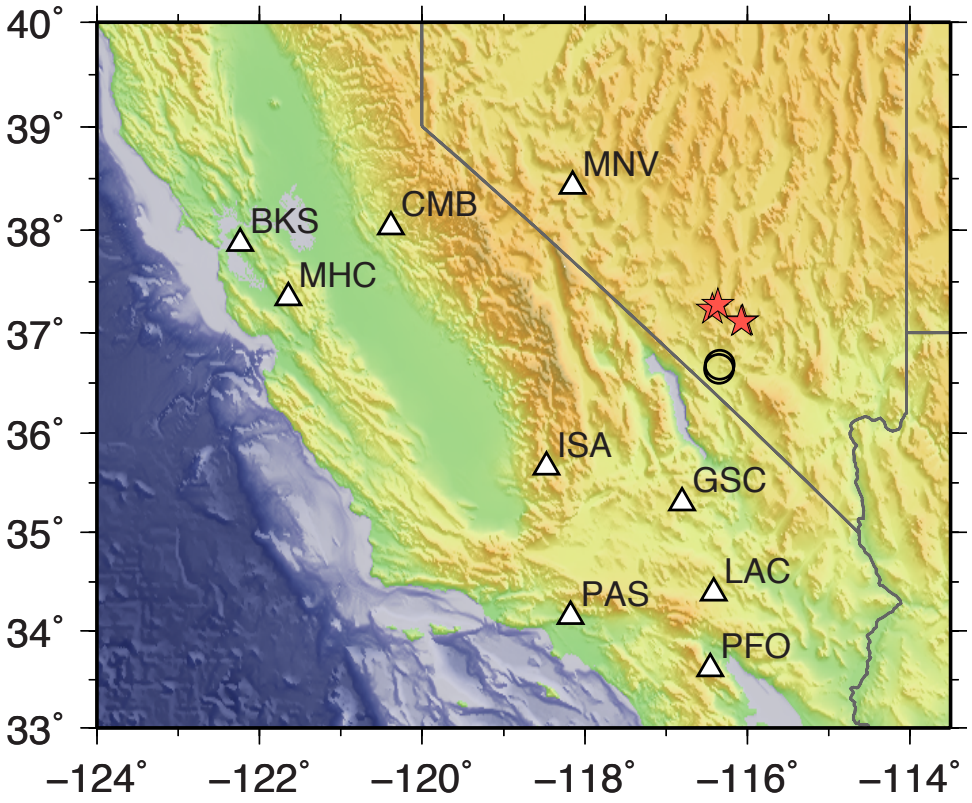

Figure 5.1: Map of the western United States. Red stars are Nevada Test Site (NTS) explosions, black circles are earthquakes and the white triangles are broadband seismic stations.

5.3.2 Reciprocal Green's Functions

We compute elastodynamic GFs for each source-receiver pair using 1D and 3D Earth models. The GFs are the impulse response whose orientation is given by the basic MT elements or by the fundamental fault types (e.g. Helmberger, 1983; Jost and Herrmann, 1989). The three basic faults types are the vertical dip-slip (DS), 45-degree dip-slip (DD), and vertical strike-slip (SS). Any arbitrary (full) MT can be described as a linear combination of the six basic MT elements ($Mxx, Mxy, Mxz, Myy, Myz, Mzz$), where the first index represents the direction of the force, and the second the direction of a spatial derivative. Thus Mxx, Myy and Mzz represent the strength of vector dipole forces, and Mxy, Mxz, Myz, Myx, Mzx and Mzy represent the strength of force couples. Conservation of angular momentum leads to symmetry of the MTs, where $Mxy = Myx$, yielding the 6 independent elements. For the deviatoric MT, where the trace is zero, five basic tensor elements or the three fundamental fault types can describe the seismic tensor (e.g. Langston, 1981; Langston and Helmberger, 1975).

The GFs are computed for each source-receiver pair and processed the same way as the data. The 1D GFs are computed using the western US velocity model (Song et al., 1996) and frequency wavenumber integration method (Wang and Herrmann, 1980; Herrmann and Wang, 1985; Herrmann, 2013). The 3D GFs are computed using the anelastic FD code, SW4, developed at the Center of Applied Scientific Computing at Lawrence Livermore National Laboratory (LLNL; part of the Computational Infrastructure for Geodynamics). The conventional approach to compute 3D GFs using FD is computationally expensive because we need to simulate wave propagation at regional distances with attenuation and at shorter periods. For each receiver, the number of simulations required to compute 3D GFs is six times the number of sources to compute the six basic MT elements. Therefore to reduce the computation cost we apply the reciprocity principle to compute the 3D GFs. Source-receiver reciprocity for seismic waves is given by the Betti's theorem (Aki and Richards, 2002; Dahlen and Tromp, 1998) which states that the location of the source and observation can be switched but still produce the same exact elastic response. Eisner and Clayton (2001) and Graves and Wald (2001) implemented source-receiver reciprocity using the FD approach to simulate ground motion for any number of arbitrary sources from a set of stations. The advantage of using reciprocity rather than the forward approach is that it is only necessary to run three calculations at every receiver location. Commonly there are fewer stations than sources in a typical monitoring scenario. We compute the elastic response at the source due to a single force in three orthogonal directions (X, Y and Z) at the receiver. For each reciprocal single force the numerical spatial derivative of the displacement in the interior of the model can be computed. Then it is possible to combine the derivatives to construct the individual MT components. For a single force oriented along the X direction:

$$G^X_{xx} = \frac{\partial u^X_x}{\partial x} \tag{5.1a}$$

$$G^X_{yy} = \frac{\partial u^X_y}{\partial y} \tag{5.1b}$$

$$G^X_{zz} = \frac{\partial u^X_z}{\partial z} \tag{5.1c}$$

$$G^X_{xy} = \frac{\partial u^X_y}{\partial x} + \frac{\partial u^X_x}{\partial y} \tag{5.1d}$$

$$G^X_{xz} = \frac{\partial u^X_z}{\partial x} + \frac{\partial u^X_x}{\partial z} \tag{5.1e}$$

$$G^X_{yz} = \frac{\partial u^X_z}{\partial y} + \frac{\partial u^X_y}{\partial z} \tag{5.1f}$$

There are similar equations for unit forces oriented in the Y and Z directions. We call the elastic response computed via reciprocity the reciprocal Green's functions (RGF) to

distinguish them from the conventional (forward) approach. We can then compute the X-component of displacement for an arbitrary source as the weighted sum of the RGFs:

$$u^X = M_{xx}G^X_{xx} + M_{yy}G^X_{yy} + M_{zz}G^X_{zz} + M_{xy}G^X_{xy} + M_{xz}G^X_{xz} + M_{yz}G^X_{yz} \quad (5.2)$$

The capitol superscripts refer to the component of motion, which corresponds to the direction of the applied unit force at the receiver position. Given the strike, rake, dip and scalar moment of the fundamental fault types we can compute the M_{ij} coefficients (Eq.1 in Box 4.4 of Aki and Richards, 2002), and substituting them into Eq. 5.2 we can construct the displacement response for each fundamental fault type Green's function for the moment tensor inversion.

The 3D isotropic model by Moschetti et al. (2010) is linearly interpolated in the vertical direction and smoothing is applied in the horizontal direction using Gaussian averaging. The smoothing is necessary because the velocity model is much coarser than the computation grid. For the reciprocal FD calculations we use a grid spacing of 250 m and a Gaussian source function with a duration of 0.5 seconds. We did not include any water layers or topography in the 3D calculations, and implemented attenuation using a function of local Vs [km/s] (e.g. Graves et al., 2008; Olsen et al., 2009), such that Qs = 50Vs and Qp = 2Qs. Figure 2 shows a comparison between a forward FD calculation and a reciprocal calculation. In this case, the source depth is 1 km and the receiver is 100 km away and at the surface. There is excellent agreement between the forward and reciprocal simulations.

The FD calculations were performed on the Livermore Computing Center (LC) 8-core Xeon 35-2670 Linux cluster, cab, consisting of 1,296 nodes, each with 16 cores per node and 32 GB memory. Ideally we should use the same computation domain for all the reciprocal calculations but the run time increases rather quickly at large distances due to a drastic increase in the number of grid points and the duration of the simulation. Because the 3D model is smooth and we are only comparing waveforms as short as 8 seconds, we justify using different computation domains by positioning the source and receivers to be at least 250 grid points away from the boundary and use a sufficiently large absorbing boundary layer (30 km in all directions) to minimize boundary reflections. Running on 512 processors, the run time for one RGF calculation with approximately 1.2 billion grid points and 1,1924 time steps takes about 10 hours.

5.4 Moment Tensor Inversion Results

We perform 1D and 3D MT inversion and compute Network Sensitivity Solutions [NSS] (e.g. Ford et al., 2010) for all events. For four out of the six events, we also compare the source properties in two different frequency bands. For the earthquakes (Armagosa and Little Skull Mountain), we search for the best depth using the 1D model and invert for 1D

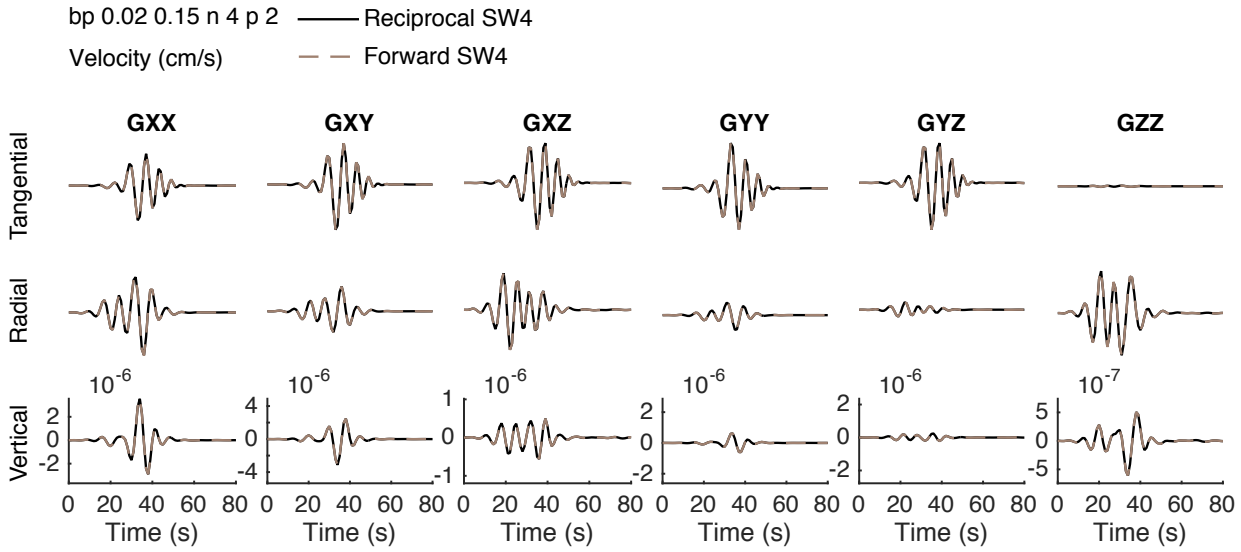

Figure 5.2: A comparison between forward and reciprocal finite-difference calculations at 100 km distance. The waveforms are in velocity (cm/s) and bandpass-filtered between 0.02 and 0.15 Hz with a 4-pole acausal Butterworth filter. The black lines are the reciprocal calculations and the brown dashed lines are the conventional (forward) calculations.

and 3D MT solutions at these depths, whereas for the explosions (METROPOLIS, COSO, HOYA and JUNCTION), we fix the source depth at 1 km for both 1D and 3D GFs. For the comparison at different frequency bands, we use data from the BDSN and SCSN networks, and when available, we also compute solutions including the LLNL network stations but since the raw data and instrument responses for these stations are currently not open we cannot compare the solutions in the different frequency bands.

5.4.1 Low Signal-to-Noise Events

COSO and Amargosa have relatively low SNR compare to the other events in this study, therefore we did not compare the 1D and 3D inversion results at different frequency bands, instead the inversion is done between 10 to 50 seconds. Figure 3a shows the full MT inversion results for COSO. The 1D solution fits the data slightly better than the 3D solution, while the moment magnitude (M_w) using the 3D model is slightly higher than that of the 1D model. Both the 1D and 3D GF inversions recover solutions that are dominated by the explosion component, representing 65% and 68% of the total seismic moment, respectively. On the other hand, the off-diagonal components of the MTs are quite different, where the 1D solution has a deviatoric component that is mostly a normal DC mechanism and the 3D solution is a mixture of vertical DS and CLVD mechanisms. Thus while the explosive

nature of the event is clearly recovered in both cases there is velocity model dependence on the lesser "tectonic" release component of the source.

For the Amargosa earthquake (Fig. 5.3b) the 1D solution is fitting 17% better than the 3D solution, a much greater difference compared to COSO. This is interesting in of itself because it clearly shows that the use of a 3D velocity model, including one that is constrained by data (surface wave dispersion) will not necessarily lead to improved ability to fit the data. The 1D and 3D fault plane orientations are also quite different where the 1D solution is closer to a normal mechanism. In contrast, the 3D solution has a vertical DS component that is significantly rotated with respect to the 1D solution. In addition, the 3D solution results in a relatively large "false" ISO of 36% of the total seismic moment. However, the ISO component is not statistically significant as determined by the F-test (Menke, 1989; Menke, 2012; Templeton and Dreger, 2006), where the level of statistical significance with the additional degree of freedom in the full MT inversion is only 50%. Nevertheless, this illustrates that imperfect 3D velocity models can also increase the ISO moment in earthquakes, contrary to the results of Covellone and Savage (2012). Although we see an increase in ISO component for short period inversions the 1D (Fig. 5.4a) and 3D NSS (Fig. 5.4b) exhibit a typical earthquake-like signature with a bullseye pattern (Ford et al., 2010).

5.4.2 2002 Little Skull Mountain Earthquake

The Md 4.3 2002 Little Skull Mountain earthquake occurred near NTS, approximately 6 km southwest of the 1992 Little Skull Mountain mainshock. At 20 to 50 seconds, we have data from five stations with an azimuthal coverage of 89°. For the comparison at long period (Fig 5.5a-c), both 1D and 3D MT solutions fit the data equally well, and have similar mechanisms. The solution is a normal mechanism and is predominantly DC. The DC component for the 3D solution is slightly higher than the 1D solution, and unlike the explosions the 1D solution M_w is higher than the 3D solution.

For the inversion at short period we did not include MHC due to low SNR. Using data from 8 to 20 second yields 1D and 3D MTs with only 50% and 16% DC, respectively (Fig. 5.5a), considerably lower than solutions from the 20 to 50 second passband. The low DC in the 3D solution is particularly alarming. The 3D solution also recovers a rotated normal mechanism with respect to long period MTs (about 40 degrees). The M_w is similar for all solutions and the 1D model performs better than the 3D model mainly because the 3D model cannot fit the tangential component as well as the 1D model (Fig. 5.5d-e). We also see an increase in variance at CMB using the 3D model. We identify ISA to be a problematic station in the 3D inversion because the synthetics cannot fit the data well with time shifts less than half the minimum wavelength (4s). Therefore the solution with the highest VR within the 4-second window is a solution with zero shifting. Considering a three-station inversion without ISA (Fig. 5.6) we obtain a solution with 52% DC and a normal mechanism

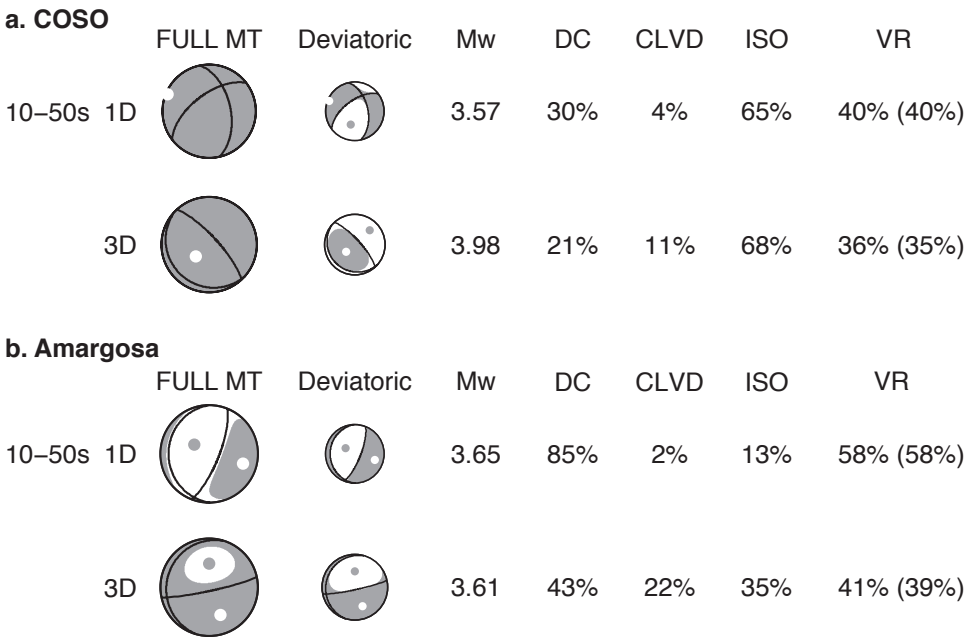

Figure 5.3: COSO and Amargosa full moment tensor inversion results with 1D and 3D Green's functions filtered between 10 to 50 seconds. Full moment tensor focal mechanism and the deviatroic component of the solution are plotted as well as the moment magnitude (M_w), percent double-couple (DC), percent compensated linear vector dipole (CLVD), percent isotropic (ISO) and variance reduction (VR). VR from deviatoric inversion is in parentheses.

consistent with long period MTs and the 1D short period MT.

Whether or not we include ISA in the 3D MT inversion, the ISO component remains high, up to 40%, which is quite large for an earthquake. However the F-test reveals the ISO component is not statistically significant with a 50% confidence level of significance for inversions with and without ISA. In addition, 1D (Fig. 5.7a) and 3D NSS (Fig. 5.7b-c) all exhibit an earthquake-like distribution and similar level of solution uncertainty where the normalized VR$\geq$95% (67%, 43% and 54%, respectively) are about the same size. Similar to Amargosa, the results show that imperfect 3D velocity models can also increase the ISO moment in earthquakes.

5.4.3 Larger NTS Explosions

We compare 1D and 3D MT inversions for three NTS explosions METROPOLIS, HOYA and JUNCTION. Of the three explosions HOYA has strong SH radiation on the tangen-

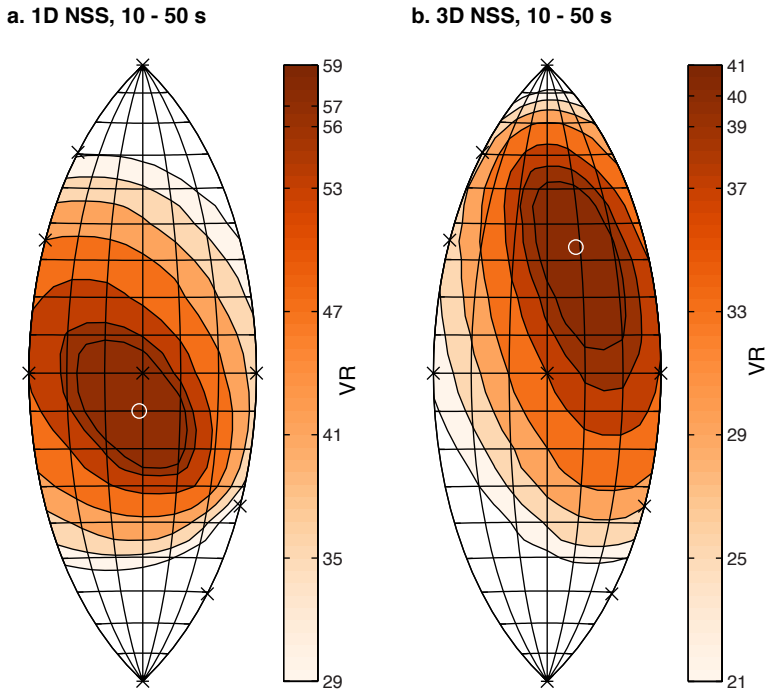

Figure 5.4: Amargosa NSS for (a) 1D and (b) 3D Green's functions filtered between 10 to 50 seconds. White circle marks the location of best full moment tensor in source-type space.

tial component, indicative of a larger tectonic release. For METROPOLIS we have data from three stations PAS, CMB and MHC where we can compare the solutions at different frequency bands. Additionally, we are able to compute a solution including two additional stations, MNV and LAC from the LLNL network, increasing the azimuthal coverage from 75° to 123°. Data from MNV and LAC are filtered between 10 to 30 seconds. PAS and CMB have high SNR at both long and short periods whereas MHC has relatively noisy data at long periods for the two horizontal components, but relatively high SNR for the vertical component. At 20 to 50 seconds, we see very little SH energy in the tangential component and essentially none at CMB. The deviatroic part of the solution is very similar for both 1D and 3D MTs; however, the 3D solution has a much higher ISO component, 16% higher than the 1D solution (Fig. 8a). Again, the 3D solution has a higher Mw that is closer to the reported magnitude (Md) in the catalog (Table 5.1). Although the VR improved slightly for all three stations from 1D to 3D (Fig. 5.8b-c), the increase is only a few percent. At 8 to 20 seconds, the ISO component of the 3D solution decreased to 59%, in contrast the ISO component of the 1D solution increased to 81%. The deviatoric part of the solution changed significantly from long period to short period, instead of a reverse sense of motion for both solutions at long periods, at short periods the 1D solution is mostly DS and the 3D solution has a large CLVD component. In terms of waveform fits (Fig. 5.8d-e), overall

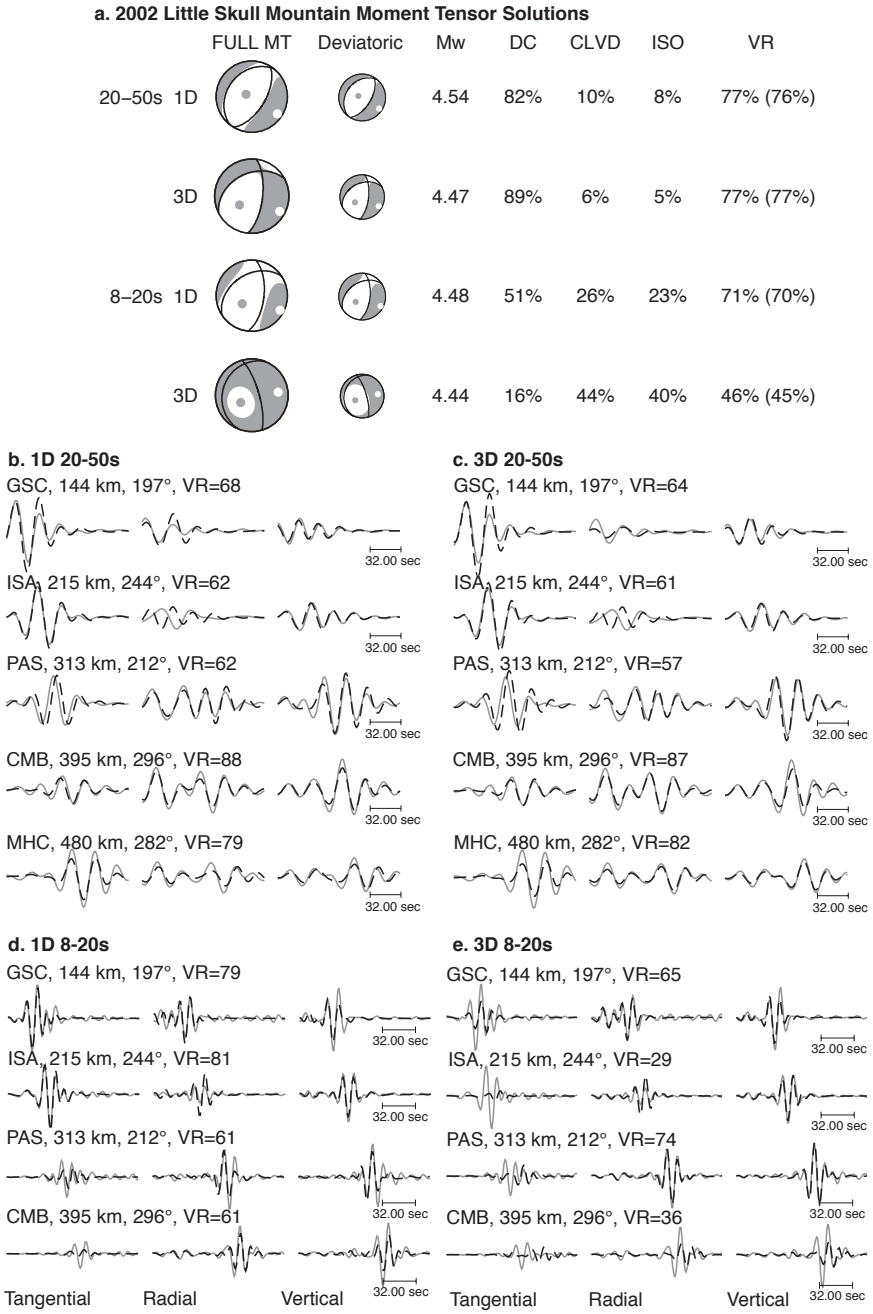

Figure 5.5: 2002 Little Skull earthquake full moment tensor inversion results with 1D and 3D Green's functions and at different frequency bands. (a) Full moment tensor focal mechanism and the deviatroic component of the solution are plotted as well as the moment magnitude (M_w), percent double-couple (DC), percent compensated linear vector dipole (CLVD), percent isotropic (ISO) and variance reduction (VR). VR from deviatoric inversion is in parentheses. (b-e) Data (solid line) and synthetic waveforms (dashed line) plotted from left to the right are the tangential, radial and vertical components.

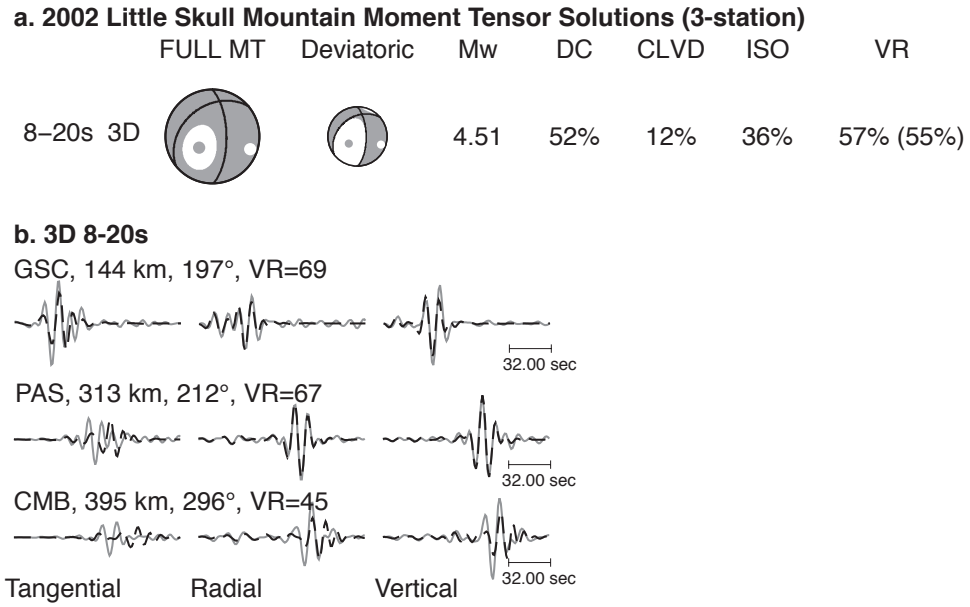

Figure 5.6: 2002 Little Skull earthquake three-station inversion using 8 to 20 second 3D Green's functions. (a) Full moment tensor focal mechanism and the deviatroic component of the solution are plotted as well as the moment magnitude (M_w), percent double-couple (DC), percent compensated linear vector dipole (CLVD), percent isotropic (ISO) and variance reduction (VR). VR from deviatoric inversion is in parentheses. (b) Data (solid line) and synthetic waveforms (dashed line) plotted from left to the right are the tangential, radial and vertical components.

the 1D model is fitting the data better than the 3D model due to significant increase in VR at CMB. On the other hand, the 3D model performs better along the path to MHC. Mw decreased for both solutions from the long period case to short period case, but again the 3D solution has a higher Mw. The best solution is the inversion using data from five stations and filtered between 10 to 50 seconds (Fig. 5.8a). Both 1D and 3D results have high ISO components and similar mechanisms for the off-diagonal components. Mw for the 3D solution is 0.3 magnitude units higher than the 1D solution, and overall the 3D model is fitting a few percent better than the 1D model.

Unlike the other explosions in this study, HOYA has strong Love wave energy across all stations. The data also have high SNR in the frequency band we examined and better station coverage compare to the other explosions. The azimuthal coverage for HOYA is 100° for the five-station inversion, and the best solution including two additional LLNL stations MNV and LAC has an azimuthal coverage of 132°. For solutions from 20 to 50 seconds (Fig. 5.9a-c), the ISO component is around 60% for both velocity models; however the 3D solution

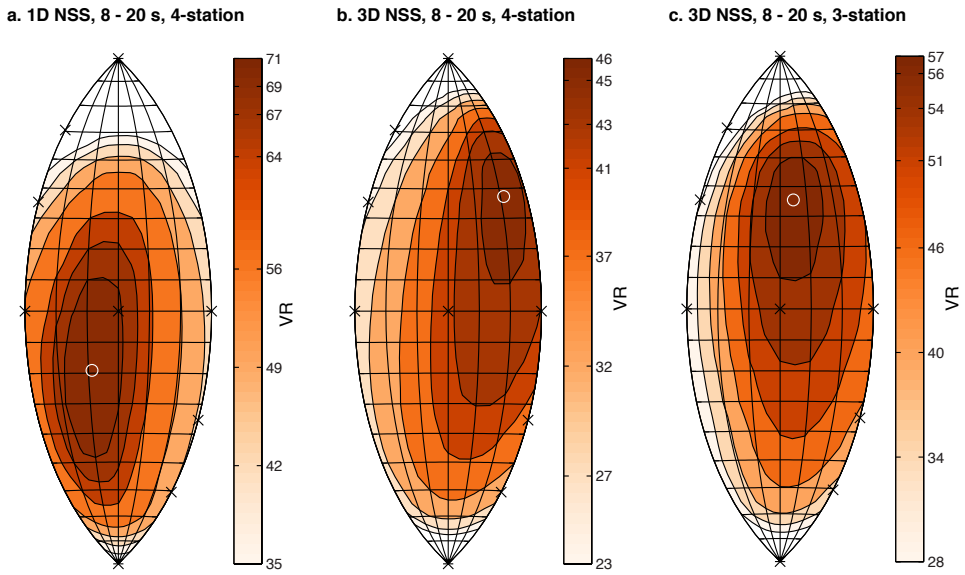

Figure 5.7: 2002 Little Skull Mountain NSS using 8 to 20 second Green's functions for (a) 1D 4-station inversion, (b) 3D 4-station inversion and (c) 3D 3-station inversion. White circles mark the location of best full moment tensor in source-type space.

has a larger DC component and a higher Mw. The non-ISO mechanism is quite different between the two models, the 1D case is a normal mechanism and the 3D case is a vertical DS mechanism. The 3D model fits the data better than the 1D model. As seen in Figure 5.9b-c the amplitudes between the data and synthetics at stations PAS, PFO and BKS are in better agreement when we use a 3D model.

From 8 to 20 seconds (Fig. 5.9a,d-e), the 3D solution has an ISO component of 73% whereas the 1D solution has an ISO component of 54%. The 3D model cannot fit the data well on the tangential components at all stations except for BKS. We can see the waveform fits are significantly better along the path to BKS when using 3D GFs instead of 1D GFs, resulting in higher overall VR for the 3D solution. At short periods the deviatoric part of the solution has a different mechanism compared to the long period solutions. Although the 3D case still consists of a vertical DS mechanism the fault orientation has rotated about 45° towards the southwest. In contrast to the other explosions the M_w is slightly higher when using 1D GFs at short periods. The long period solutions are more consistent with the seven-station inversion because the frequency band used for the best solution is between 10 to 50 seconds. We use inverse variance weighting instead of inverse distance weighting for the seven-station inversion because data from MNV and LAC are filtered between 10 to 30 seconds, resulting in higher amplitudes, while the rest of the stations are filtered between 20 to 50 seconds. For the seven-station inversion, the 3D solution has a higher M_w and ISO

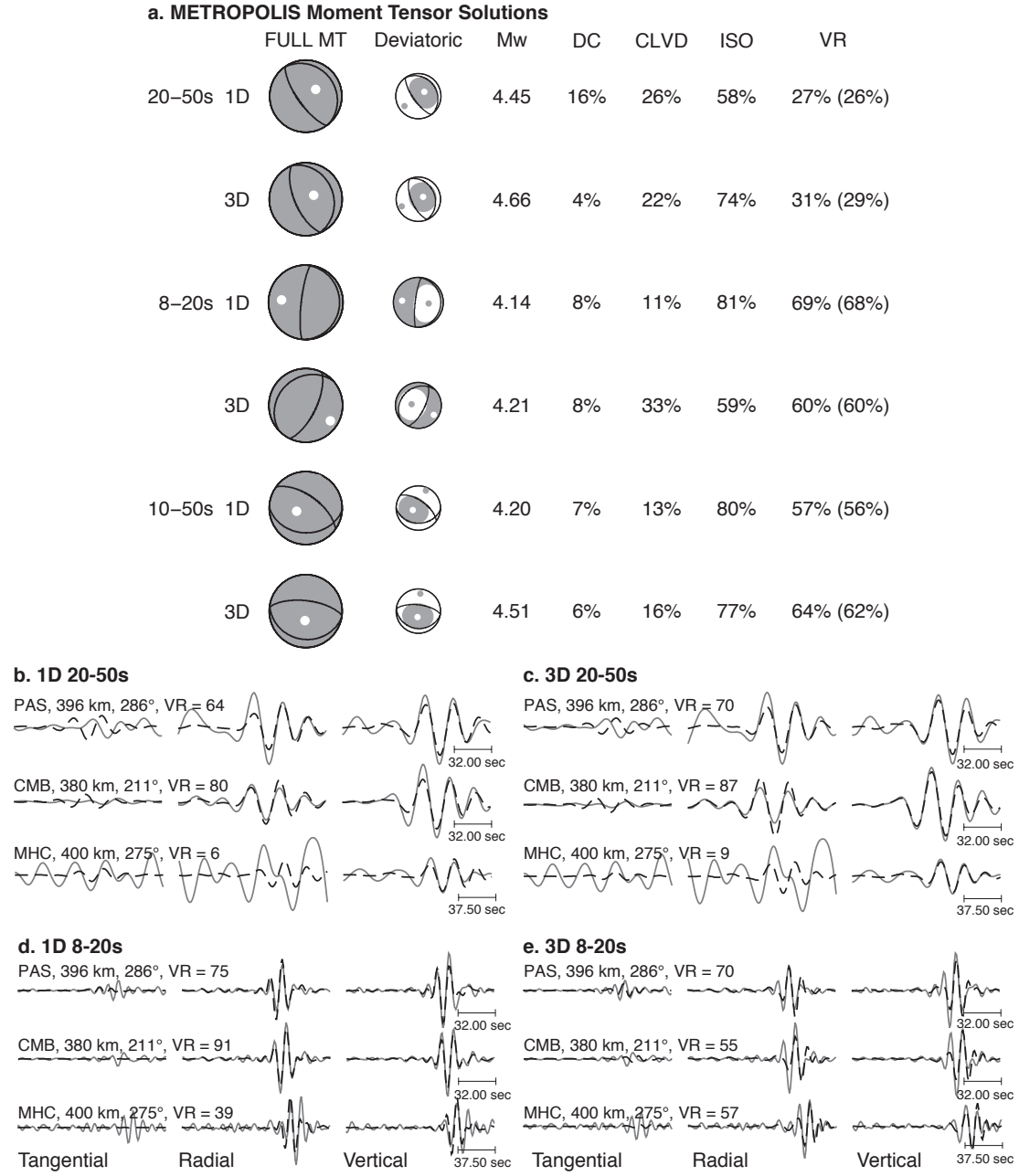

Figure 5.8: METROPOLIS full moment tensor inversion results with 1D and 3D Green's functions and at different frequency bands. (a) Full moment tensor focal mechanism and the deviatroic component of the solution are plotted as well as the moment magnitude (M_w), percent double-couple (DC), percent compensated linear vector dipole (CLVD), percent isotropic (ISO) and variance reduction (VR). VR from deviatoric inversion is in parentheses. (b-e) Data (solid line) and synthetic waveforms (dashed line) plotted from left to the right are the tangential, radial and vertical components.

component, and a vertical DS mechanism instead of a normal mechanism for the deviatoric part of the full MT.

For JUNCTION, we have data from four stations BKS, PAS, PFO and ISA for the comparison at different periods, and there is an additional LLNL station LAC in the five-station inversion. For the five-station inversion, all data from the BDSN and SCSN network stations are filtered between 10 to 50 seconds and LAC is filtered between 10 to 30 seconds. Comparing the results at 20 to 50 seconds (Fig. 5.10a), full MT solutions using either model have excellent waveform fits; the 3D solution has a VR of 95% and the 1D model has a VR of 83%. VR increases for all stations using 3D GFs but the biggest improvements are along the paths to BKS and PFO (Fig. 5.10b-c). Similar to HOYA, the amplitudes between data and synthetics on the radial and vertical components agree well when 3D GFs are used but not as well on the tangential component for BKS and PFO. Both solutions are predominantly ISO but the 3D solution has an ISO component 17% higher than the 1D solution. Mw from the 3D solution is also higher than the 1D case. The deviatoric component of the solutions have different fault orientations and sense of motion between the 1D and 3D case; the 1D solution consists of a normal mechanism and the 3D solution consists of a CLVD mechanism with the major vector dipole in tension (+CLVD).

Comparing the solutions at periods between 8 and 20 seconds, we see again that the paths to BKS and PFO are well modeled using 3D GFs, which are consistent with the results at long periods. However, the VR decreases for the paths to ISA and PAS when using 3D GFs (Fig 5.10d-e). Different than the results at long period, the 1D solution has a larger ISO component of 75% while the 3D solution has an ISO component of 69%. The non-ISO part of the MT consists of a DS mechanism but with different orientations between 1D and 3D cases. Jackknife resampling of different station combinations shows PAS is a key station in the inversion at short period, the ISO component decreases when we remove PAS, especially for the 1D case where the ISO disappears and the solution is a CLVD mechanism with the major vector dipole in compression (−CLVD). The best solution using data from five stations are mostly ISO but for the 1D case the ISO component is reduced to 56%. In terms of M_w, the 3D solution overestimates the magnitude when we compare it to the reported ML in Springer et al. (2002). The deviatoric part of the solution comprises of a vertical DS mechanism for the 1D case and a +CLVD mechanism for the 3D case. The drop in VR for the 1D solution is due to lower fits at station LAC whereas all other stations have VR above 70%.

5.4.4 Comparison in Source-Type Space

Network Sensitivity Solutions (NSS) utilizing source-type representations proposed by Hudson et al. (1989) and Tape and Tape (2012a) and Tape and Tape (2012b) have been developed and used in previous studies to estimate uncertainties in source inversions (e.g. Ford et al., 2010; Guilhem et al., 2014; Chiang et al., 2014; Nayak and Dreger, 2015). We

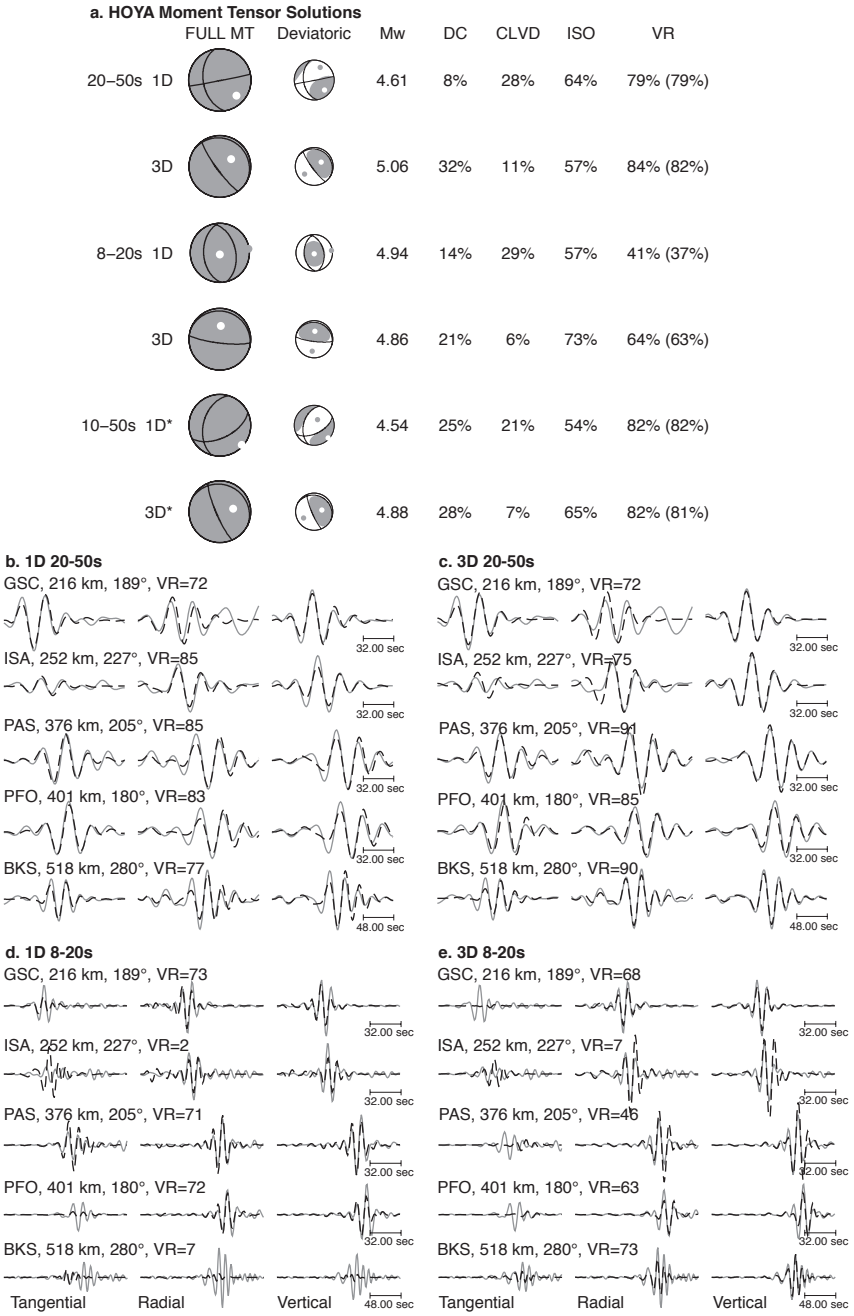

Figure 5.9: HOYA full moment tensor inversion results with 1D and 3D Green's functions and at different frequency bands. (a) Full moment tensor focal mechanism and the deviatroic component of the solution are plotted as well as the moment magnitude (M_w), percent double-couple (DC), percent compensated linear vector dipole (CLVD), percent isotropic (ISO) and variance reduction (VR). VR from deviatoric inversion is in parentheses. (b-e) Data (solid line) and synthetic waveforms (dashed line) plotted from left to the right are the tangential, radial and vertical components.

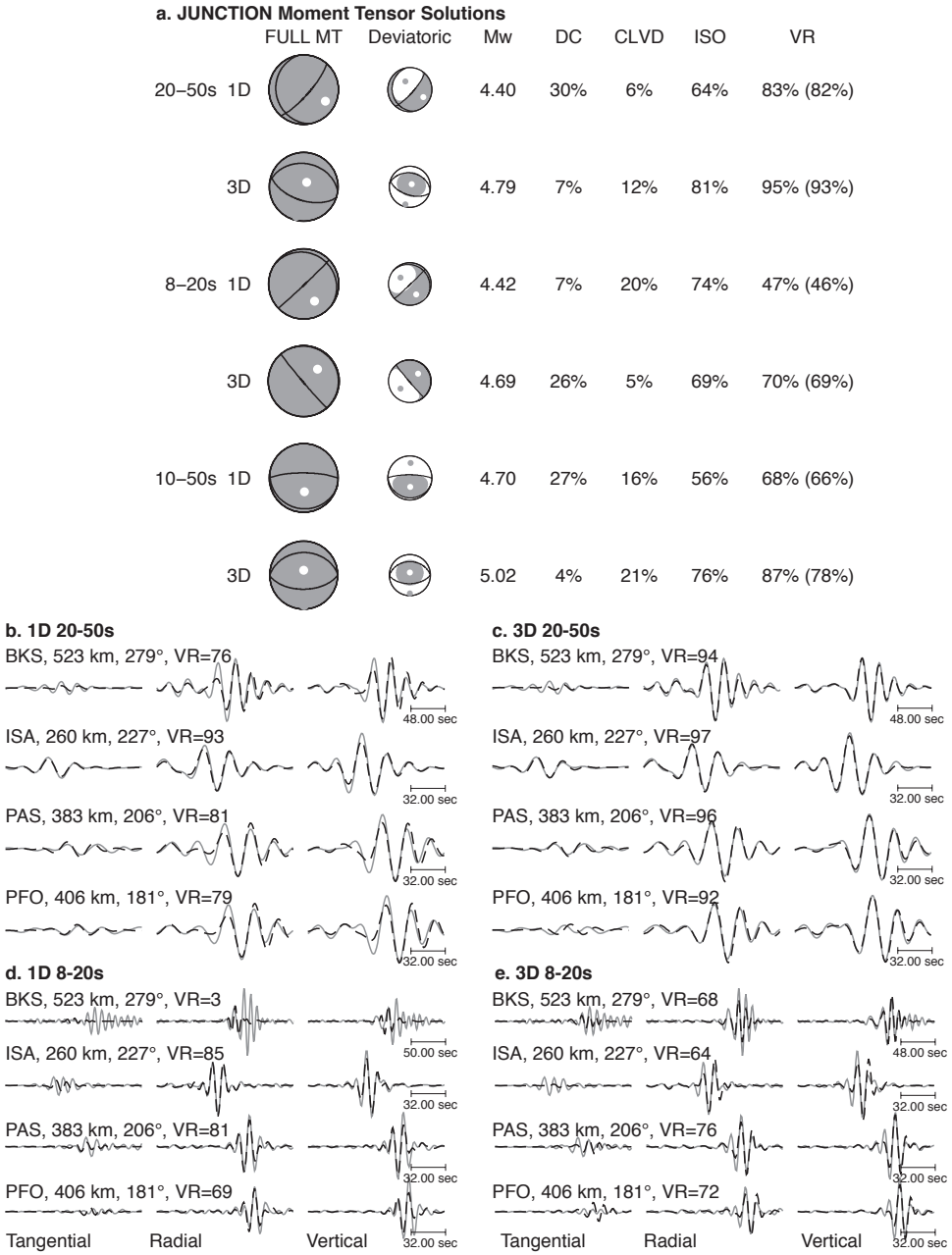

Figure 5.10: JUNCTION full moment tensor inversion results with 1D and 3D Green's functions and at different frequency bands. (a) Full moment tensor focal mechanism and the deviatroic component of the solution are plotted as well as the moment magnitude (M_w), percent double-couple (DC), percent compensated linear vector dipole (CLVD), percent isotropic (ISO) and variance reduction (VR). VR from deviatoric inversion is in parentheses. (b-e) Data (solid line) and synthetic waveforms (dashed line) plotted from left to the right are the tangential, radial and vertical components.

would like to compare the estimated uncertainties in the source-type space between 1D and 3D GFs to see if the 3D model reduces the source-type uncertainties, therefore providing better constraints on source mechanisms and increasing confidence in discrimination. We compute the NSS for Little Skull Mountain, METROPOLIS, HOYA and JUNCTION using the same station configuration and filter parameters in the MT inversion analysis. The results comparing 1D and 3D NSS at two frequency bands are presented in Figure 5.11, where we plotted solutions with normalized VR$\geq$95%. The comparison for the 2002 Little Skull Mountain earthquake shows at long periods (20-50 seconds) the spread of the MT uncertainties are larger using 3D GFs, but at short periods (8-20 seconds) the spread is about the same between the two models. If we look at the distribution of the source-type parameters γ and δ (Fig. 5.12a), we see a wider distribution in the volumetric component (δ) of the MT when inverting using 3D GFs. At higher frequencies, the two NSS populate different areas of the source-type space; the 3D NSS extends into the region of positive volume change while the 1D NSS extends into the region of negative volume change. There are noticeable shifts in the mean of the distributions for both 1D and 3D NSS (Fig. 5.12a), where the distributions at short periods deviate away from a pure DC mechanism. For the explosions, 1D and 3D NSS (Fig. 5.11) at long periods show the spread of the estimated uncertainties associated with source inversion varies between events: the uncertainties for JUNCTION are similar using either 1D or 3D GFs, for HOYA the solutions are better constrained using 3D GFs but the results are opposite for METROPOLIS. At short periods we see little difference between the 1D and 3D NSS, except for HOYA where the solution is very well-constrained using 1D GFs. The distribution of γ and δ for explosions are negative skewed (Fig. 5.12b), meaning they have a long tail in the negative direction, for both 1D and 3D models and at both long and short periods, the exception is the HOYA 1D NSS where γ is positive skewed resulting in a population of solutions near the theoretical explosion/opening crack mechanisms. All explosion NSS have a mean δ around 30° and we do not see a large difference in the mean δ values between 1D and 3D NSS.

5.5 Discussion

Comparisons between 1D and 3D source inversions show differences in source mechanism in both the long period and short period cases. For the 20 to 50 second case, the 1D and 3D solutions for the 2002 Little Skull Mountain earthquake show minimal difference in source mechanism and magnitude. In contrast, the explosions show an increase in magnitude and waveform fits from 1D to 3D inversions. The off-diagonal components are not well-constrained and vary depending on the frequency band and velocity model used. Contrary to Hingee et al. (2011) and Covellone and Savage (2012), where MT solutions were compared from 40 to 200 seconds and 25 to 125 seconds, respectively, in general we see a reduction in waveform fits for the 3D inversions at relatively short periods (8 to 20 seconds) and for the two earthquakes we see an increase in non-DC components, suggesting finer de-

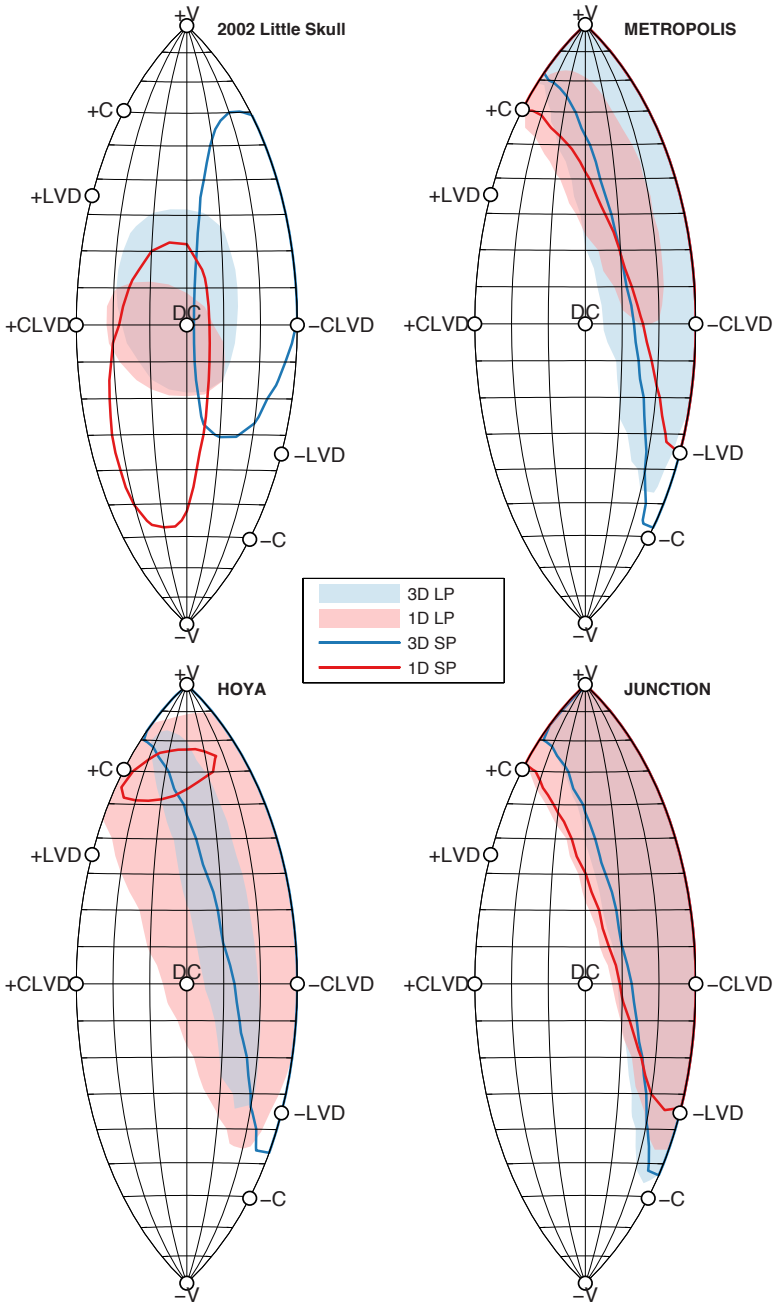

Figure 5.11: Figure 11. Comparison of Network Sensitivity Solution (NSS) of four different events: 2002 Little Skull earthquake, METROPOLIS, HOYA and JUNCTION. The shaded regions and contour lines show the populations of solutions with normalized VR≥95% for long period and short period waveform inversions, respectively. The blue and pink colors are solutions computed using 3D and 1D Green's functions, respectively.

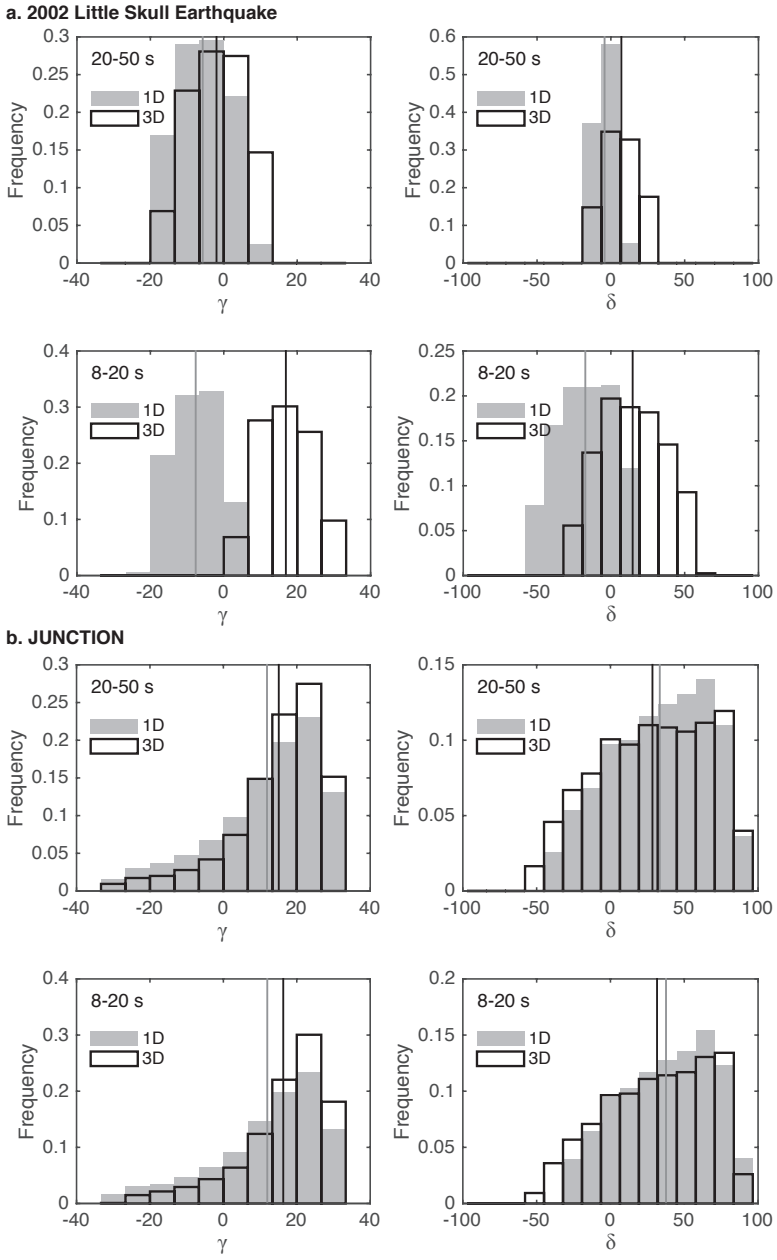

Figure 5.12: Comparisons of source-type parameters γ and δ for two events (a) 2002 Little Skull Mountain earthquake and (b) NTS explosion JUNCTION. Histograms show γ and δ from waveform inversions at two frequency bands, the gray bars represent the use of 1D Green's functions, the white bars represent the use of 3D Green's functions, and the gray and black lines are the mean values from 1D and 3D inversions, respectively.

tails of the Earth's structure may not be well-represented by the 3D model. The exceptions are the paths to BKS and MHC, particularly BKS, where we see significant improvements in waveform fits when 3D GFs are used in the short period inversions. Paths crossing the extensional regimens and low velocity sediments (Fig. 5.13a) are better represented by the 3D model, where stations BKS and MHC are situated on top of the low velocity zone (Fig. 5.13b). Based on the four events analyzed in this study, the long period time domain MT inversion results in higher waveform fits when 3D GFs are applied, however we do not see a significant reduction in uncertainties associated with the MT using synthetics derived from the 3D model. JUNCTION has little difference in source uncertainties between the 1D and 3D case, Little Skull Mountain and METROPOLIS show higher uncertainties for the 3D case whereas HOYA shows lower uncertainties for the 3D case. A larger sample size is required to make more useful interpretations about the use of 3D models in estimating MT source uncertainties.

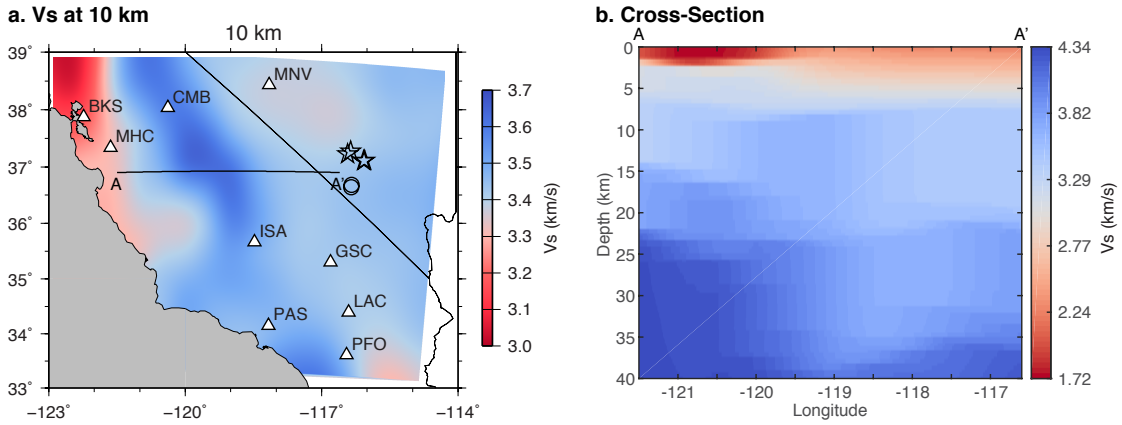

Figure 5.13: (a) Vs at 10 km depth where surface waves are most sensitive to the structure at these period ranges. (b) A cross-sectional view of crustal and upper mantle velocities across A-A'.

Moschetti et al. (2010) noted the surface wave model has larger uncertainties in shear wave speeds in extensional regions across the western US, near the Moho (lower crust) and the shallowest parts of the crust. There is a significant trade-off between crustal thickness and shear wave speed resulting in an increase in shear wave uncertainties around the Moho (between 35 to 45 km depth). In our 3D short period inversions, Rayleigh waves are fitting better than the Love waves. The 3D model used was determined using dispersion data from Rayleigh wave group and phase velocities and Love wave phase velocities, Love wave group velocities are not included due to large uncertainties. Also, the Love wave dispersion maps are in period bands of 8 to 32 seconds whereas the Rayleigh wave dispersion maps are in period bands of 6 to 40 seconds. Therefore in addition to a priori constraints on sediment

and crustal thicknesses (Laske and Masters, 1997; Gilbert and Fouch, 2007) the details of the 3D model were constrained mostly by short period Rayleigh wave data. In comparison, Hingee et al. (2011) used a 3D radially anisotropic model constructed from full waveform tomography. The full waveform model (Fichtner et al., 179; Fichtner et al., 290) is derived from a large variety of observations including both surface waves and body waves. They also implemented a realistic 3D Q model by Abdulah (2007). Covellone and Savage (2012) also used a 3D model (Kustowski et al., 2008) computed from a combination of data sets that included surface wave phase velocity measurements, long period waveforms and body wave travel times. This suggests tomography models derived from full waveform modeling are preferred for short period inversions.

Since our results indicate the use of 3D GFs at short periods has limited benefit for the particular 3D model that was employed, a more attractive option to evaluate 3D models than the costly 3D simulations may be using path-averaged 1D velocity models derived from the 3D model. We compute MTs for Little Skull Mountain, HOYA and JUNCTION using 1D averaged velocity models for each source-receiver path. In general, the averaged structures have a Moho ranging from 30 to 37 km and a very thin low velocity layer (<1 km thick) when compared to the 1D Song et al. (1996). Here we present results for Little Skull Mountain (Fig. 5.14) and HOYA (Fig. 5.15). Overall the MT solutions from 20 to 50 seconds (Fig. 5.14a-b and Fig. 5.15a-b) are similar to previous 1D and 3D MTs, the differences are in the short period inversions. For JUNCTION the results are similar to the 3D inversion except the path to BKS cannot be modeled by the averaged 1D structure, and the solution has a lower ISO of 52%. For Little Skull Mountain, the short period inversion with averaged 1D models have better fits to the data at ISA and CMB, however the resulting mechanism is an incorrect oblique strike-slip earthquake (Fig. 5.14a). The overall lower goodness of fit with averaged 1D MTs and 3D MT suggest paths from Little Skull Mountain to the stations need further refinement. For HOYA, the averaged 3D structure is actually a better representation for the paths to GSC, ISA and PFO, the fits to the data at these stations are higher compare to the 3D solution due to better agreement in the Love waves; whereas again the paths to BKS cannot be modeled by the path-averaged 1D model. 1D and 3D comparisons indicate that, in many cases, well-calibrated average 1D representations of the Earth structure may be a more attractive option at periods as short as 8 seconds, but 3D models do need to be considered as shown by the modeling results for the path to BKS.

5.6 Conclusion

We applied source-receiver reciprocity to compute 3D GFs using the FD method. Using the full waveform MT inversion method (Minson and Dreger, 2008) we analyze earthquakes and explosions at NTS using 1D and 3D Earth models. Other than the computation of the GFs, we applied identical data processing procedures to the 1D and 3D waveform inversions

and use the same station configuration to allow for direct comparisons between the source properties and associated uncertainties of the two models and evaluate the results in different frequency bands. Our results at low frequencies show good agreement for the focal mechanisms between the two models and slight improvement in waveform fits when using the 3D model. At high frequencies the advantage of the 3D model is limited, mainly due to poor agreement between Love wave data and synthetics, and for the two earthquakes we see an increase in non-DC components in our full 3D MT results; however we do see significant improvements in the 3D inversion along the paths to BKS and MHC and the reduction in variance is especially prominent at high frequencies. In addition, we see better agreement between Mw and the reported catalog magnitudes when 3D models are applied in the inversion. We do not see a systematic reduction in uncertainties associated with the MT when 3D GFs are applied, in most cases the uncertainties are the same between the two models at short periods but vary from event to event at long periods. The 3D model that was used tends to add a false isotropic component to MT solutions of earthquakes. While this is a negative result from a source-type discrimination perspective it is important to recognize that the improvement in fit afforded by the isotropic component is not statistically significant. Using 3D velocity models for source inversion is often cited as a means to improve results however this analysis demonstrates that this may not always be the case, and even if calibrated 3D models are employed careful analysis of uncertainty and solution sensitivity are needed before non-DC components of MTs of earthquakes can be interpreted. The results also show for the explosions that there is no difference in the ability to discriminate the explosions from earthquakes, which is a positive result, although reduced uncertainty in the source-type goodness of fit space using the 3D GFs would be preferred. The results however do show that the minor non-isotropic components of explosions is highly variable with respect to both the velocity model and the passband. This means that it will be difficult to interpret such results for mechanism of non-isotropic radiation in explosions from MT inversions.

Our results indicate that the surface wave derived 3D model for the Western U.S. for seismic MT estimation still needs further refinement along the paths we examined (except perhaps BKS/MHC) to model wave propagation at high frequencies, and instead of the more costly 3D simulation using path-averaged 1D models for short period inversion is a more practical option in many cases. A 3D model by Shen et al. (2013) uses additional constraints from receiver functions should be evaluated and compared to the MT inversion results using the Moschetti et al. (2010) model in future work. In this study we have established a procedure to compare and evaluate 1D and 3D source inversions, when models with better crustal resolutions become available we can begin to explore depth sensitivity for both explosions and shallow earthquakes. It is likely that when trying to improve capabilities for other regions of the world that multiple 3D velocity models will need to be tested, as well as perturbations to those models in order to evaluate the stability of source solutions obtained with 3D velocity models, much in the same way that it is necessary to do so with 1D models.

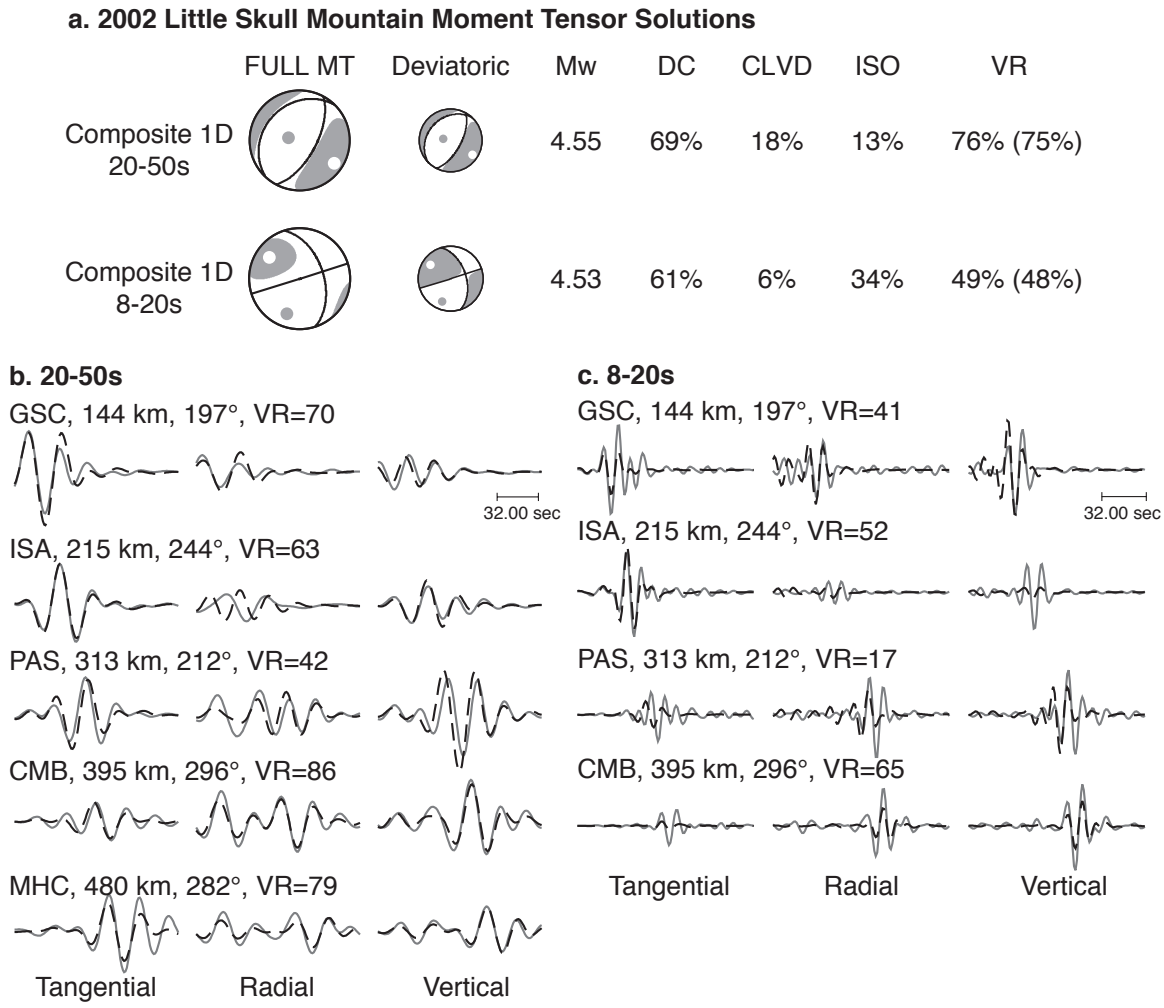

Figure 5.14: 2002 Little Skull Mountain full moment tensor inversion results with path averaged 1D Green's functions at different frequency bands. (a) Full moment tensor focal mechanism and the deviatroic component of the solution are plotted as well as the moment magnitude (M_w), percent double-couple (DC), percent compensated linear vector dipole (CLVD), percent isotropic (ISO) and variance reduction (VR). VR from deviatoric inversion is in parentheses. (b-c) Data (solid line) and synthetic waveforms (dashed line) plotted from left to the right are the tangential, radial and vertical components.

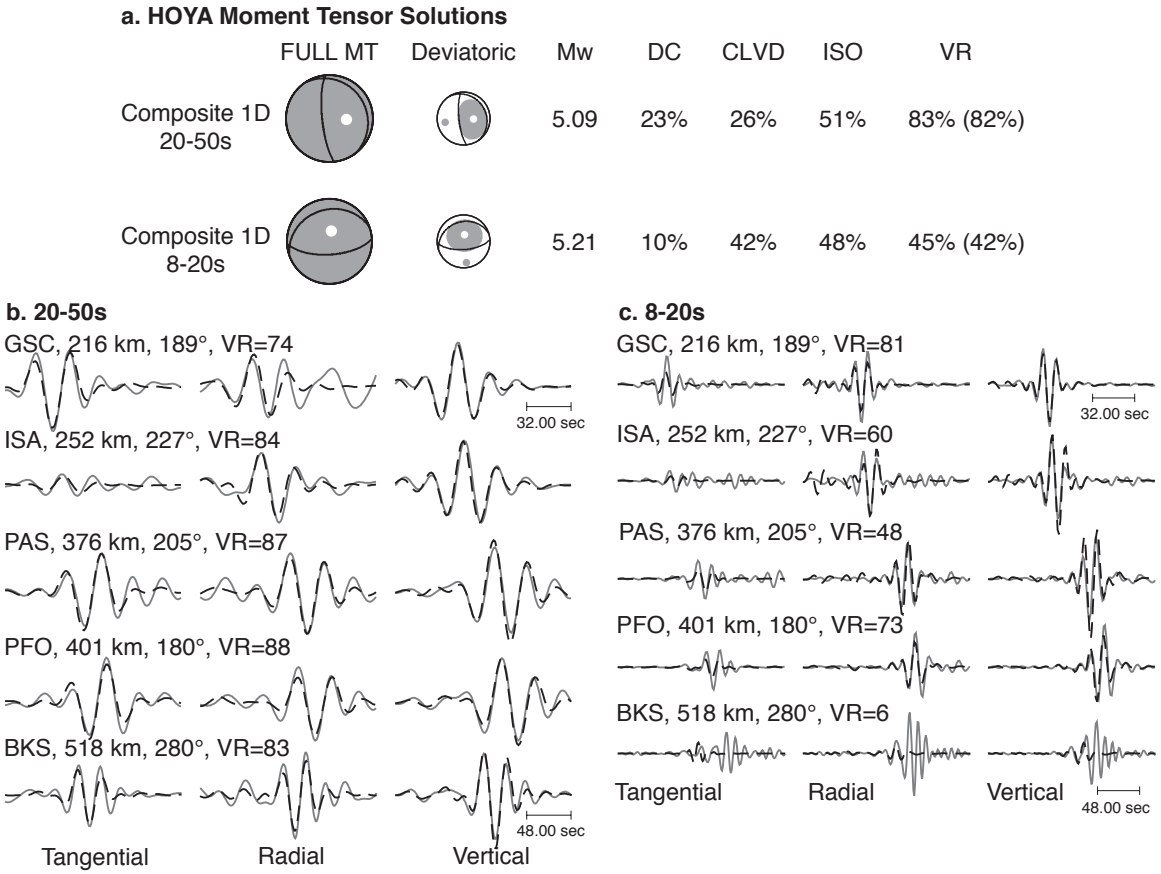

Figure 5.15: HOYA full moment tensor inversion results with path averaged 1D Green's functions at different frequency bands. (a) Full moment tensor focal mechanism and the deviatroic component of the solution are plotted as well as the moment magnitude (M_w), percent double-couple (DC), percent compensated linear vector dipole (CLVD), percent isotropic (ISO) and variance reduction (VR). VR from deviatoric inversion is in parentheses. (b-c) Data (solid line) and synthetic waveforms (dashed line) plotted from left to the right are the tangential, radial and vertical components.

Chapter 6

Conclusion

The regional distance, long period complete waveform moment tensor inversion approach is invaluable for nuclear event discrimination. The method is capable of discriminating explosions from other seismic sources under sparse monitoring situations, at shallow source depths and for complex sources. Although there are several theories about the generation of shear waves in underground nuclear explosions the process remains poorly understood (e.g. Massé, 1981), but this research demonstrates despite the lack of understanding of the complex source processes the isotropic components can still be extracted from long period regional waveforms and provide a strong discrimination capability. In addition to the seismic discrimination application, the techniques developed in this study can be applied to other natural and manmade events to obtain reliable focal mechanisms and assess their uncertainties, which are important for fault characterization, tectonics, seismic hazard, and in-situ stress studies.

In Chapter 2 we perform seismic moment tensor inversions for the 1988 Soviet JVE test and two Chinese Lop Nor nuclear tests. These cases have sparse monitoring conditions as well as uncertainty in velocity structure. In each case we have shown that the use of long-period waveform data comprised mostly of regional surface waves result in solutions with large isotropic components that are consistent with solutions for other studied nuclear tests (Ford et al., 2009a; Ford et al., 2009b; Ford et al., 2010). The inclusion of regional and/or teleseismic P-wave first motion polarities constrain the moment tensor derived source-type, providing good separation from earthquakes and other deviatoric source types. Importantly there is separation with cavity collapse source-types, which have caused difficulties with other discriminants (Walter et al., 2007). Observations of possible Rayleigh wave reversals for the 8 June 1996 Lop Nor test suggest other source processes such as shock driven block faulting or tensile damage (Patton and Taylor, 2008) may be involved. We carried out synthetic tests to evaluate the method's capabilities for different levels of tectonic release and source medium damage. These tests show that the combination of long-period regional waveform data and P wave first motion polarities is able to resolve the anomalous volumetric nature of compound explosion tensile-damage/block-faulting events.

In Chapter 3 we are able to extract the isotropic component of low-magnitude, shallow chemical explosions where free-surface effects are prominent. Although the source-type uncertainty analysis shows using waveform data alone cannot uniquely characterize the events as explosive, the combined waveform and first motion method enables the unique discrimination of these events. Incorporating the two data sets is particularly useful in constraining the isotropic component of explosions, and the method not only applies to large events, but also to small magnitude, very shallow explosions that are effectively at the free surface.

Although the moment tensor method is capable of event discrimination, yield estimation using the recovered seismic moment from moment tensor inversion remains challenging. But using the combined waveform and first motion data Network Sensitivity Solution (NSS) analysis we can begin to quantify the range of errors in the estimated yield. Pure explosion synthetic tests suggest source inversions using Green's functions for deeper depths reduce the bias in moment due to free surface effects. We do find that the estimated yields for these small chemical explosions are consistent with an extrapolation of a moment/yield empirical relationship derived for much larger nuclear explosions (Stevens and Murphy, 2001). However we cannot draw definite conclusions using the results from the chemical explosions due to not only free-surface effects, but uncertainties associated with imperfect knowledge of the Earth structure, unaccounted non-isotropic radiation due to the mass movement of the quarry face (Goforth and Bonner, 1995; Bonner et al., 1996) and differences in seismic coupling between different types of explosives (Murphy, 1996).

In Chapter 4 we show synthetically that using 1D velocity models to compute Green's functions is a robust assumption in moment tensor inversions at periods down to 10 seconds. We demonstrate in our synthetic study that earthquake mechanism and source depth can be recovered using 1D velocity models, and the non-double-couple components in the full moment tensors are not statistically significant with the additional degree of freedom as determined by the F-test (e.g. Menke, 2012). For the explosion and composite sources, although we do not see an increase in the double-couple components, the recovered solution is predominantly CLVD due to the theoretical ISO-CLVD trade-off resulting from the ambiguity in surface wave radiation for an explosion and a vertically oriented CLVD in compression. However, the NSS exhibits a typical explosion-like signature in the source-type space and the trade-off can be eliminated with additional constraints from P wave first motion polarities. We also demonstrate how the method's ability to accurately predict wave propagation degrades as we added heterogeneities to the smooth model by applying large-scale random velocity perturbations. When an explosion case is considered there is an increase in the "tectonic" release; however, we also see a reduction in the fit to the data and larger uncertainties in the source-type space, indicative of a poor solution. Although unmodeled Earth structure results in an increase in non-double-couple components in earthquakes and non-isotropic components in explosions, we show that these components can be reduced with path-specific calibrations to the 1D model, either by forward modeling of broadband waveforms or by

taking the average 1D model for each source-receiver path from a 3D velocity model.

The 1D model assumption is advantageous in terms of computational cost and produces stable solutions in the low frequency band, it can however lead to bias in moment tensor results in regions of large lateral heterogeneity and at high frequencies (e.g. Liu et al., 2004; Covellone and Savage, 2012). The ability to model higher frequency waveforms becomes an integral part because for small magnitude seismic events and low-yield explosions the long period signals at regional distances are often below the background noise level, while the high frequency waveforms have better signal-to-noise ratios. But to utilize the high frequency data requires the use of 3D velocity models to account for heterogeneities in the structure.

Therefore in Chapter 5 we investigate source processes of earthquakes and explosions at the Nevada Test Site using 1D and 3D Earth models, and evaluate the solutions at different frequency bands. We compute 3D velocity model Green's functions with the finite-difference approach by invoking source-receiver reciprocity to reduce computation cost. Our results show good agreement between the 1D and 3D solutions from 20 to 50 seconds where there is slight improvement in waveform fits when 3D Green's functions are considered. From 8 to 20 seconds the advantage of the smooth 3D model is limited though we do see significant improvements along the paths crossing the Basin and Range and into the low velocity sediments of the Central Valley of California (BKS/MHC). Along these paths the reduction in variance between observations and predictions is prominent at high frequencies. While we see good agreement between 1D and 3D moment tensor solutions we do not see a systematic reduction in the associated uncertainties in source-type space when 3D Green's functions are considered. In addition, solutions computed using path-averaged 1D models are comparable to solutions using 3D Green's functions, suggesting that the use of path-specific 1D models derived from the 3D model is a more attractive alternative compared to the more costly 3D simulations. Our results indicate that the finer details of the Moschetti et al. (2010) surface wave tomography needs further refinement along most of the paths we examined and comparisons with other studies show that velocity models derived from full waveform tomography are preferred for source inversions at high frequencies.

This dissertation demonstrates the utility of complete waveform moment tensor inversion for nuclear event discrimination. Regional waveform inversion with additional constraints from P wave first motion polarities can be used to discriminate explosions from earthquakes and reduce the estimated uncertainties in situations where free-surface vanishing traction, complexities in explosion source processes, sparse station coverage, and imperfect representation of Earth structure can introduce biases in the recovered solution. However, challenges remain in estimating explosive yield and modeling high frequency waveforms for the monitoring of low-yield explosions. Future work on expanding the dataset to include additional observations from small chemical explosions with announced yields can help establish more suitable magnitude-yield relationships for small events; and comparison of multiple 3D veloc-

ity models is necessary to evaluate solution stability at higher frequencies. The established procedure to compute 3D Green's functions and techniques to evaluate solution stability will allow us to explore different velocity models and source depth sensitivity for both explosions and shallow seismicity at multiple frequency bands, background noise levels and station geometries. Future work should also investigate the application of the GridMT approach (Kawakatsu, 1998) at monitoring targeted regions to locate and characterize local seismicity and explosions. Successful applications to offshore earthquakes in the Mendocino Triple Junction (Guilhem and Dreger, 2011), the 2011 Tohoku-Oki megathrust (Guilhem et al., 2013), and small magnitude swarms associated with the collapse of a salt dome formation in Louisiana (Nayak and Dreger, 2014) demonstrate the inversion can be easily automated for monitoring purposes. The nature of GridMT makes it particularly amenable for implementation of 3D velocity models for Green's functions, and it offers antonymous monitoring capability including detection, location, source estimation, and source-type discrimination for targeted regions and potential clandestine monitoring.

Bibliography

Aagaard, B. T., Brocher, T. M., Dolenc, D., Dreger, D., Graves, R. W., Harmsen, S., Hartzell, S., Larsen, S., and Zoback, M. L. (2008). "Ground-Motion Modeling of the 1906 San Francisco Earthquake, Part I: Validation Using the 1989 Loma Prieta Earthquake". In: *Bulletin of the Seismological Society of America* 98.2, pp. 989–1011. DOI: 10.1785/0120060409.

Aagaard, B. T., Graves, R. W., Rodgers, A., Brocher, T. M., Simpson, R. W., Dreger, D., Petersson, N. A., Larsen, S. C., Ma, S., and Jachens, R. C. (2010). "Ground-Motion Modeling of Hayward Fault Scenario Earthquakes, Part II: Simulation of Long-Period and Broadband Ground Motions". In: *Bulletin of the Seismological Society of America* 100.6, pp. 2945–2977. DOI: 10.1785/0120090379.

Abdulah, A. (2007). "Seismic body wave attenuation tomography beneath the Seismic body wave attenuation tomography beneath the Australasian region". PhD thesis. The Australian National University.

Aki, K. and Richards, P. G. (2002). *Quantitative Seismology*. Ed. by Ellis, J. Sausalito, California: University Science Books; Second edition.

Appelo, D. and Petersson, N. A. (2009). "Communications in Computational Physics". In: *A Stable Finite Difference Method for the Elastic Wave Equation on Complex Geometries with Free Surfaces* 5, pp. 84–107.

Baig, A. and Urbancic, T. (2010). "Microseismic moment tensors: A path to understanding frac growth". In: *The Leading Edge* 29.3, pp. 320–324. DOI: 10.1190/1.3353729.

Baise, L. G., Dreger, D. S., and Glaser, S. D. (2003). "The Effect of Shallow San Francisco Bay Sediments on Waveforms Recorded during the MW 4.6 Bolinas, California, Earthquake". In: *Bulletin of the Seismological Society of America* 93.1, pp. 465–479. DOI: 10.1785/0120010213.

Barker, T., McLaughlin, K. L., Stevens, J. L., and Day, S. M. (1993). *Numerical models of quarry blast sources: effects of the bench*. S-CUBED Report SSS-TR-93–13915. Phillips Laboratory.

Battis, J. C. and Cipar, J. J. (1991). *Seismic recordings in the Northeastern United States of the Shagan River Nuclear Test of 14 September 1988*. Tech. rep. PL-TR-91-2001. Geophysics Directorate of Philips Laboratory, Air Force Systems Command.

Bensen, G. D., Ritzwoller, M. H., and Yang, Y. (2009). "A 3-D shear velocity model of the crust and uppermost mantle beneath the United States from ambient seismic noise".

In: *Geophysical Journal International* 177.3, pp. 1177–1196. DOI: 10.1111/j.1365-246X.2009.04125.x.

Ben-Zion, Y. and Ampuero, J.-P. (2009). "Seismic radiation from regions sustaining material damage". In: *Geophysical Journal International* 178.3, pp. 1351–1356.

Bhattacharyya, J., Sheehan, A. F., Tiampo, K., and Rundle, J. (1999). "Using a genetic algorithm to model broadband regional waveforms for crustal structure in the western United States". In: *Bulletin of the Seismological Society of America* 89.1, pp. 202–214.

Bonner, J. L., Herrin, E. T., and Goforth, T. T. (1996). "Azimuthal Variation of Rg Energy From Quarry Blasts in Central Texas". In: *Seismological Research Letters* 67.4, pp. 43–56. DOI: 10.1785/gssrl.67.4.43.

Bowers, D. (1997). "The October 30, 1994, seismic disturbance in South Africa: Earthquake or large rock burst?" In: *Journal of Geophysical Research: Solid Earth* 102.B5, pp. 9843–9857. DOI: 10.1029/97JB00509.

Bowers, D. and Hudson, J. A. (1999). "Defining the scalar moment of a seismic source with a general moment tensor". In: *Bulletin of the Seismological Society of America* 89.5, pp. 1390–1394.

Bowers, D. and Walter, W. R. (2002). "Discriminating between large mine collapses and explosions using teleseismic P waves". In: *Pure and Applied Geophysics* 159.4, pp. 803–830. DOI: 10.1029/97JB00509.

Boyd, O., Dreger, D., Lai, V., and Gritto, R. (2015). "A Systematic Analysis of Seismic Moment Tensor at The Geysers Geothermal Field, California". Accepted for publication by the Bulletin of the Seismological Society of America.

Brocher, T. M. (2005). "Empirical Relations between Elastic Wavespeeds and Density in the Earth's Crust". In: *Bulletin of the Seismological Society of America* 95.6, pp. 2081–2092. DOI: 10.1785/0120050077.

Burger, R. W., Lay, T., and Burdick, L. J. (1987). "Average Q and yield estimates from the Pahute Mesa test site". In: *Bulletin of the Seismological Society of America* 77.4, pp. 1274–1294.

Burger, R. W., Lay, T., Wallace, T. C., and Burdick, L. J. (1986). "Evidence of tectonic release in long-period S waves from underground nuclear explosions at the Novaya Zemlya test sites". In: *Bulletin of the Seismological Society of America* 76.3, pp. 733–755.

Chiang, A., Dreger, D. S., Ford, S. R., and Walter, W. R. (2014). "Source Characterization of Underground Explosions from Combined Regional Moment Tensor and First-Motion Analysis". In: *Bulletin of the Seismological Society of America* 104.4, pp. 1587–1600.

Covellone, B. M. and Savage, B. (2012). "A Quantitative Comparison between 1D and 3D Source Inversion Methodologies: Application to the Middle East". In: *Bulletin of the Seismological Society of America* 102.5, pp. 2189–2199. DOI: 10.1785/0120110278.

Dahlen, F. A. and Tromp, J. (1998). *Theoretical Global Seismology*. Princeton University Press.

Day, S. M., Cherry, J. T., Rimer, N., and Stevens, J. L. (1987). "Nonlinear model of tectonic release from underground explosions". In: *Bulletin of the Seismological Society of America* 77.3, pp. 996–1016.

Dreger, D. S. (2003). "85.11 TDMT_INV: Time domain seismic moment tensor INVersion". In: *International Handbook of Earthquake and Engineering Seismology*. Ed. by Lee, W. H., Kanamori, H., Jennings, P. C., and Kisslinger, C. Vol. 81. International Geophysics Part B. ACADEMIC PRESS, p. 1627.

Dreger, D. S., Ford, S. R., and Walter, W. R. (2008). "Source Analysis of the Crandall Canyon, Utah, Mine Collapse". In: *Science* 321.5886, p. 217.

Dreger, D. S. and Helmberger, D. V. (1990). "Broadband modeling of local earthquakes". In: *Bulletin of the Seismological Society of America* 80.5, pp. 1162–1179.

Dreger, D. S. and Helmberger, D. V. (1993). "Determination of source parameters at regional distances with three-component sparse network data". In: *Journal of Geophysical Research: Solid Earth* 98.B5, pp. 8107–8125. DOI: 10.1029/93JB00023.

Dreger, D. and Woods, B. (2002). "Regional distance seismic moment tensors of nuclear explosions". In: *Tectonophysics* 356.1–3. Seismic Source Mechanism through Moment Tensors, pp. 139–156. DOI: http://dx.doi.org/10.1016/S0040-1951(02)00381-5.

Dziewonski, A. M., Chou, T.-A., and Woodhouse, J. H. (1981). "Determination of earthquake source parameters from waveform data for studies of global and regional seismicity". In: *Journal of Geophysical Research: Solid Earth* 86.B4, pp. 2825–2852. DOI: 10.1029/JB086iB04p02825.

Dziewonski, A. and Anderson, D. (1981). "Preliminary reference Earth model". In: *Physics of the Earth and Planetary Interiors* 25.297-356.

Eisner, L. and Clayton, R. W. (2001). "A Reciprocity Method for Multiple-Source Simulations". In: *Bulletin of the Seismological Society of America* 91.3, pp. 553–560. DOI: 10.1785/0120000222.

Ekström, G. and Nettles, M. (1997). "Calibration of the HGLP seismograph network and centroid-moment tensor analysis of significant earthquakes of 1976". In: *Physics of the Earth and Planetary Interiors* 101.3–4, pp. 219–243. DOI: http://dx.doi.org/10.1016/S0031-9201(97)00002-2.

Ekström, G. and Richards, P. G. (1994). "Empirical Measurements of Tectonic Moment Release In Nuclear Explosions From Teleseismic Surface Waves and Body Waves". In: *Geophysical Journal International* 117.1, pp. 120–140.

Ellsworth, W. L. (2013). "Injection-Induced Earthquakes". In: *Science* 341.6142. DOI: 10.1126/science.1225942.

Fichtner, A., Kennett, B., Igel, H., and Bunge, H.-P. (179). "Full seismic waveform tomography for upper-mantle structure in the Australasian waveform tomography for upper-mantle structure in the Australasian region using adjoint methods". In: *Geophysical Journal International* 1703-1725.

Fichtner, A., Kennett, B., Igel, H., and Bunge, H.-P. (290). "Full waveform tomography for radially anisotropic structure: new insight into present and past states of the Australasian upper mantle". In: *Earth and Planetary Science Letters* 270-280.

Ford, S. R., Dreger, D. S., and Walter, W. R. (2008). "Source Characterization of the 6 August 2007 Crandall Canyon Mine Seismic Event in Central Utah". In: *Seismological Research Letters* 79.5, pp. 637–644.

Ford, S. R., Walter, W. R., and Dreger, D. S. (2012). "Event Discrimination using Regional Moment Tensors with Teleseismic-P Constraints". In: *Bulletin of the Seismological Society of America* 102.2, pp. 867–872.

Ford, S. R. (2008). "Isotropic Sources and Attenuation Structure: Isotropic Sources and Attenuation Structure: Nuclear Tests, Mine Collapses, and Q". PhD thesis. University of California, Berkeley.

Ford, S. R., Dreger, D. S., and Walter, W. R. (2009a). "Identifying isotropic events using a regional moment tensor inversion". In: *Journal of Geophysical Research: Solid Earth* 114.B1. B01306.

Ford, S. R., Dreger, D. S., and Walter, W. R. (2009b). "Source analysis of the Memorial Day explosion, Kimchaek, North Korea". In: *Geophysical Research Letters* 36.21. L21304.

Ford, S. R., Dreger, D. S., and Walter, W. R. (2010). "Network Sensitivity Solutions for Regional Moment-Tensor Inversions". In: *Bulletin of the Seismological Society of America* 100.5A, pp. 1962–1970.

Gilbert, H. J. and Fouch, M. (2007). "Complex upper mantle seismic structure across the southern Colorado Plateau/Basin and Range: II. Results from receiver function analysis". In: *Eos Trans. AGU* 88.52.

Given, J. W. and Mellman, G. R. (1986). *Estimating explosion and tectonic release source parameters of underground nuclear explosions from Rayleigh and Love wave observations*. Tech. rep. AFGL-TR-86- 0171(I). Air Force Geophysics Laboratory.

Goff, J. A. and Jordan, T. H. (1988). "Stochastic Modeling of Seafloor Morphology: Inversion of Sea Beam Data for Second-Order Statistics". In: *Journal of Geophysical Research: Solid Earth* 93.B11, pp. 13589–13608. DOI: 10.1029/JB093iB11p13589.

Goforth, T. T. and Bonner, J. L. (1995). "Characteristics of Rg waves recorded from quarry blasts in central Texas". In: *Bulletin of the Seismological Society of America* 85.4, pp. 1232–1235.

Graves, R. W., Aagaard, B. T., Hudnut, K. W., Star, L. M., Stewart, J. P., and Jordan, T. H. (2008). "Broadband simulations for Mw 7.8 southern San Andreas earthquakes: Ground motion sensitivity to rupture speed". In: *Geophysical Research Letters* 35.22. L22302, n/a–n/a. DOI: 10.1029/2008GL035750.

Graves, R. W. and Wald, D. J. (2001). "Resolution analysis of finite fault source inversion using one- and three-dimensional Green's functions: 1. Strong motions". In: *Journal of Geophysical Research: Solid Earth* 106.B5, pp. 8745–8766. DOI: 10.1029/2000JB900436.

Guilhem, A., Hutchings, L., Dreger, D. S., and Johnson, L. R. (2014). "Moment tensor inversions of M 3 earthquakes in the Geysers geothermal fields, California". In: *Journal of Geophysical Research: Solid Earth* 119.3. 2013JB010271, pp. 2121–2137.

Guilhem, A. and Dreger, D. S. (2011). "Rapid detection and characterization of large earthquakes using quasi-finite-source Green's functions in continuous moment tensor inversion". In: *Geophysical Research Letters* 38.13. L13318, n/a–n/a. DOI: 10.1029/2011GL047550.

Guilhem, A., Dreger, D. S., Tsuruoka, H., and Kawakatsu, H. (2013). "Moment tensors for rapid characterization of megathrust earthquakes: the example of the 2011 M 9 Tohoku-

oki, Japan earthquake". In: *Geophysical Journal International* 192.2, pp. 759–772. DOI: 10.1093/gji/ggs045.

Hardebeck, J. L. and Hauksson, E. (2001). "Stress Orientations Obtained from Earthquake Focal Mechanisms: What Are Appropriate Uncertainty Estimates?" In: *Bulletin of the Seismological Society of America* 91.2, pp. 250–262. DOI: 10.1785/0120000032.

Hardebeck, J. L. and Michael, A. J. (2006). "Damped regional-scale stress inversions: Methodology and examples for southern California and the Coalinga aftershock sequence". In: *Journal of Geophysical Research: Solid Earth* 111.B11. B11310, n/a–n/a. DOI: 10.1029/2005JB004144.

Helmberger, D. V. (1983). "Theory and application of synthetic seismograms". In: *Earthquakes: Observation, Theory, and Interpretation : Proceedings of the International School of Physics "Enrico Fermi", Course Lxxxv*. Ed. by Kanamori, H. and Boschi, E. Proceedings of the International School of Physics. Elsevier Science Ltd, pp. 174–222.

Herrmann, R. B. and Wang, C. Y. (1985). "A comparison of synthetic seismograms". In: *Bulletin of the Seismological Society of America* 75.1, pp. 41–56.

Herrmann, R. B. (2013). "Computer Programs in Seismology: An Evolving Tool for Instruction and Research". In: *Seismological Research Letters* 84.6, pp. 1081–1088. DOI: 10.1785/0220110096.

Hingee, M., Tkalčić, H., Fichtner, A., and Sambridge, M. (2011). "Seismic moment tensor inversion using a 3-D structural model: applications for the Australian region". In: *Geophysical Journal International* 184.2, pp. 949–964. DOI: 10.1111/j.1365-246X.2010.04897.x.

Holliger, K. and Levander, A. R. (1992). "A stochastic view of lower crustal fabric based on evidence from the Ivrea Zone". In: *Geophysical Research Letters* 19.11, pp. 1153–1156. DOI: 10.1029/92GL00919.

Hudson, J. A., Pearce, R. G., and Rogers, R. M. (1989). "Source type plot for inversion of the moment tensor". In: *Journal of Geophysical Research: Solid Earth* 94.B1, pp. 765–774.

Jost, M. L. and Herrmann, R. B. (1989). "A Student's Guide to and Review of Moment Tensors". In: *Seismological Research Letters* 60.2, pp. 37–57.

Julian, B. R., Miller, A. D., and Foulger, G. R. (1998). "Non-double-couple earthquakes 1. Theory". In: *Reviews of Geophysics* 36.4, pp. 525–549. DOI: 10.1029/98RG00716.

Kao, H., Jian, P.-R., Ma, K.-F., Huang, B.-S., and Liu, C.-C. (1998). "Moment-tensor inversion for offshore earthquakes east of Taiwan and their implications to regional collision". In: *Geophysical Research Letters* 25.19, pp. 3619–3622. DOI: 10.1029/98GL02803.

Kawakatsu, H. (1998). "On the Realtime Monitoring of the Long-period Seismic Wavefield". In: *Bulletin of the Earthquake Research Institute, University of Tokyo* 73, pp. 267–274.

Kennett, B. L. N. and Engdahl, E. R. (1991). "Traveltimes for global earthquake location and phase identification". In: *Geophysical Journal International* 105.2, pp. 429–465.

Keranen, K. M., Weingarten, M., Abers, G. A., Bekins, B. A., and Ge, S. (2014). "Sharp increase in central Oklahoma seismicity since 2008 induced by massive wastewater injection". In: *Science* 345.6195, pp. 448–451. DOI: 10.1126/science.1255802.

Khalturin, V. I., Rautian, T. G., and Richards, P. G. (1998). "The seismic signal strength of chemical explosions". In: *Bulletin of the Seismological Society of America* 88.6, pp. 1511–1524.

Kim, A., Dreger, D. S., and Larsen, S. (2010). "Moderate Earthquake Ground-Motion Validation in the San Francisco Bay Area". In: *Bulletin of the Seismological Society of America* 100.2, pp. 819–825. DOI: 10.1785/0120090076.

Kim, S., Rhie, J., and Kim, G. (2011). "Forward waveform modelling procedure for 1-D crustal velocity structure and its application to the southern Korean Peninsula". In: *Geophysical Journal International* 185.1, pp. 453–468.

Kustowski, B., Ekström, G., and Dziewonski, A. (2008). "The shear-wave moment tensor inversions for earthquakes in southern California". In: *Bulletin of the Seismological Society of America* 94.5, pp. 1748–1761.

Langston, C. A. (1981). "Source inversion of seismic waveforms: The Koyna, India, earthquakes of 13 September 1967". In: *Bulletin of the Seismological Society of America* 71.1, pp. 1–24.

Langston, C. A. and Helmberger, D. V. (1975). "A Procedure for Modelling Shallow Dislocation Sources". In: *Geophysical Journal of the Royal Astronomical Society* 42.1, pp. 117–130. DOI: 10.1111/j.1365-246X.1975.tb05854.x.

Larsen, S. and Shultz, C. (1995). *ELAS3D: 2D/3D elastic finite difference wave propagation code*. Technical Report UCRLMA-121792. Lawrence Livermore National Laboratory.

Laske, G. and Masters, G. (1997). "A Global Digital Map of Sediment Thickness". In: *EOS Trans. AGU* 78.F483.

Lee, E.-J., Chen, P., Jordan, T. H., and Wang, L. (2011). "Rapid full-wave centroid moment tensor (CMT) inversion in a three-dimensional earth structure model for earthquakes in Southern California". In: *Geophysical Journal International* 186.1, pp. 311–330. DOI: 10.1111/j.1365-246X.2011.05031.x.

Liu, Q., Polet, J., Komatitsch, D., and Tromp, J. (2004). "Spectral-Element Moment Tensor Inversions for Earthquakes in Southern California". In: *Bulletin of the Seismological Society of America* 94.5, pp. 1748–1761. DOI: 10.1785/012004038.

Massé, R. P. (1981). "Review of seismic source models for underground nuclear explosions". In: *Bulletin of the Seismological Society of America* 71.4, pp. 1249–1268.

McGarr, A. (2014). "Maximum magnitude earthquakes induced by fluid injection". In: *Journal of Geophysical Research: Solid Earth* 119.2, pp. 1008–1019. DOI: 10.1002/2013JB010597.

McLaughlin, K. L., Bonner, J. L., and Barker, T. (2004). "Seismic source mechanisms for quarry blasts: modelling observed Rayleigh and Love wave radiation patterns from a Texas quarry". In: *Geophysical Journal International* 156.1, pp. 79–93. DOI: 10.1111/j.1365-246X.2004.02105.x.

McNamara, D. E., Benz, H. M., Herrmann, R. B., Bergman, E. A., Earle, P., Holland, A., Baldwin, R., and Gassner, A. (2015). "Earthquake hypocenters and focal mechanisms in central Oklahoma reveal a complex system of reactivated subsurface strike-slip faulting".

In: *Geophysical Research Letters* 42.8. 2014GL062730, pp. 2742–2749. DOI: 10.1002/2014GL062730.

Menke, W. (1989). *Geophysical Data Analysis: Discrete Inverse Theory*. Revised Edition. International Geophysics. Academic Press.

Menke, W. (2012). *Chapter 5 - Solution of the Linear, Gaussian Inverse Problem, Viewpoint 3: Maximum Likelihood Methods*. Ed. by Menke, W. Third Edition. Boston: Academic Press, pp. 89–114.

Minson, S. E. and Dreger, D. S. (2008). "Stable inversions for complete moment tensors". In: *Geophysical Journal International* 174.2, pp. 585–592.

Minson, S. E., Dreger, D. S., Bürgmann, R., Kanamori, H., and Larson, K. M. (2007). "Seismically and geodetically determined nondouble-couple source mechanisms from the 2000 Miyakejima volcanic earthquake swarm". In: *Journal of Geophysical Research: Solid Earth* 112.B10. B10308.

Moschetti, M. P., Ritzwoller, M. H., Lin, F.-C., and Yang, Y. (2010). "Crustal shear wave velocity structure of the western United States inferred from ambient seismic noise and earthquake data". In: *Journal of Geophysical Research: Solid Earth* 115.B10. B10306, n/a–n/a. DOI: 10.1029/2010JB007448.

Mueller, R. A. and Murphy, J. R. (1971). "Seismic characteristics of underground nuclear detonations: Part I. Seismic spectrum scaling". In: *Bulletin of the Seismological Society of America* 61.6, pp. 1675–1692.

Murphy, J. R. (1977). "Seismic source functions and magnitude determinations for underground nuclear detonations". In: *Bulletin of the Seismological Society of America* 67.1, pp. 135–158.

Murphy, J. R. (1996). "Types of Seismic Events and Their Source Descriptions". English. In: *Monitoring a Comprehensive Test Ban Treaty*. Ed. by Husebye, E. S. and Dainty, A. M. Vol. 303. NATO ASI Series. Springer Netherlands, pp. 225–245. DOI: 10.1007/978-94-011-0419-7_16.

Nayak, A. and Dreger, D. (2015). "Source-type specific inversion of moment tensors". Bulletin of the Seismological Society of America Revised manuscript.

Nayak, A. and Dreger, D. S. (2014). "Moment Tensor Inversion of Seismic Events Associated with the Sinkhole at Napoleonville Salt Dome, Louisiana". In: *Bulletin of the Seismological Society of America* 104.4, pp. 1763–1776.

Nielsen, L. and Thybo, H. (2006). "Identification of crustal and upper mantle heterogeneity by modelling of controlled-source seismic data". In: *Tectonophysics* 416, pp. 209–228.

Olsen, K. B., Day, S. M., Dalguer, L. A., Mayhew, J., Cui, Y., Zhu, J., Cruz-Atienza, V. M., Roten, D., Maechling, P., Jordan, T. H., Okaya, D., and Chourasia, A. (2009). "ShakeOut-D: Ground motion estimates using an ensemble of large earthquakes on the southern San Andreas fault with spontaneous rupture propagation". In: *Geophysical Research Letters* 36.4. L04303, n/a–n/a. DOI: 10.1029/2008GL036832.

Olsen, K. B., Archuleta, R. J., and Matarese, J. R. (1995). "Three-Dimensional Simulation of a Magnitude 7.75 Earthquake on the San Andreas Fault". English. In: *Science*. New Series 270.5242, pages.

Panning, M., Dreger, D., and Tkalčić Hrvoječić, H. (2001). "Near-source velocity structure and isotropic moment tensors: A case study of the Long Valley Caldera". In: *Geophysical Research Letters* 28.9, pp. 1815–1818. DOI: 10.1029/2000GL012389.

Pasyanos, M. E., Dreger, D. S., and Romanowicz, B. (1996). "Toward real-time estimation of regional moment tensors". In: *Bulletin of the Seismological Society of America* 86.5, pp. 1255–1269.

Pasyanos, M. E., Franz, G. A., and Ramirez, A. L. (2006). "Reconciling a geophysical model to data using a Markov chain Monte Carlo algorithm: An application to the Yellow Sea–Korean Peninsula region". In: *Journal of Geophysical Research: Solid Earth* 111.B3. B03313, n/a–n/a. DOI: 10.1029/2005JB003851.

Patton, H. J. and Taylor, S. R. (2008). "Effects of shock-induced tensile failure on mb-Ms discrimination: Contrasts between historic nuclear explosions and the North Korean test of 9 October 2006". In: *Geophysical Research Letters* 35.14. L14301.

Patton, H. J. and Taylor, S. R. (2011). "The apparent explosion moment: Inferences of volumetric moment due to source medium damage by underground nuclear explosions". In: *Journal of Geophysical Research: Solid Earth* 116.B3. B03310.

Pearce, R. G. and Rogers, R. M. (1989). "Determination of earthquake moment tensors from teleseismic relative amplitude observations". In: *Journal of Geophysical Research: Solid Earth* 94.B1, pp. 775–786. DOI: 10.1029/JB094iB01p00775.

Petersen, M. D., Moschetti, M. P., Powers, P. M., Mueller, C. S., Haller, K. M., Frankel, A. D., Zeng, Y., Rezaeian, S., Harmsen, S. C., Boyd, O. S., Field, N., Chen, R., Rukstales, K. S., Luco, N., Wheeler, R. L., Williams, R. A., and Olsen, A. H. (2014). *Documentation for the 2014 Update of the United States National Seismic Hazard Map*. Open-File Report 2014–1091. U.S. Geological Survey. DOI: http://dx.doi.org/10.3133/ofr20141091.

Petersson, N. A. and Sjögreen, B. (2014). "Super-grid modeling of the elastic wave equation in semi-bounded domains". In: *Communications in Computational Physics* 16.4, pp. 913–955.

Pitarka, A. (1999). "3D Elastic finite-difference modeling of seismic motion using staggered grids with nonuniform spacing". In: *Bulletin of the Seismological Society of America* 89.1, pp. 54–68.

Porritt, R. W., Allen, R. M., and Pollitz, F. F. (2014). "Seismic imaging east of the Rocky Mountains with {USArray}". In: *Earth and Planetary Science Letters* 402. Special issue on {USArray} science, pp. 16–25. DOI: http://dx.doi.org/10.1016/j.epsl.2013.10.034.

Priestley, K. F., Walter, W. R., Martynov, V., and Rozhkov, M. V. (1990). "Regional seismic recordings of the Soviet nuclear explosion of the Joint Verification Experiment". In: *Geophysical Research Letters* 17.2, pp. 179–182.

Ramos-Martínez, J. and McMechan, G. A. (2001). "Source-Parameter Estimation by Full Waveform Inversion in 3D Heterogeneous, Viscoelastic, Anisotropic Media". In: *Bulletin of the Seismological Society of America* 91.2, pp. 276–291. DOI: 10.1785/0120000017.

Rautian, T. G. and Khalturin, V. I. (1978). "The use of the coda for determination of the earthquake source spectrum". In: *Bulletin of the Seismological Society of America* 68.4, pp. 923–948.

Rodgers, A., Petersson, N. A., Nilsson, S., Sjögreen, B., and McCandless, K. (2008). "Broadband Waveform Modeling of Moderate Earthquakes in the San Francisco Bay Area and Preliminary Assessment of the USGS 3D Seismic Velocity Model". In: *Bulletin of the Seismological Society of America* 98.2, pp. 969–988. DOI: 10.1785/0120060407.

Romanowicz, B., Dreger, D., Pasyanos, M., and Uhrhammer, R. (1993). "Monitoring of strain release in central and northern California using broadband data". In: *Geophysical Research Letters* 20.15, pp. 1643–1646. DOI: 10.1029/93GL01540.

Saikia, C. K., Kafka, A. L., Gnewuch, S. C., and McTigue, J. W. (1990). "Shear velocity and intrinsic Q structure of the shallow crust in southeastern New England from Rg wave dispersion". In: *Journal of Geophysical Research: Solid Earth* 95.B6, pp. 8527–8541. DOI: 10.1029/JB095iB06p08527.

Shen, W., Ritzwoller, M. H., and Schulte-Pelkum, V. (2013). "A 3-D model of the crust and uppermost mantle beneath the Central and Western US by joint inversion of receiver functions and surface wave dispersion". In: *Journal of Geophysical Research: Solid Earth* 118.1, pp. 262–276. DOI: 10.1029/2012JB009602.

Shuler, A., Ekström, G., and Nettles, M. (2013a). "Physical mechanisms for vertical-CLVD earthquakes at active volcanoes". In: *Journal of Geophysical Research: Solid Earth* 118.4, pp. 1569–1586. DOI: 10.1002/jgrb.50131.

Shuler, A., Nettles, M., and Ekström, G. (2013b). "Global observation of vertical-CLVD earthquakes at active volcanoes". In: *Journal of Geophysical Research: Solid Earth* 118.1, pp. 138–164. DOI: 10.1029/2012JB009721.

Šílený, J. (2004). "Regional moment tensor uncertainty due to mismodeling of the crust". In: *Tectonophysics* 383.3-4, pp. 133–147.

Sjögreen, B. and Petersson, N. (2012). "A Fourth Order Accurate Finite Difference Scheme for the Elastic Wave Equation in Second Order Formulation". English. In: *Journal of Scientific Computing* 52.1, pp. 17–48. DOI: 10.1007/s10915-011-9531-1.

Snoke, J. A. (2009). "Traveltime Tables for iasp91 and ak135". In: *Seismological Research Letters* 80.2, pp. 260–262.

Song, X. J., Helmberger, D. V., and Zhao, L. (1996). "Broad-Band Modelling of Regional Seismograms: the Basin and Range Crustal Structure". In: *Geophysical Journal International* 125.1, pp. 15–29. DOI: 10.1111/j.1365-246X.1996.tb06531.x.

Springer, D. L., Pawloski, G. A., Ricca, J. L., Rohrer, R. F., and Smith, D. K. (2002). "Seismic Source Summary for All U.S. Below-Surface Nuclear Explosions". In: *Bulletin of the Seismological Society of America* 92.5, pp. 1806–1840. DOI: 10.1785/0120010194.

Stevens, J. L. and Murphy, J. R. (2001). "Yield estimation from surface-wave amplitudes". In: *Pure and Applied Geophysics* 158.11, pp. 2227–2251. DOI: 10.1007/PL00001147.

Sun, X., Song, X., Zheng, S., Yang, Y., and Ritzwoller, M. H. (2010). "Three dimensional shear wave velocity structure of the crust and upper mantle beneath China from ambient noise surface wave tomography". English. In: *Earthquake Science* 23.5, pp. 449–463.

Tape, C., Liu, Q., Maggi, A., and Tromp, J. (2010). "Seismic tomography of the southern California crust based on spectral-element and adjoint methods". In: *Geophysical Journal International* 180.1, pp. 433–462. DOI: 10.1111/j.1365-246X.2009.04429.x.

Tape, W. and Tape, C. (2012a). "A geometric comparison of source-type plots for moment tensors". In: *Geophysical Journal International* 190.1, pp. 499–510.

Tape, W. and Tape, C. (2012b). "A geometric setting for moment tensors". In: *Geophysical Journal International* 190.1, pp. 476–498.

Templeton, D. C. and Dreger, D. S. (2006). "Non-Double-Couple Earthquakes in the Long Valley Volcanic Region". In: *Bulletin of the Seismological Society of America* 96.1, pp. 69–79.

Tkalčić, H., Dreger, D. S., Foulger, G. R., and Julian, B. R. (2009). "The Puzzle of the 1996 Bárdarbunga, Iceland, Earthquake: No Volumetric Component in the Source Mechanism". In: *Bulletin of the Seismological Society of America* 99.5, pp. 3077–3085.

Toksöz, M. N., Harkrider, D. G., and Ben-Menahem, A. (1965). "Determination of source parameters by amplitude equalization of seismic surface waves: 2. Release of tectonic strain by underground nuclear explosions and mechanisms of earthquakes". In: *Journal of Geophysical Research* 70.4, pp. 907–922.

Toksöz, M. N. and Kehrer, H. H. (1972). "Tectonic Strain Release by Underground Nuclear Explosions and its Effect on Seismic Discrimination". In: *Geophysical Journal of the Royal Astronomical Society* 31.1-3, pp. 141–161.

Vavryčuk, V. (2015). "Moment tensor decompositions revisited". In: *Journal of Seismology* 19.1, pp. 231–252. DOI: 10.1007/s10950-014-9463-y.

Waldhauser, F., Schaff, D., Richards, P. G., and Kim, W.-Y. (2004). "Lop Nor Revisited: Underground Nuclear Explosion Locations, 1976-1996, from Double-Difference Analysis of Regional and Teleseismic Data". In: *Bulletin of the Seismological Society of America* 94.5, pp. 1879–1889.

Walter, F., Clinton, J. F., Deichmann, N., Dreger, D. S., Minson, S. E., and Funk, M. (2009). "Moment Tensor Inversions of Icequakes on Gornergletscher, Switzerland". In: *Bulletin of the Seismological Society of America* 99.2A, pp. 852–870. DOI: 10.1785/0120080110.

Walter, F., Dreger, D. S., Clinton, J. F., Deichmann, N., and Funk, M. (2010). "Evidence for Near-Horizontal Tensile Faulting at the Base of Gornergletscher, a Swiss Alpine Glacier". In: *Bulletin of the Seismological Society of America* 100.2, pp. 458–472. DOI: 10.1785/0120090083.

Walter, W., Matzel, E., Pasyanos, M., Harris, D., Gok, R., and Ford, S. (2007). "Empirical Observations of Earthquake-Explosion Discrimination Using P/S Ratios and Implications for the Sources of Explosion S-Waves". In: *Proceedings of the 30th Monitoring Research Review: Ground-Based Nuclear Explosion Monitoring Technologies*. Vol. 1, pp. 684–694.

Walter, W. R. and Ammon, C. J. (1993). *Complete regional seismic waveform inversion for crust and upper mantle structure: the September 14, 1988 JVE explosion, Kazakhstan, Eurasia*. Tech. rep. UCRL-JC-112844. Lawrence Livermore National Laboratory.

Walter, W. R. and Patton, H. J. (1990). "Tectonic release from the Soviet Joint Verification Experiment". In: *Geophysical Research Letters* 17.10, pp. 1517–1520.

Walter, W. R. and Rodgers, A. J. (1999). "Regional waveform modeling in southwestern Asia: tectonic release from the May 11, 1998 Indian nuclear tests". 94th SSA Annual Meeting.

Wang, C. Y. and Herrmann, R. B. (1980). "A numerical study of P-, SV-, and SH-wave generation in a plane layered medium". In: *Bulletin of the Seismological Society of America* 70.4, pp. 1015–1036.

Wei, S., Zhan, Z., Tan, Y., Ni, S., and Helmberger, D. (2012). "Locating earthquakes with surface waves and centroid moment tensor estimation". In: *Journal of Geophysical Research: Solid Earth* 117.B4. B04309. DOI: 10.1029/2011JB008501.

Wu, R.-S. (1982). "Attenuation of short period seismic waves due to scattering". In: *Geophysical Research Letters* 9.1, pp. 9–12. DOI: 10.1029/GL009i001p00009.

Yang, X., North, R., Romney, C., and Richards, P. G. (2003). "Worldwide nuclear explosions". In: *International Handbook of Earthquake and Engineering Seismology*. Ed. by William H.K. Lee Hiroo Kanamori, P. C. J. and Kisslinger, C. Vol. 81, Part B. International Geophysics. Academic Press. Chap. 84, pp. 1595–1599.

Zhao, L., Chen, P., and Jordan, T. H. (2006). "Strain Green's Tensors, Reciprocity, and Their Applications to Seismic Source and Structure Studies". In: *Bulletin of the Seismological Society of America* 96.5, pp. 1753–1763. DOI: 10.1785/0120050253.

Zhu, L. and Rivera, L. A. (2002). "A note on the dynamic and static displacements from a point source in multilayered media". In: *Geophysical Journal International* 148.3, pp. 619–627.